Syracuse University

SURFACE

Dissertations - ALL   SURFACE

August 2020

Effects of Surface Topography on Bacterial Biofilm Formation

Sang Won Lee
Syracuse University

Abstract

Biofilms are multicellular structures with bacterial cells attached to a surface and embedded in an extracellular matrix. With high-level resistance to antimicrobial agents, biofilms are the cause of chronic infections associated with implanted medical devices such as breast implants, orthopedic devices, pace markers, and many others. Besides the prevalence, biofilm infections are associated with high mortality, presenting an urgent need for more effective controls. Several strategies such as coating with antimicrobial agents and changing chemical, physical, and biological properties of biomaterials have been attempted, but bacteria have remarkable capabilities to overcome unfavorable conditions over time and long-term biofilm control remains challenging. In addition, most approaches are based on empirical experiments rather than rational designs, limiting their effects, especially *in vivo*.

In this study, we engineered surface topography in two ways (static and dynamic) to better understand and control bacterial biofilm formation. For the static surface topography, a high-throughput approach to study bacterial attachment on PDMS surfaces with different textures was developed. By testing bacterial adhesion to samples with square-shaped recessive patterns with varying size and inter-pattern distance, surface features that promote biofilm formation were identified. *E. coli* attachment did not exhibit a monotonic, linear relationship with surface area, but depended on the 3D topography.

For dynamic surface topography, we used shape memory polymers (SMPs) to obtain on-demand dynamic changes in substratum topography. Our results show that shape recovery of *tert*-butyl acrylate (tBA) based one-way SMP caused 99.9% detachment of 48 h *Pseudomonas aeruginosa* PAO1 biofilms. Interestingly, *P. aeruginosa* PAO1 biofilm cells detached by shape recovery showed 2,479 times higher antibiotic susceptibility compared to the original biofilm

cells. The released biofilm cells also presented 4.1 times higher expression of the gene *rrnB*, encoding ribosomal RNA, and 11.8 times more production of adenosine triphosphate (ATP) than the control biofilm cells.

To further develop this technology for long-term biofilm control, we synthesized reversible SMP with different molecular weights of poly(ε-caprolactone) diisocyanatoethyl dimethacrylate (PCLDIMA), with 25 wt.% of butyl acrylate (BA) as a linker, and 1 wt.% of benzoyl peroxide (BPO) as a thermal initiator. Among various combinations of molecular weight, 2:1 wt. ratio mixture of 15,000 g/mol PCLDIMA and 2,000 g/mol PCLDIMA showed a transition temperature of 36.7°C. The created rSMP has repeatable and reversible shape recovery for more than 3 cycles. With 18% stretch, 61.0±6.6% of 48 h *P. aeruginosa* PAO1 biofilm cells were removed in each shape recovery cycle on average, with a total of 94.3±1.0% biofilm removal after three consecutive shape recovery cycles.

In summary, the results of this study demonstrated that surface topography has potent effects on bacterial adhesion and biofilm formation. We believe that these results not only provide important information for understanding the risk of medical devices but also helps the design of control methods for preventing chronic infections associated with implanted medical devices.

**EFFECTS OF SURFACE TOPOGRAPHY
ON BACTERIAL BIOFILM FORMATION**

by

Sang Won Lee

B.S. Chemical Engineering, Sungkyunkwan University, 2012
M.S. Chemical and Biological Engineering, Seoul National University, 2014

Dissertation
Submitted in partial fulfillment of the requirements for the degree of
Doctor of Philosophy in Chemical Engineering

Syracuse University
August 2020

Acknowledgements

I would like to express my deep and sincere gratitude to my research supervisor, Prof. Dacheng Ren, Ph.D., for giving me the opportunity to do research and providing invaluable guidance throughout this research. His dynamism, vision, sincerity and motivation have deeply inspired me. He has taught me the methodology to carry out the research and to present the research works as clearly as possible. It was a great privilege and honor to work and study under his guidance. I am extremely grateful for what he has offered me. I would also like to thank him for his friendship, empathy, and great sense of humor.

I am extremely grateful to my family especially my parents and sister for their love, prayers, caring and sacrifices for educating and preparing me for my future. I am very much thankful to my girlfriend, Sara, for her love, understanding, prayers and continuing support to complete this research work. My special thanks go to all my friends in Korea (especially Patrick Kim) for the keen interest shown to complete this thesis successfully. I would like to say thanks to my friends and research colleagues, Dr. Gu, Sweta, Yousr, Jerry, Eloise, Hao Wang, Hao Li, Tian, Joe, Fangchao, Ali, Nick, Yanrui, Bo, Seungrak, Sejung, Jim, Heejae, Bryant, and Dr. Danny Park for their constant encouragement. I express my special thanks to Dr. K. Scott Phillips, Dr. Hainsworth Shin, and Dr. Eva Wang at FDA for their genuine supports throughout this research work. I am extending my thanks to the committee members, Dr. Henderson, Dr. Soman, Dr. Ma, and Dr. Movileanu, for being a committee member or a chair of my defense. I also thank all the staff of Syracuse University, FDA, and CNF at Cornell University for their kindness.

Finally, my thanks go to all the people who have supported me to complete the research work directly or indirectly.

Table of Contents

List of Tables

List of Figures

Chapter 1

Motivation, hypothesis, and objectives

1.1 Motivations

Based on National Health Survey data and a report of 'implantable medical devices market', more than 6 million of procedures for implantable medical devices are conducted every year in the U.S. and its global market is worth $96.6 billion in 2018 and projected to reach $143.3 billion by 2024 [1,2]. As the uses of implantable medical devices increase, device-associated infections are on the rise and have remained difficult to treat. According to the National Institute of Health (NIH), biofilms are involved in up to 80% of the total medical-associated microbial chronic infections [3].

Bacteria can colonize both biotic and abiotic surfaces and form biofilms that are multicellular structures with extracellular polymeric substrates secreted by the attached cells [4]. Cells in mature biofilms are also associated with slow growth and difficult to eradicate compared to their planktonic counterparts due to enhanced resistance to antimicrobials and other disinfection agents [5,6]. As a result, biofilms are up to 1,000 times more tolerant of antibiotics compared to planktonic cells which result in chronic infections associated with implanted medical devices [7,8]. Thus, the grand challenge of biofilms has motivated the search for new strategies for biofilm prevention and removal.

The economical and clinical significance of biofilm-related problems has stimulated intensive research to design more effective anti-fouling strategies [9–12]. To prevent bacteria from colonizing a surface, different approaches have been explored to alter the properties of the substrate materials such as surface chemistry [13,14], topography [15–18], and stiffness [19,20]. Among these chemical and mechanical properties, topography has attracted increasing attention.

A large number of studies on topographic effects have been conducted to investigate how micron- and nano-scale topographies affect cell adhesion and biofilm formation. Some nano-scale topographies have been demonstrated to have bactericidal effects through direct damage to bacterial membranes [17]. In contrast, micron-scale topographies do not have bactericidal effects but may inhibit bacterial adhesion through specific effects on bacteria-material interactions [10]. Topographic features associated with a bacterial infection on medical devices were also studied and it can be organized based on their locations of use such as breast implants [21], bone implants [22–24], catheters [25], and oral implants [26–28]. Among these, orthopedics devices and dental implants have been explored more than the other devices. It will be helpful to investigate the effects of surface topography of soft materials such as breast implants and catheters.

It is worth noticing that most studies on topography are based on protruding features. There is a lack of understanding of how recessive features affect biofilm formation, which is commonly present on implant surfaces such as breast implants. Investigation of bacterial adhesion on recessive patterns will provide not only new information about the mechanism of bacterial attachment but also guidance for new device designs.

To remove mature biofilms from the surface, we developed a novel strategy of dynamic topography using shape memory polymer. Based on the similar polymeric materials used for urinary catheter devices, we used *tert*-butyl acrylate-based polymers and polycaprolactone based polymers and studied the effects of dynamic change in topography on biofilm removal and the physiology of biofilm cells.

1.2 Hypothesis and objectives

In this study, we hypothesize that the changes in micron-scale topography can significantly affect biofilm structure and the physiology of biofilm cells. To test this hypothesis, we investigated bacterial attachment and biofilm removal by systematically varying surface topography (Figure 1.1).
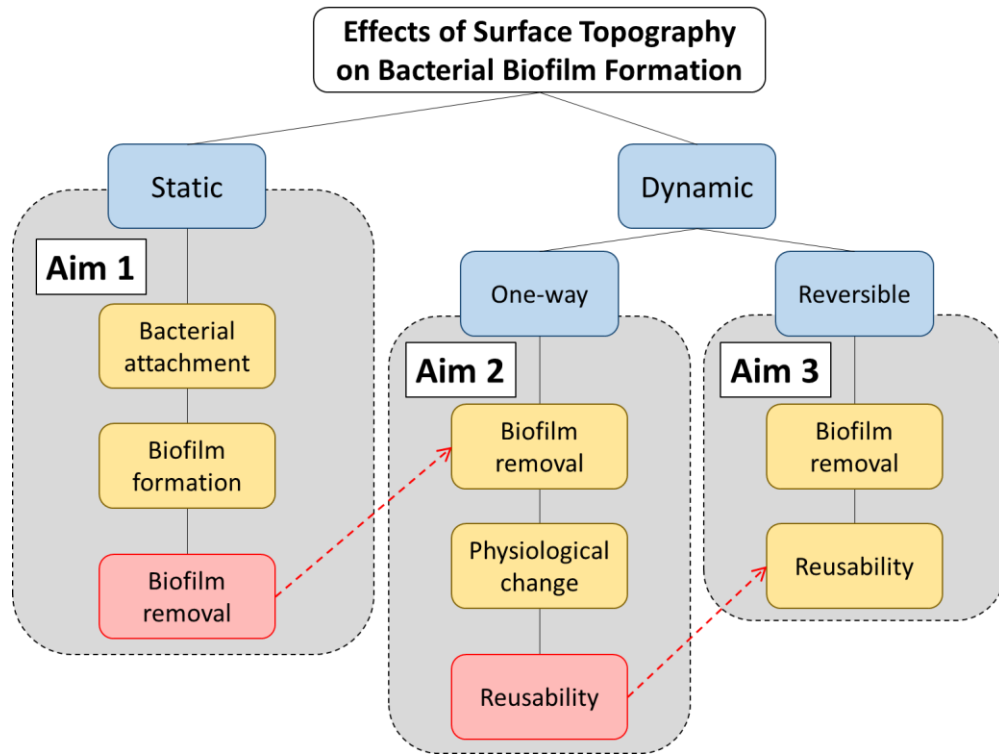
Figure 1.1 A schematic diagram of the aims process.

The work of the study is outlined in the following specific objectives.

Objectives 1: Investigate the effects of static surface topography of polydimethylsiloxane (PDMS) on *E. coli* RP437/pRSH103 attachment and its biofilm formation.

Objectives 2: Examine the effects of dynamic surface topography using one-way shape memory polymers (SMPs).

Objectives 3: Demonstrate the effects of dynamic surface topography evaluated by reversible

shape memory polymers (rSMPs).

1.3 References

[1]   IMARC Group, Implantable Medical Devices Market: Global Industry Trends, Share, Size, Growth, Opportunity and Forecast 2019-2024, 2019.

[2]   Centers for Disease Control and Prevention, Number of all-listed procedures for discharges from short-stay hospitals, 2010.

[3]   Z. Khatoon, C.D. McTiernan, E.J. Suuronen, T.-F. Mah, E.I. Alarcon, Bacterial biofilm formation on implantable devices and approaches to its treatment and prevention, Heliyon. 4 (2018) e01067. https://doi.org/10.1016/j.heliyon.2018.e01067.

[4]   H.C. Flemming, J. Wingender, The biofilm matrix, Nat. Rev. Microbiol. 8 (2010) 623–633. https://doi.org/10.1038/nrmicro2415.

[5]   I. Olsen, Biofilm-specific antibiotic tolerance and resistance, Eur. J. Clin. Microbiol. Infect. Dis. 34 (2015) 877–886. https://doi.org/10.1007/s10096-015-2323-z.

[6]   C.W. Hall, T.F. Mah, Molecular mechanisms of biofilm-based antibiotic resistance and tolerance in pathogenic bacteria, FEMS Microbiol. Rev. 41 (2017) 276–301. https://doi.org/10.1093/femsre/fux010.

[7]   L. Hall-Stoodley, J.W. Costerton, P. Stoodley, Bacterial biofilms: From the natural environment to infectious diseases, Nat. Rev. Microbiol. 2 (2004) 95–108. https://doi.org/10.1038/nrmicro821.

[8]   R.D. Wolcott, G.D. Ehrlich, Biofilms and chronic infections, JAMA - J. Am. Med. Assoc. 299 (2008) 2682–2684. https://doi.org/10.1001/jama.299.22.2682.

[9]   H. Koo, R.N. Allan, R.P. Howlin, P. Stoodley, L. Hall-Stoodley, Targeting microbial

biofilms: Current and prospective therapeutic strategies, Nat. Rev. Microbiol. 15 (2017) 740–755. https://doi.org/10.1038/nrmicro.2017.99.

[10] H. Gu, D. Ren, Materials and surface engineering to control bacterial adhesion and biofilm formation: A review of recent advances, Front. Chem. Sci. Eng. 8 (2014) 20–33. https://doi.org/10.1007/s11705-014-1412-3.

[11] F. Song, H. Koo, D. Ren, Effects of material properties on bacterial adhesion and biofilm formation, J. Dent. Res. 94 (2015) 1027–1034. https://doi.org/10.1177/0022034515587690.

[12] K. Liu, L. Jiang, Bio-inspired design of multiscale structures for function integration, Nano Today. 6 (2011) 155–175. https://doi.org/10.1016/j.nantod.2011.02.002.

[13] L. Zhao, P.K. Chu, Y. Zhang, Z. Wu, Antibacterial coatings on titanium implants, J. Biomed. Mater. Res. - Part B Appl. Biomater. 91 (2009) 470–480. https://doi.org/10.1002/jbm.b.31463.

[14] E.B.H. Hume, J. Baveja, B. Muir, T.L. Schubert, N. Kumar, S. Kjelleberg, H.J. Griesser, H. Thissen, R. Read, L.A. Poole-Warren, K. Schindhelm, M.D.P. Willcox, The control of Staphylococcus epidermidis biofilm formation and in vivo infection rates by covalently bound furanones, Biomaterials. 25 (2004) 5023–5030. https://doi.org/10.1016/j.biomaterials.2004.01.048.

[15] K. Anselme, P. Davidson, A.M. Popa, M. Giazzon, M. Liley, L. Ploux, The interaction of cells and bacteria with surfaces structured at the nanometre scale, Acta Biomater. 6 (2010) 3824–3846. https://doi.org/10.1016/j.actbio.2010.04.001.

[16] H. Gu, K.W. Kolewe, D. Ren, Conjugation in Escherichia coli Biofilms on

       Poly(dimethylsiloxane) Surfaces with Microtopographic Patterns, Langmuir. 33 (2017)

       3142–3150. https://doi.org/10.1021/acs.langmuir.6b04679.

[17] M.N. Dickson, E.I. Liang, L.A. Rodriguez, N. Vollereaux, A.F. Yee, Nanopatterned

       polymer surfaces with bactericidal properties, Biointerphases. 10 (2015) 021010.

       https://doi.org/10.1116/1.4922157.

[18] D. Perera-Costa, J.M. Bruque, M.L. González-Martín, A.C. Gómez-García, V. Vadillo-

       Rodríguez, Studying the influence of surface topography on bacterial adhesion using

       spatially organized microtopographic surface patterns, Langmuir. 30 (2014) 4633–4641.

       https://doi.org/10.1021/la5001057.

[19] F. Song, H. Wang, K. Sauer, D. Ren, Cyclic-di-GMP and oprF are involved in the

       response of Pseudomonas aeruginosa to substrate material stiffness during attachment on

       polydimethylsiloxane (PDMS), Front. Microbiol. 9 (2018) 1–13.

       https://doi.org/10.3389/fmicb.2018.00110.

[20] Y. Zhao, F. Song, H. Wang, J. Zhou, D. Ren, Phagocytosis of Escherichia coli biofilm

       cells with different aspect ratios: a role of substratum material stiffness, Appl. Microbiol.

       Biotechnol. 101 (2017) 6473–6481. https://doi.org/10.1007/s00253-017-8394-2.

[21] B.H. Shin, B.H. Kim, S. Kim, K. Lee, Y. Bin Choy, C.Y. Heo, Silicone breast implant

       modification review: Overcoming capsular contracture, Biomater. Res. 22 (2018) 37.

       https://doi.org/10.1186/s40824-018-0147-5.

[22] K. Kapat, P.P. Maity, A.P. Rameshbabu, P.K. Srivas, P. Majumdar, S. Dhara,

       Simultaneous hydrothermal bioactivation with nano-topographic modulation of porous

titanium alloys towards enhanced osteogenic and antimicrobial responses, J. Mater. Chem. B. 6 (2018) 2877–2893. https://doi.org/10.1039/c8tb00382c.

[23] W.J. Metsemakers, T. Schmid, S. Zeiter, M. Ernst, I. Keller, N. Cosmelli, D. Arens, T.F. Moriarty, R.G. Richards, Titanium and steel fracture fixation plates with different surface topographies: Influence on infection rate in a rabbit fracture model, Injury. 47 (2016) 633–639. https://doi.org/10.1016/j.injury.2016.01.011.

[24] P.M. Tsimbouri, L. Fisher, N. Holloway, T. Sjostrom, A.H. Nobbs, R.M.D. Meek, B. Su, M.J. Dalby, Osteogenic and bactericidal surfaces from hydrothermal titania nanowires on titanium substrates, Sci. Rep. 6 (2016) 36857. https://doi.org/10.1038/srep36857.

[25] O. Mrad, J. Saunier, C. Aymes-Chodur, V. Rosilio, S. Bouttier, F. Agnely, P. Aubert, J. Vigneron, A. Etcheberry, N. Yagoubi, A multiscale approach to assess the complex surface of polyurethane catheters and the effects of a new plasma decontamination treatment on the surface properties, Microsc. Microanal. 16 (2010) 764–778. https://doi.org/10.1017/S1431927610093876.

[26] J. Verran, C.J. Maryan, Retention of Candida albicans on acrylic resin and silicone of different surface topography, J. Prosthet. Dent. 77 (1997) 535–539. https://doi.org/10.1016/S0022-3913(97)70148-3.

[27] A. Ionescu, E. Wutscher, E. Brambilla, S. Schneider-Feyrer, F.J. Giessibl, S. Hahnel, Influence of surface properties of resin-based composites on in vitro Streptococcus mutans biofilm development, Eur. J. Oral Sci. 120 (2012) 458–465. https://doi.org/10.1111/j.1600-0722.2012.00983.x.

[28] P.P.C. Pita, J.A. Rodrigues, C. Ota-Tsuzuki, T.F. Miato, E.G. Zenobio, G. Giro, L.C.

Figueiredo, C. Gonçalves, S.A. Gehrke, A. Cassoni, J.A. Shibli, Oral streptococci biofilm formation on different implant surface topographies, Biomed Res. Int. 2015 (2015) 1–6. https://doi.org/10.1155/2015/159625.

Chapter 2

Literature review:

Topographic effects on bacterial adhesion and biofilm formation

2.1 Bacterial biofilms

Bacteria can survive in challenging environments by attaching to a surface and developing a biofilm that consists of sessile bacterial cells and an extracellular matrix [1,2]. Cells in mature biofilms are also associated with slow growth, which renders most antibiotics ineffective [3,4]. Consequently, biofilms are up to 1,000 times more tolerant to antibiotics compared to planktonic cells which result in chronic infections associated with implanted medical devices [2,5]. As shown in Figure 2.1, a lifecycle of biofilm formation can be categorized into four steps; attachment, growth, maturation, and detachment [2,6]. (1) Bacteria with a challenging environment are easily looking for surfaces to attach and transform their state from 'swimmers' to 'stickers' by changing their gene expression. (2) After the irreversible attachment, the adhered bacteria start to grow with multiplying themselves and producing an extracellular matrix (ECM) composed of proteins, DNA, polysaccharides, and RNA. (3) When the bacteria colonize, called biofilm, it grows until reaches a balance between biofilm formation and the environmental condition around itself (maturation). (4) However, the matured biofilms start looking for other new surfaces with detaching themselves from the surface when there is a lack of nutrients or the environmental condition has changed. The cycle of the biofilm formation process keeps rotating repeatedly until their death. These biofilms can exist anywhere in natural communities, public health, industrial environments, etc.
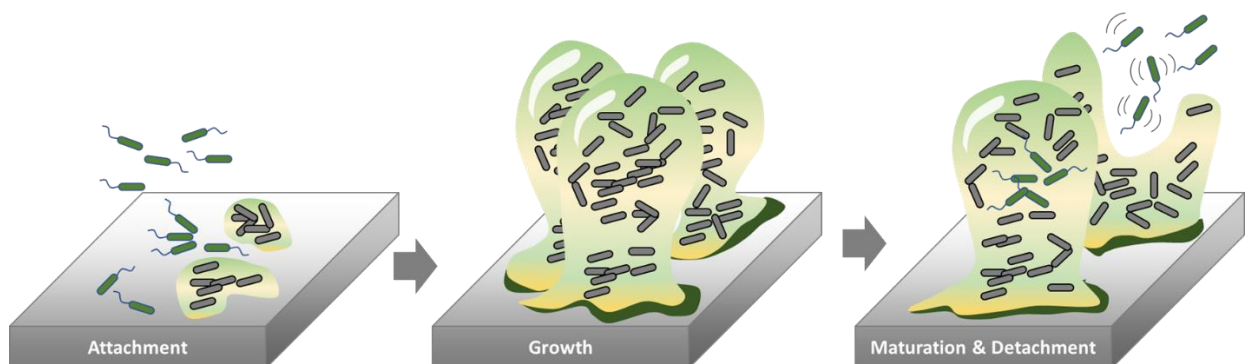
Figure 2.1. A schematic diagram of biofilm life cycle; (1) attachment, (2) growth, (3) maturation, and (4) detachment.

2.2 Healthcare-associated chronic infections

Microbes have remarkable capabilities to form biofilms on biomaterials which can affect the safe use and function of medical devices in humans [7–10]. Based on National Health Survey data and a report of 'implantable medical devices market', more than 6 million of procedures for implantable medical devices are conducted every year in the U.S. and its global market is worth $96.6 billion in 2018 and projected to reach $143.3 billion by 2024 [11,12]. As the uses of implantable medical devices increase, device-associated infections are on the rise and have remained difficult to treat. In addition, the biofilms are involved in more than 65% of nosocomial infections [2,5,13] and up to 80% of the total medical-associated microbial chronic infection rates [7] according to the Centers for Disease Control and Prevention (CDC) and National Institute of Health (NIH), respectively. The association between medical device-related infections and biofilms of multidrug-resistant organisms has recently been established by large-scale clinical data [8]. Thus, the economical and clinical significance of biofilm-related problems has stimulated intensive research to design more effective anti-fouling strategies.

2.3 Current strategies for controlling medical device-associated infections

To prevent bacteria from colonizing a surface, different approaches have been explored to alter the properties of the substrate materials such as surface chemistry [14–27], topography [28–39], and stiffness [40–43]. Strategies for modifying surface chemistry include coating with antibacterial agents [15,16,18–22,25] or other compounds that can change the charge [26] or hydrophobicity [14,17,24,27]. Surface hydrophobicity can also be changed by altering surface

topography [39]. Inspired by natural anti-fouling surfaces such as sharkskin [44], lotus leaves [14], taro leaves [17], and cicada wings [36], static micron- and nano-scale patterns and roughness have been created and demonstrated to prevent biofilm formation without using antimicrobial agents that can potentially promote resistance. Chemical and physical properties of the substrate material have a significant and broad-spectrum impact on biofilm formation and thus are promising targets for engineering antifouling materials. These chemical and physical approaches have been demonstrated to inhibit bacterial adhesion; however, challenges such as sustaining the efficacy of control agents, adverse effects of environmental and host factors (e.g., covering by body fluid or metabolic products during bacterial growth), and the remarkable capabilities of bacteria to adapt to challenging environments can allow bacteria to overcome unfavorable surface properties and eventually form biofilms over time [45]. Thus, a further study of developing better strategies to eradicate biofilms is in progress.

2.4 Interaction of bacteria with surface topography during initial attachment

Bacteria cannot see or hear, and thus rely on touch when it comes to "reading" the surface topographies. This can be done by using flagella [46,47], pili [46,48,49], and mechano-sensitive channels of membranes [50,51]. The response of bacteria to the surface topographies, however, varies depending on the types of surface topography and bacterial species. *E. coli* moves it flagella clockwise when settling down on a flat surface [52], but has more tumbling as the groove size of surface topography gets smaller [46,53]. *E. coli* was found to elongate to attach to the surface features of grooves/channels when its size becomes smaller than the cell body (~1.3 µm) [54]. *B. subtilis* enters a stable state from a turbulent state when the channel width reaches 70 µm [55] and *P. aeruginosa* prefers to swim in the grooves between protrusive hemispheres with a diameter of 8 µm [56]. Gu *et al.* [57] proposed a set of criteria for the rational design of

micron-scale anti-fouling surface topographies based on the study of how *E. coli* with protrusive

surface topographies and the best designed showed 84% reduction of *E. coli* biofilm formation.

For sub-micron topographies, the size of features is the most important parameter on bacterial

initial attachment [58].

When the size of topographic features gets to sub-micron bacterial membranes can be ruptured

by nano-scale features due to the increase of contact pressure and a shear force [59]. For

instance, Dickson *et al.* [36] proposed that smaller nanofeature sizes and closer distances

between nano features will lead to a higher bactericidal effect. Wu *et al.* [60] and Fisher *et al.*

[61] also suggested that inhomogeneous height and different feature types (nanocones,

nanoneedles) will increase the stretch of bacterial membranes, which results in bacterial death or

less bacterial attachment on the surfaces.

2.5 Surface topography effects on bacterial adhesion and biofilm formation

In recent years the importance of surface topography in microbial adhesion has come to the

fore [26,35,41,62–66] not only as a promising area of research but also for its importance in the

real-world medical challenges. One example with significant implications for women's health is

the link between surface topography and incidence of breast implant-associated anaplastic large

cell lymphoma (BIA-ALCL), which occur predominately with textured implants rather than

smooth implants [67]. Although it is not yet understood why textured implants are associated

with BIA-ALCL [68], several research publications suggest that bacterial factors, possibly from

biofilms, may contribute [7,68–73]. The interplay between bacteria, host factors, and the breast

implant, and how this affects the long-term safety of an implant is still largely unknown, as is the

case with many other medical devices. There are significant public debate and both regulatory

agencies [74], and standards organizations [75–77] worldwide are considering if surface topography should be considered in risk classification.

Given the significant role of bacterial biofilms in medical device-associated infections, there has been significant research on how bacteria interact with surface topographies and how to rationally design surface topography as a strategy to create antifouling and contact killing materials. We believe that the field will benefit from a better connection that integrates research on how bacteria sense and respond to surface topographies with research that measures how well surfaces work to prevent biofilm formation. Translating the basic scientific understanding of how bacteria read the map to the real-world application for medical devices requires not only an understanding of what types of surface topology are antifouling and what types should be avoided but also the knowledge of how the complex *in vivo* milieu (or medically specific environmental conditions) affects the performance of the devices in humans (Figure 2.2).
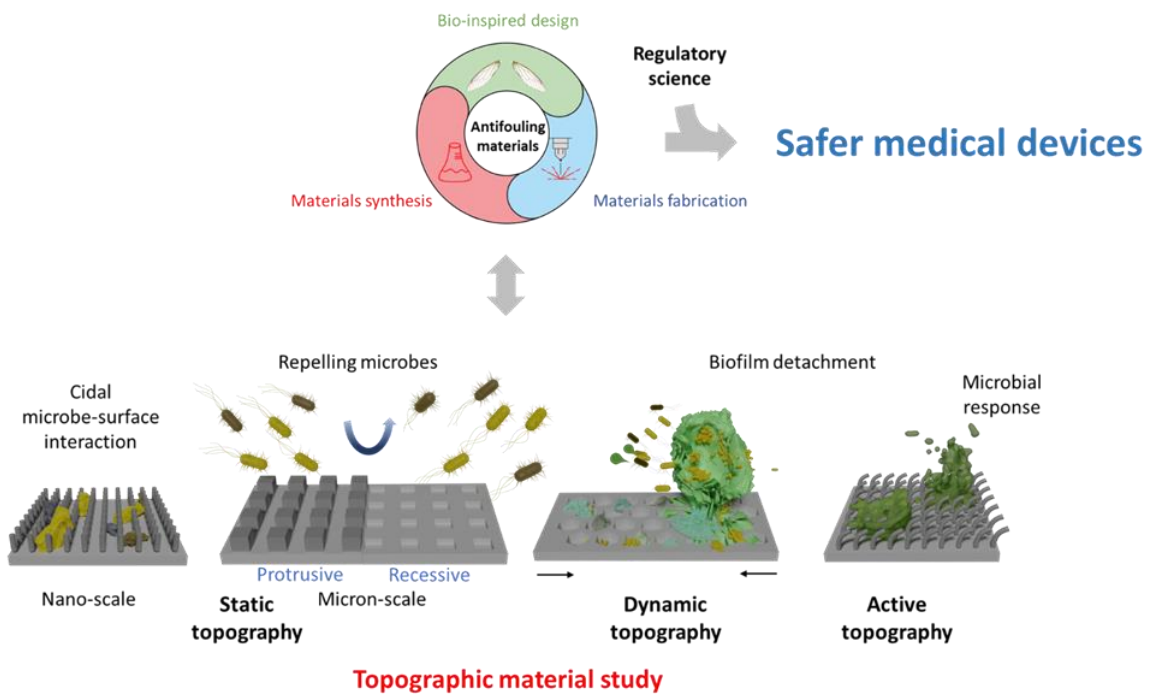
Figure 2.2. Schematic showing how materials synthesis, materials fabrication, and bio-inspired design feed into the medical device development process including regulatory science, to create safer and more effective medical devices. Classes of topography-based antifouling materials include nano-scale microbicidal designs (left), micron-scale static designs (second left), dynamic designs (second right), and active designs (right).

A large number of studies have been conducted to investigate how micron- and nano-scale topographies affect cell adhesion and biofilm formation, and to explore the possibility of promoting host tissue growth while inhibiting bacterial adhesion. The vast majority of studies to date have been focused on static topographies, including both protrusive and recessive features, with either well-defined or relatively random size and distribution. The features reported to date have been tested on both polymeric and metallic materials, from nm to µm scale, and include both designed topographies and bioinspired features mimicking those on plant leaves [78], shark skin [44], and insect wings [36]. While certain features were found to promote bacterial attachment and biofilm formation, most studies were aimed to identify antifouling materials. In general, micron-scale topographies do not have bactericidal effects but may inhibit bacterial adhesion through specific effects on bacteria-material interactions. In contrast, several nano-scale topographies have bactericidal effects by directly damaging bacterial membranes.

2.5.1 Micron-scale static surface topography

Micron-scale topographies have been shown to affect the attachment and biofilm formation of different bacterial strains on varying materials such as poly(methyl methacrylate) (PMMA) [79], polystyrene [80], polyethylene glycol (PEG) hydrogel [81], polyethylene terephthalate (PET) [82], Si [83,84], optical fiber [85], and Ti [86]. Some of the designs were inspired by naturally

17

existing antifouling surfaces. For example, micron-scale topographies were created by mimicking the micropatterns on shark skin [44] for antifouling activities.

A number of studies reported evidence that bacteria can actively explore and respond to micron-scale surface topography during attachment. The size, shape, and distribution of topographic patterns all play an important role in bacterial attachment. Grooves between protruding features, especially the shallow ones, are prone to bacterial adhesion. Hsu *et al.* [87] argued that bacterial cells attempt to maximize their contact area with the surface during attachment. As a result, the cells aligned differently depending on the arrangement of topographic features. This is consistent with the report of Gu *et al.* [33] who studied how protrusive line topography affects the orientation of attached *E. coli* cells. The effects are attributed to how bacteria attach using flagella; e.g., when the flagella attach on the side of protrusive lines, the cells orient perpendicularly to the line direction. Hochbaum *et al.* [28] mentioned that as the distance of features varied from 4 µm to sub-micron size, the orientation of the attached single-cell changed from parallel to perpendicular to the post lattice protruding from the surface to place itself in the confined well area. Hou *et al.* [88] fabricated square-shaped protruding topographies (2-100 µm side length) on PDMS and observed up to 90% reduction of *E. coli* adherence on top of squares that are 20 µm × 20 µm or smaller. Cell attachment is significantly more when the surface area increases above this threshold dimension. Gu *et al.* [29,33] observed similar trends and found a decrease in conjugation with interruption of biofilm formation by surface topography. Many other topographic features can also inhibit bacterial biofilm formation such as line patterns [89,90], irregular micro pits [86], honeycombs [84], cylindrical wells [81,85], ridges [39,78,91,92], and pillars with shapes of square [80,83,93] or hexagon [46,79]. Although these studies differ in the pattern dimension and layout, substrate

material, and the bacterial strains tested, it is a common observation that bacterial adhesion decreases as the size of the topographic pattern get smaller [39,90–93]. An exception was the work of Zhang *et al.* [78] on biomimetic surfaces of spinach leaves. The authors observed no difference in the number of adherent bacteria between un-patterned and patterned (~50 µm wrinkle with 6.88 µm Rrms) surfaces.

Some of the patterns achieve antifouling effects through changes in hydrophobicity. By creating topographic features, it is possible to trap air bubbles and render the surface hydrophobic and antifouling [93]. In addition to such physical barriers, it is also possible to design antifouling surfaces by interfering with bacterial sensing. For example, Gu *et al.* [33] reported that *E. coli* attachment on the side of protruding patterns is not preferred by the cells. Inspired by this and other findings, a set of criteria was proposed for the rational design of micron-scale antifouling topographies including (1) small cross-sectional area (less than the 20 µm × 20 µm threshold), (2) 10 µm or more of height to prevent flagella from reaching the bottom, (3) more side area, and (4) 2-5 µm of inter-pattern distance to minimize the bacteria cells that settle or bridge over between features. The authors validated this principle with 10 µm tall hexagonal patterns with 15 µm side length and 2 µm inter-pattern distance and it reduced *E. coli* biofilm formation by 84% compared to the flat control [33].

Besides attachment, static topographies can also affect the physiology of bacterial cells. For example, micron-scale topography can affect bacterial motility. Chang *et al.* [46] reported that *P. aeruginosa* motility on surfaces with hemispheres is affected if the diameter of the sphere is 2 µm or longer, but not 1 µm. In a later study, the same group reported that the motility of *P. aeruginosa* over topographical steps is affected by the height of the step riser. The probability of crossing a step was found reduced if the height is comparable to the size of the cell [56]. In a

flow cell system, the velocity of *E. coli* cells moving over µm-size microwells is different from the velocity over a flat surface [93]. *E. coli* cell cluster formation on narrow (5 µm wide) line patterns is 14 times less than that on flat surfaces [33]. Micron-scale topography also affects bacterial conjugation [29]. An important consideration, and potential drawback to static topographic features, is that effective biofilm control depends on the direct interaction between bacteria and the surface. Multiple studies have shown that bacteria can attach to surfaces by overcoming unfavorable topographies [33,47,87,94,95]. Future studies are needed to better understand this behavior and mitigate them through rational design.

2.5.2 Nano-scale static surface topography

Unlike the micron-scale topographies that mainly affect bacterial attachment, some nanoscale topographies have bactericidal activities through piercing of the cell membrane. A number of studies have been inspired by nanofeatures on insect wings, which have bactericidal effects. For example, hexagonally arranged nanopillars on Clanger cicada (*Psaltoda claripennis*) wings can kill bacterial cells on contact [96]. Further study using atomic force microscopy (AFM) revealed that these nanopillars penetrate bacterial membranes and kill the cells within 3 minutes. The effects were found to be physical because coating the surface with gold did not change the effects [97]. These nanotopographies were found to kill Gram-negative bacteria such as *P. aeruginosa*, *E. coli*, and *P. fluorescen*t, but not Gram-positive bacteria, which have thicker cell walls and thus are more rigid [98]. This is consistent with some other reports [99] and the finding that cell rigidity plays a role in membrane damage by nanopillars [96]. A biophysical model revealed that the damage to the cell membrane is due to the stretches in the regions suspended between the pillars in contact with the bacterial cell [96]. There are also nanotopographies that have been shown to kill both Gram-negative and Gram-positive cells [100]. Linklater *et al.* [101]

and Ivanova *et al.* [102] reported strong bactericidal effects of nanofeatures on vertically aligned carbon nanotube and black silicon against Gram-negative and Gram-positive bacteria, with up to 99.3% reduction at a rate of 450,000 cells/min/cm^2. Au nanostructures including pillars, rings, and nuggets all showed >99% reduction of methicillin-resistant *S. aureus* [103].

Kelleher *et al.* [104] found that the nanostructures on the wings of three different Cicada species were all hydrophobic with low surface energy. Nanostructures with the strongest bactericidal effects had the shortest spacing between nanopillars and the highest level of roughness. In addition to cicada wings, the skin of the box-patterned gecko (*Lucasium sp.*) with its spinules (hairs) [105] and nanotextures on dragonfly wings (*Orthetrum villosovittatum*) [59] is also antibacterial and self-cleaning. The surfaces were found to kill Gram-negative bacteria but not human stem cells [105].

These activities have inspired researchers to create similar features on biomaterials to reduce bacterial colonization. Using the method of glancing angle sputter deposition (GLAD), Sengstock *et al.* [106,107] replicated the nanostructure of cicada wings on Ti surfaces and demonstrated antibacterial activities against *E. coli* [106]. The methods to create nano-scale features have been well summarized by Tripathy *et al.* in a recent review [66]. A number of different nano-scale features have been studied to date such as nanopillars [98,102] and nano spikes [108] on Si surfaces generated by plasma etching, diamond [61,109] and gold [103] substrates treated by anodization and plasma etching, carbon nanotubes created by chemical vapor deposition (CVD) [110], aluminum substrate etched by sodium hydroxide (NaOH) solution [111], nanowires and nano-size spikes made by hydrothermal processing [112–115], and nano rough Ti surfaces created by electron beam evaporation [116].

Compared to inorganic materials, fewer studies have been conducted with polymers presenting nanostructures. Xu *et al.* [117] fabricated 400/400 nm and 500/500 nm (diameter/height) nanopillars on polyurethane (PU) surfaces and reported up to 64% and 88% reduction of bacterial adhesion without doping S-nitroso-N-acetylpenicillamine (SNAP) and with SNAP doped layer, respectively. Using rigorous coupled-wave analysis (RCWA), Kim *et al.* [118] developed nanostructured PMMA film with both antireflective and antimicrobial properties.

Concurrent with the bactericidal effects, nanotopographies have been shown to affect bacterial physiology and morphology. For example, single-walled nanotubes (SWNTs) are effective in killing *E. coli* [110] and found to induce the expression of stress-related genes in *E. coli*. On modified PMMA films with nanopillars, attached *E. coli* cells appear to be longer and flatter than those on flat surfaces. The elongation (filamentous growth) is thought to indicate the stress of these cells [119–122].

In addition to bactericidal effects directly from physical interactions, nanostructures have been engineered to reduce biofouling by altering the local chemical environment or releasing antimicrobials. Nano roughness has been shown to increase the adsorption of the protein casein, which reduces bacterial attachment [123]. Nanotubes have been used to load antibiotics and inhibit bacterial colonization. Popat *et al.* [18] used anodization techniques to fabricate nanotubes on Ti surfaces. Loading gentamicin in these nanotubes can reduce bacterial colonization by 70% during 4 h but promote the proliferation of preosteoblastic cells, compared to Ti and Ti with drug-free nanotubes. Hizal *et al.* [124] demonstrated bacteria triggered the release of antibiotics on nanostructured Ti, modified with layer by layer coating of tannic acid/gentamicin, although the 3D nanostructure itself does not have antimicrobial effects.

A number of studies reported different effects of nanostructures on bacteria and mammalian cells and the possibility to selectively kill bacteria more than mammalian cells [105,115,125–128]. This field would benefit from future studies to develop rational designs with different effects on microbes and host cells.

Overall, a number of bioinspired and synthetic systems of micron- and nano-scale topographies have been engineered and exhibited effective antifouling activities (Figure 2.3). However, a vast majority of studies to date are rather empirical and the roles of bacterial factors are not well explored. Further development in this field will benefit from a more in-depth understanding of bacteria-material interactions, especially how bacteria sense and respond to such surface features (how bacteria read the map).

Microtopography   **Nanotopography**
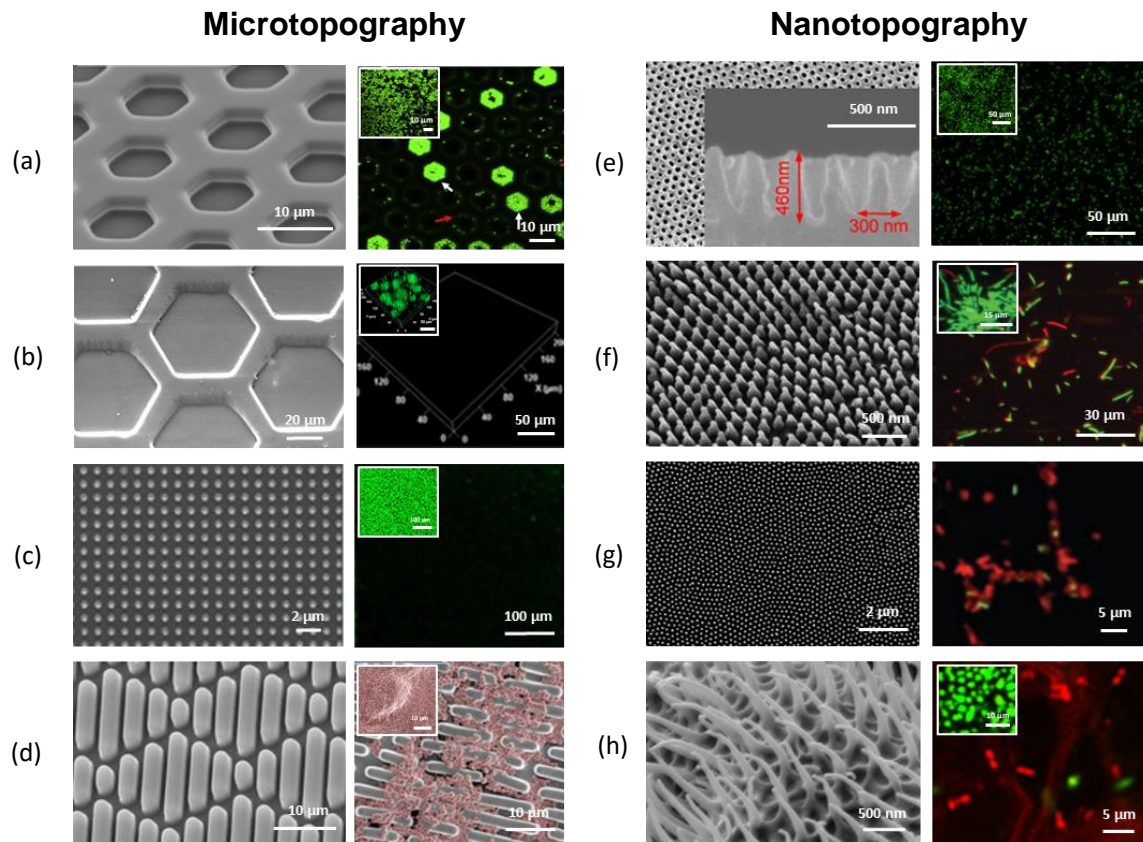
Figure 2.3. Reduction of bacterial attachment by using micron- and nano-scale topographies. (a-d) SEM images (left) and fluorescent microscopic images (right) of bacterial attachment on hexagonal PDMS pits (a), hexagonal recessive PDMS features (b), micropillars (c) Sharklet™ patterned surfaces (d). Reproduced with permission from refs [44,83,91,129]. (e-h) Bacterial attachment on nanotopographies. SEM images (left) and fluorescent microscopic images (right) of bacterial attachments (right insets; bacterial attachment on flat control surfaces) on a fabricated surface with nanostructure (e), nanopillars (f), cicada wings (g), and gecko skins (h). The small images show cell attachment on flat control surfaces. Image reproduced with permission from refs [36,97,105,118]. The SEM image b was taken for this manuscript.

2.5.3 Dynamic surface topography

Conceptually, preventing bacteria from attaching to a surface can avoid subsequent biofilm formation and associated detrimental effects. However, no surface developed to date can prevent bacterial attachment indefinitely. While static topographies with specific micron or nano-scale features may initially prevent bacterial adhesion and biofilm formation, cells that manage to attach tend to multiply and overcome these features eventually. For surfaces that have bactericidal effects, it is also possible that dead cells may protect other cells that attach to them. To obtain long-term biofilm control, it is important to develop technologies that can remove established biofilms. Epstein *et al.* [130] developed a synthetic platform that can create up to 2 µm dynamic wrinkles of PDMS through uniaxial mechanical strain and demonstrated up to 80% removal of 24 h *P. aeruginosa* biofilms. Shivapooja *et al.* produced active topography by applying pneumatic actuation [131] and electrical voltage [132] to the surfaces and obtained more than 90% removal of *E. coli* biofilms and 80% *Cobetia* marina biofilms. Gu *et al.* [133] recently fabricated a dynamic substrate using *a tert*-butylacrylate-based shape memory polymer with microscale hexagon topography. The patterns alone reduced 48h biofilm formation by ~

50%. By triggering on-demand shape recovery with mild heating (to 40°C), dynamic changes in patterned surface topography led to potent removal of established biofilms (up to 3 logs, 99.9%) of *P. aeruginosa*, *E. coli*, and *S. aureus*. The detached cells were also found more susceptible to antibiotics [134]. Levering *et al.* [135] reported a design of an on-demand fouling-release urinary catheter, which detached mature *P. mirabilis* biofilm by up to 90% through hydraulic and pneumatic actuation. Besides biofilm removal, the motion of the surface has been shown to increase the antifouling activities of static topographies. For example, the bactericidal effects of Titania (TiO$_2$) nanowire arrays were found to be stronger on upright surfaces with shaking compared to static cultures [115]. Similarly, on surfaces with nanofeatures, bacterial motility may contribute to the killing effects. Nano-topography exhibited cell piercing activities regardless of the motility of cells but was more effective where mechanical motion was part of the interaction between device and microbes [115].

2.5.4 Active surface topography

Recently, Gu *et al*. [136] engineered magnetically driven active topographies for long-term biofilm control (Figure 2.4). By creating micron-sized pillars with super-paramagnetic nanoparticles loaded in the pillar tips, the surfaces can both repel bacteria from attaching and remove established biofilms by tuning the beating frequency and bending angle (thus beating force) of the pillars. A prototype catheter was engineered based on this design, which remained clean for more than 30 days with the challenge of artificial urine medium and uropathogenic *E. coli* (UPEC), while the flat and static controls were blocked by UPEC biofilms within 5 and 3 days, respectively. Future design of smart medical devices also needs the capability to detect biofilm formation *in situ*. One possibility is to integrate impedimetric sensors into medical devices.
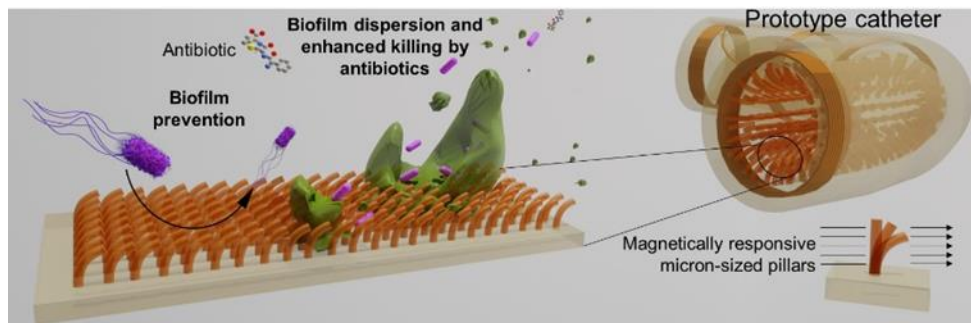
Figure 2.4. Active topography for long-term biofilm control. An antifouling surface was achieved by the programmable beating of micron-sized pillars driven by a tunable magnetic field. Image reproduced with permission from ref [136].

2.5 References

[1]   H.C. Flemming, J. Wingender, The biofilm matrix, Nat. Rev. Microbiol. 8 (2010) 623–633. https://doi.org/10.1038/nrmicro2415.

[2]   L. Hall-Stoodley, J.W. Costerton, P. Stoodley, Bacterial biofilms: From the natural environment to infectious diseases, Nat. Rev. Microbiol. 2 (2004) 95–108. https://doi.org/10.1038/nrmicro821.

[3]   I. Olsen, Biofilm-specific antibiotic tolerance and resistance, Eur. J. Clin. Microbiol. Infect. Dis. 34 (2015) 877–886. https://doi.org/10.1007/s10096-015-2323-z.

[4]   C.W. Hall, T.F. Mah, Molecular mechanisms of biofilm-based antibiotic resistance and tolerance in pathogenic bacteria, FEMS Microbiol. Rev. 41 (2017) 276–301. https://doi.org/10.1093/femsre/fux010.

[5]   R.D. Wolcott, G.D. Ehrlich, Biofilms and chronic infections, JAMA - J. Am. Med. Assoc. 299 (2008) 2682–2684. https://doi.org/10.1001/jama.299.22.2682.

[6]   C. for B.E. MSU, What are biofilms?, (n.d.). http://www.biofilm.montana.edu/biofilm-basics/what_are_biofilms.html.

[7]   Z. Khatoon, C.D. McTiernan, E.J. Suuronen, T.-F. Mah, E.I. Alarcon, Bacterial biofilm formation on implantable devices and approaches to its treatment and prevention, Heliyon. 4 (2018) e01067. https://doi.org/10.1016/j.heliyon.2018.e01067.

[8]   L.M. Weiner-Lastinger, S. Abner, J.R. Edwards, A.J. Kallen, M. Karlsson, S.S. Magill, D. Pollock, I. See, M.M. Soe, M.S. Walters, M.A. Dudeck, Antimicrobial-resistant pathogens associated with adult healthcare-associated infections: Summary of data reported to the

National Healthcare Safety Network, 2015–2017, Infect. Control Hosp. Epidemiol. 41 (2020) 1–18. https://doi.org/10.1017/ice.2019.296.

[9]   S.L. Percival, L. Suleman, C. Vuotto, G. Donelli, Healthcare-Associated infections, medical devices and biofilms: Risk, tolerance and control, J. Med. Microbiol. 64 (2015) 323–334. https://doi.org/10.1099/jmm.0.000032.

[10]   S. Veerachamy, T. Yarlagadda, G. Manivasagam, P.K. Yarlagadda, Bacterial adherence and biofilm formation on medical implants: A review, Proc. Inst. Mech. Eng. Part H J. Eng. Med. 228 (2014) 1083–1099. https://doi.org/10.1177/0954411914556137.

[11]   IMARC Group, Implantable Medical Devices Market: Global Industry Trends, Share, Size, Growth, Opportunity and Forecast 2019-2024, 2019.

[12]   Centers for Disease Control and Prevention, Number of all-listed procedures for discharges from short-stay hospitals, 2010.

[13]   P. Sreeramoju, Preventing Healthcare-Associated Infections, Am. J. Med. Sci. (2012) 1. https://doi.org/10.1097/MAJ.0b013e31824435e6.

[14]   X. Zhang, L. Wang, E. Levänen, Superhydrophobic surfaces for the reduction of bacterial adhesion, RSC Adv. 3 (2013) 12003. https://doi.org/10.1039/c3ra40497h.

[15]   A. Ewald, S.K. Glückermann, R. Thull, U. Gbureck, D. Lew, Antimicrobial titanium/silver PVD coatings on titanium, Biomed. Eng. Online. 5 (2006) 22. https://doi.org/10.1186/1475-925X-5-22.

[16]   L. Zhao, P.K. Chu, Y. Zhang, Z. Wu, Antibacterial coatings on titanium implants, J. Biomed. Mater. Res. - Part B Appl. Biomater. 91 (2009) 470–480.

https://doi.org/10.1002/jbm.b.31463.

[17]   J. Ma, Y. Sun, K. Gleichauf, J. Lou, Q. Li, Nanostructure on taro leaves resists fouling by colloids and bacteria under submerged conditions, Langmuir. 27 (2011) 10035–10040. https://doi.org/10.1021/la2010024.

[18]   K.C. Popat, M. Eltgroth, T.J. LaTempa, C.A. Grimes, T.A. Desai, Decreased Staphylococcus epidermis adhesion and increased osteoblast functionality on antibiotic-loaded titania nanotubes, Biomaterials. 28 (2007) 4880–4888. https://doi.org/10.1016/j.biomaterials.2007.07.037.

[19]   J.R. Chambers, K.E. Cherny, K. Sauer, Susceptibility of Pseudomonas aeruginosa dispersed cells to antimicrobial agents is dependent on the dispersion cue and class of the antimicrobial agent used, Antimicrob. Agents Chemother. 61 (2017) 1–18. https://doi.org/10.1128/AAC.00846-17.

[20]   A.D. Russell, W.B. Hugo, Antimicrobial Activity and Action of Silver, Prog. Med. Chem. 31 (1994) 351–370. https://doi.org/10.1016/S0079-6468(08)70024-9.

[21]   J.S. Price, A.F. Tencer, D.M. Arm, G.A. Bohach, Controlled release of antibiotics from coated orthopedic implants, J. Biomed. Mater. Res. 30 (1996) 281–286. https://doi.org/10.1002/(SICI)1097-4636(199603)30:3<281::AID-JBM2>3.0.CO;2-M.

[22]   W.H. Kim, S.B. Lee, K.T. Oh, S.K. Moon, K.M. Kim, K.N. Kim, The release behavior of CHX from polymer-coated titanium surfaces, Surf. Interface Anal. 40 (2008) 202–204. https://doi.org/10.1002/sia.2809.

[23]   J. Hasan, R.J. Crawford, E.P. Ivanova, Antibacterial surfaces: The quest for a new

generation of biomaterials, Trends Biotechnol. 31 (2013) 295–304.

https://doi.org/10.1016/j.tibtech.2013.01.017.

[24]   E. Fadeeva, V.K. Truong, M. Stiesch, B.N. Chichkov, R.J. Crawford, J. Wang, E.P.

Ivanova, Bacterial retention on superhydrophobic titanium surfaces fabricated by

femtosecond laser ablation, Langmuir. 27 (2011) 3012–3019.

https://doi.org/10.1021/la104607g.

[25]   E.B.H. Hume, J. Baveja, B. Muir, T.L. Schubert, N. Kumar, S. Kjelleberg, H.J. Griesser,

H. Thissen, R. Read, L.A. Poole-Warren, K. Schindhelm, M.D.P. Willcox, The control of

Staphylococcus epidermidis biofilm formation and in vivo infection rates by covalently

bound furanones, Biomaterials. 25 (2004) 5023–5030.

https://doi.org/10.1016/j.biomaterials.2004.01.048.

[26]   D. Campoccia, L. Montanaro, C.R. Arciola, A review of the biomaterials technologies for

infection-resistant surfaces, Biomaterials. 34 (2013) 8533–8554.

https://doi.org/10.1016/j.biomaterials.2013.07.089.

[27]   F. Mabboux, L. Ponsonnet, J.J. Morrier, N. Jaffrezic, O. Barsotti, Surface free energy and

bacterial retention to saliva-coated dental implant materials - An in vitro study, Colloids

Surfaces B Biointerfaces. 39 (2004) 199–205.

https://doi.org/10.1016/j.colsurfb.2004.08.002.

[28]   A.I. Hochbaum, J. Aizenberg, Bacteria pattern spontaneously on periodic nanostructure

arrays, Nano Lett. 10 (2010) 3717–3721. https://doi.org/10.1021/nl102290k.

[29]   H. Gu, K.W. Kolewe, D. Ren, Conjugation in Escherichia coli Biofilms on

Poly(dimethylsiloxane) Surfaces with Microtopographic Patterns, Langmuir. 33 (2017)

3142–3150. https://doi.org/10.1021/acs.langmuir.6b04679.

[30] R. Xing, S.P. Lyngstadaas, J.E. Ellingsen, S. Taxt-Lamolle, H.J. Haugen, The influence of surface nanoroughness, texture and chemistry of TiZr implant abutment on oral biofilm accumulation, Clin. Oral Implants Res. 26 (2015) 649–656. https://doi.org/10.1111/clr.12354.

[31] K. Anselme, P. Davidson, A.M. Popa, M. Giazzon, M. Liley, L. Ploux, The interaction of cells and bacteria with surfaces structured at the nanometre scale, Acta Biomater. 6 (2010) 3824–3846. https://doi.org/10.1016/j.actbio.2010.04.001.

[32] H. Yan Lin, Y. Liu, D. Wismeijer, W. Crielaard, D. Mei Deng, Effects of Oral Implant Surface Roughness on Bacterial Biofilm Formation and Treatment Efficacy, Int. J. Oral Maxillofac. Implants. 28 (2013) 1226–1231. https://doi.org/10.11607/jomi.3099.

[33] H. Gu, A. Chen, X. Song, M.E. Brasch, J.H. Henderson, D. Ren, How Escherichia coli lands and forms cell clusters on a surface: A new role of surface topography, Sci. Rep. 6 (2016) 1–14. https://doi.org/10.1038/srep29516.

[34] A. Ionescu, E. Wutscher, E. Brambilla, S. Schneider-Feyrer, F.J. Giessibl, S. Hahnel, Influence of surface properties of resin-based composites on in vitro Streptococcus mutans biofilm development, Eur. J. Oral Sci. 120 (2012) 458–465. https://doi.org/10.1111/j.1600-0722.2012.00983.x.

[35] H. Gu, D. Ren, Materials and surface engineering to control bacterial adhesion and biofilm formation: A review of recent advances, Front. Chem. Sci. Eng. 8 (2014) 20–33. https://doi.org/10.1007/s11705-014-1412-3.

[36] M.N. Dickson, E.I. Liang, L.A. Rodriguez, N. Vollereaux, A.F. Yee, Nanopatterned polymer surfaces with bactericidal properties, Biointerphases. 10 (2015) 021010. https://doi.org/10.1116/1.4922157.

[37] D. Siegismund, A. Undisz, S. Germerodt, S. Schuster, M. Rettenmayr, Quantification of the interaction between biomaterial surfaces and bacteria by 3-D modeling, Acta Biomater. 10 (2014) 267–275. https://doi.org/10.1016/j.actbio.2013.09.016.

[38] P. Ball, Shark skin and other solutions, Nat. Eng. 400 (1999) 507–508. https://doi.org/10.1038/22883.

[39] D. Perera-Costa, J.M. Bruque, M.L. González-Martín, A.C. Gómez-García, V. Vadillo-Rodríguez, Studying the influence of surface topography on bacterial adhesion using spatially organized microtopographic surface patterns, Langmuir. 30 (2014) 4633–4641. https://doi.org/10.1021/la5001057.

[40] F. Song, H. Wang, K. Sauer, D. Ren, Cyclic-di-GMP and oprF are involved in the response of Pseudomonas aeruginosa to substrate material stiffness during attachment on polydimethylsiloxane (PDMS), Front. Microbiol. 9 (2018) 1–13. https://doi.org/10.3389/fmicb.2018.00110.

[41] F. Song, M.E. Brasch, H. Wang, J.H. Henderson, K. Sauer, D. Ren, How Bacteria Respond to Material Stiffness during Attachment: A Role of Escherichia coli Flagellar Motility, ACS Appl. Mater. Interfaces. 9 (2017) 22176–22184. https://doi.org/10.1021/acsami.7b04757.

[42] Y. Zhao, F. Song, H. Wang, J. Zhou, D. Ren, Phagocytosis of Escherichia coli biofilm cells with different aspect ratios: a role of substratum material stiffness, Appl. Microbiol.

Biotechnol. 101 (2017) 6473–6481. https://doi.org/10.1007/s00253-017-8394-2.

[43] F. Song, D. Ren, Stiffness of cross-linked poly(dimethylsiloxane) affects bacterial adhesion and antibiotic susceptibility of attached cells, Langmuir. 30 (2014) 10354– 10362. https://doi.org/10.1021/la502029f.

[44] K.K. Chung, J.F. Schumacher, E.M. Sampson, R.A. Burne, P.J. Antonelli, A.B. Brennan, Impact of engineered surface microtopography on biofilm formation of Staphylococcus aureus , Biointerphases. 2 (2007) 89–94. https://doi.org/10.1116/1.2751405.

[45] H. Koo, R.N. Allan, R.P. Howlin, P. Stoodley, L. Hall-Stoodley, Targeting microbial biofilms: Current and prospective therapeutic strategies, Nat. Rev. Microbiol. 15 (2017) 740–755. https://doi.org/10.1038/nrmicro.2017.99.

[46] Y.R. Chang, E.R. Weeks, W.A. Ducker, Surface Topography Hinders Bacterial Surface Motility, ACS Appl. Mater. Interfaces. 10 (2018) 9225–9234. https://doi.org/10.1021/acsami.7b16715.

[47] R.S. Friedlander, H. Vlamakis, P. Kim, M. Khan, R. Kolter, J. Aizenberg, Bacterial flagella explore microscale hummocks and hollows to increase adhesion, Proc. Natl. Acad. Sci. U. S. A. 110 (2013) 5624–5629. https://doi.org/10.1073/pnas.1219662110.

[48] L. Rizzello, B. Sorce, S. Sabella, G. Vecchio, A. Galeone, V. Brunetti, R. Cingolani, P.P. Pompa, Impact of Nanoscale Topography on Genomics and Proteomics of Adherent Bacteria, ACS Nano. 5 (2011) 1865–1876. https://doi.org/10.1021/nn102692m.

[49] V.D. Gordon, L. Wang, Bacterial mechanosensing: the force will be with you, always, J. Cell Sci. 132 (2019) jcs227694. https://doi.org/10.1242/jcs.227694.

[50] F. Hizal, C.H. Choi, H.J. Busscher, H.C. Van Der Mei, Staphylococcal Adhesion, Detachment and Transmission on Nanopillared Si Surfaces, ACS Appl. Mater. Interfaces. 8 (2016) 30430–30439. https://doi.org/10.1021/acsami.6b09437.

[51] V. Carniello, B.W. Peterson, H.C. van der Mei, H.J. Busscher, Physico-chemistry from initial bacterial adhesion to surface-programmed biofilm growth, Adv. Colloid Interface Sci. 261 (2018) 1–14. https://doi.org/10.1016/j.cis.2018.10.005.

[52] E. Lauga, W.R. DiLuzio, G.M. Whitesides, H.A. Stone, Swimming in Circles: Motion of Bacteria near Solid Boundaries, Biophys. J. 90 (2006) 400–412. https://doi.org/10.1529/biophysj.105.069401.

[53] P.P. Lele, B.G. Hosu, H.C. Berg, Dynamics of mechanosensing in the bacterial flagellar motor, Proc. Natl. Acad. Sci. U. S. A. 110 (2013) 11839–11844. https://doi.org/10.1073/pnas.1305885110.

[54] J. Männik, R. Driessen, P. Galajda, J.E. Keymer, C. Dekker, Bacterial growth and motility in sub-micron constrictions, Proc. Natl. Acad. Sci. U. S. A. 106 (2009) 14861–14866. https://doi.org/10.1073/pnas.0907542106.

[55] H. Wioland, E. Lushi, R.E. Goldstein, Directed collective motion of bacteria under channel confinement, New J. Phys. 18 (2016). https://doi.org/10.1088/1367-2630/18/7/075002.

[56] Y.-R. Chang, E. R. Weeks, D. Barton, J. Dobnikar, W. A. Ducker, Effect of Topographical Steps on the Surface Motility of the Bacterium Pseudomonas aeruginosa, ACS Biomater. Sci. & Eng. 0 (2019). https://doi.org/10.1021/acsbiomaterials.9b00729.

[57] H. Gu, A. Chen, X. Song, M.E. Brasch, J.H. Henderson, D. Ren, How Escherichia coli lands and forms cell clusters on a surface: A new role of surface topography, Sci. Rep. 6 (2016) 1–14. https://doi.org/10.1038/srep29516.

[58] G. Feng, Y. Cheng, S.Y. Wang, L.C. Hsu, Y. Feliz, D.A. Borca-Tasciuc, R.W. Worobo, C.I. Moraru, Alumina surfaces with nanoscale topography reduce attachment and biofilm formation by Escherichia coli and Listeria spp, Biofouling. 30 (2014) 1253–1268. https://doi.org/10.1080/08927014.2014.976561.

[59] C.D. Bandara, S. Singh, I.O. Afara, A. Wolff, T. Tesfamichael, K. Ostrikov, A. Oloyede, Bactericidal Effects of Natural Nanotopography of Dragonfly Wing on Escherichia coli, ACS Appl. Mater. Interfaces. 9 (2017) 6746–6760. https://doi.org/10.1021/acsami.6b13666.

[60] S. Wu, F. Zuber, K. Maniura-Weber, J. Brugger, Q. Ren, Nanostructured surface topographies have an effect on bactericidal activity, J. Nanobiotechnology. 16 (2018) 1–9. https://doi.org/10.1186/s12951-018-0347-0.

[61] L.E. Fisher, Y. Yang, M. Yuen, W. Zhang, A.H. Nobbs, B. Su, Bactericidal activity of biomimetic diamond nanocone surfaces, Biointerphases. 11 (2016) 011014. https://doi.org/10.1116/1.4944062.

[62] D.P. Linklater, S. Juodkazis, E.P. Ivanova, Nanofabrication of mechano-bactericidal surfaces, Nanoscale. 9 (2017) 16564–16585. https://doi.org/10.1039/c7nr05881k.

[63] M. V. Graham, N.C. Cady, Nano and microscale topographies for the prevention of bacterial surface fouling, Coatings. 4 (2014) 37–59. https://doi.org/10.3390/coatings4010037.

[64]   S. Wu, B. Zhang, Y. Liu, X. Suo, H. Li, Influence of surface topography on bacterial

       adhesion: A review (Review), Biointerphases. 13 (2018) 060801.

       https://doi.org/10.1116/1.5054057.

[65]   J. Hasan, K. Chatterjee, Recent advances in engineering topography mediated antibacterial

       surfaces, Nanoscale. 7 (2015) 15568–15575. https://doi.org/10.1039/c5nr04156b.

[66]   A. Tripathy, P. Sen, B. Su, W.H. Briscoe, Natural and bioinspired nanostructured

       bactericidal surfaces, Adv. Colloid Interface Sci. 248 (2017) 85–104.

       https://doi.org/10.1016/j.cis.2017.07.030.

[67]   U.S. Food and Drug Administration, Breast Implant-Associated Anaplastic Large Cell

       Lymphoma (BIA-ALCL), (2019). https://www.fda.gov/medical-devices/breast-

       implants/breast-implant-associated-anaplastic-large-cell-lymphoma-bia-alcl.

[68]   H. Hu, K. Johani, A. Almatroudi, K. Vickery, B. Van Natta, M.E. Kadin, G. Brody, M.

       Clemens, C.Y. Cheah, S. Lade, P.A. Joshi, H.M. Prince, A.K. Deva, Bacterial Biofilm

       Infection Detected in Breast Implant-Associated Anaplastic Large-Cell Lymphoma, Plast.

       Reconstr. Surg. 137 (2016) 1659–1669. https://doi.org/10.1097/PRS.0000000000002010.

[69]   S. Hoda, R. Rao, R.S. Hoda, Breast Implant-Associated Anaplastic Large Cell

       Lymphoma, Int. J. Surg. Pathol. 23 (2015) 209–210.

       https://doi.org/10.1177/1066896915576406.

[70]   M. Magnusson, K. Beath, R. Cooter, M. Locke, H.M. Prince, E. Elder, A.K. Deva, The

       Epidemiology of Breast Implant-Associated Anaplastic Large Cell Lymphoma in

       Australia and New Zealand Confirms the Highest Risk for Grade 4 Surface Breast

       Implants, Plast. Reconstr. Surg. 143 (2019) 1285–1292.

https://doi.org/10.1097/PRS.0000000000005500.

[71] A. Loch-Wilkinson, K.J. Beath, R.J.W. Knight, W.L.F. Wessels, M. Magnusson, T. Papadopoulos, T. Connell, J. Lofts, M. Locke, I. Hopper, R. Cooter, K. Vickery, P.A. Joshi, H.M. Prince, A.K. Deva, Breast implant-associated anaplastic large cell lymphoma in Australia and New Zealand: High-surface-area textured implants are associated with increased risk, Plast. Reconstr. Surg. 140 (2017) 645–654. https://doi.org/10.1097/PRS.0000000000003654.

[72] B.H. Shin, B.H. Kim, S. Kim, K. Lee, Y. Bin Choy, C.Y. Heo, Silicone breast implant modification review: Overcoming capsular contracture, Biomater. Res. 22 (2018) 37. https://doi.org/10.1186/s40824-018-0147-5.

[73] M. Atlan, G. Nuti, H. Wang, S. Decker, T.A. Perry, Breast implant surface texture impacts host tissue response, J. Mech. Behav. Biomed. Mater. 88 (2018) 377–385. https://doi.org/10.1016/j.jmbbm.2018.08.035.

[74] U.S. Food and Drug Administration, Statement from Binita Ashar, M.D., of the FDA's Center for Devices and Radiological Health on agency's commitment to studying breast implant safety, (2018). https://www.fda.gov/news-events/press-announcements/statement-binita-ashar-md-fdas-center-devices-and-radiological-health-agencys-commitment-studying.

[75] International Organization for Standardization, ISO 10993-1:2018(en) Biological evaluation of medical devices — Part 1: Evaluation and testing within a risk management process, (2018). https://www.iso.org/obp/ui/#iso:std:iso:10993:-1:ed-5:v2:en.

[76] International Organization for Standardization, ISO 14602 - Non-active surgical implants

- Implants for osteosynthesis - Particular requirements, (2018).
https://www.iso.org/obp/ui/#iso:std:iso:14607:ed-3:v2:en.

[77] World Health Organization, Silicone implants, (2012).
https://www.who.int/csr/don/2012_01_17/en/.

[78] B. Zhang, Y. Luo, A.J. Pearlstein, J. Aplin, Y. Liu, G.R. Bauchan, G.F. Payne, Q. Wang, X. Nou, P.D. Millner, Fabrication of biomimetically patterned surfaces and their application to probing plant-bacteria interactions, ACS Appl. Mater. Interfaces. 6 (2014) 12467–12478. https://doi.org/10.1021/am502384q.

[79] H. Pingle, P.Y. Wang, H. Thissen, P. Kingshott, Controlled Attachment of Pseudomonas aeruginosa with Binary Colloidal Crystal-Based Topographies, Small. 14 (2018) 1703574. https://doi.org/10.1002/smll.201703574.

[80] J. Valle, S. Burgui, D. Langheinrich, C. Gil, C. Solano, A. Toledo-Arana, R. Helbig, A. Lasagni, I. Lasa, Evaluation of Surface Microtopography Engineered by Direct Laser Interference for Bacterial Anti-Biofouling, Macromol. Biosci. 15 (2015) 1060–1069. https://doi.org/10.1002/mabi.201500107.

[81] Y. Wang, J.F. da Silva Domingues, G. Subbiahdoss, H.C. van der Mei, H.J. Busscher, M. Libera, Conditions of lateral surface confinement that promote tissue-cell integration and inhibit biofilm growth, Biomaterials. 35 (2014) 5446–5452. https://doi.org/10.1016/j.biomaterials.2014.03.057.

[82] L. Wang, W. Chen, E. Terentjev, Effect of micro-patterning on bacterial adhesion on polyethylene terephthalate surface, J. Biomater. Appl. 29 (2015) 1351–1362. https://doi.org/10.1177/0885328214563998.

[83] X. Ge, Y. Leng, X. Lu, F. Ren, K. Wang, Y. Ding, M. Yang, Bacterial responses to periodic micropillar array, J. Biomed. Mater. Res. - Part A. 103 (2015) 384–396. https://doi.org/10.1002/jbm.a.35182.

[84] M. Yang, Y. Ding, X. Ge, Y. Leng, Control of bacterial adhesion and growth on honeycomb-like patterned surfaces, Colloids Surfaces B Biointerfaces. 135 (2015) 549–555. https://doi.org/10.1016/j.colsurfb.2015.08.010.

[85] N. Mitik-Dineva, J. Wang, V.K. Truong, P.R. Stoddart, M.R. Alexander, D.J. Albutt, C. Fluke, R.J. Crawford, E.P. Ivanova, Bacterial attachment on optical fibre surfaces., Biofouling. 26 (2010) 461–470. https://doi.org/10.1080/08927011003753399.

[86] W.S. Jeong, J.S. Kwon, J.H. Lee, S.H. Uhm, E. Ha Choi, K.M. Kim, Bacterial attachment on titanium surfaces is dependent on topography and chemical changes induced by nonthermal atmospheric pressure plasma, Biomed. Mater. 12 (2017) 045015. https://doi.org/10.1088/1748-605X/aa734e.

[87] L.C. Hsu, J. Fang, D.A. Borca-Tasciuc, R.W. Worobo, C.I. Moraru, Effect of micro- and nanoscale topography on the adhesion of bacterial cells to solid surfaces, Appl. Environ. Microbiol. 79 (2013) 2703–2712. https://doi.org/10.1128/AEM.03436-12.

[88] S. Hou, H. Gu, C. Smith, D. Ren, Microtopographic patterns affect escherichia coli biofilm formation on poly(dimethylsiloxane) surfaces, Langmuir. 27 (2011) 2686–2691. https://doi.org/10.1021/la1046194.

[89] J. Lee, M.A. Pascall, Effect of micro-pattern topography on the attachment and survival of foodborne microorganisms on food contact surfaces, J. Food Saf. 38 (2018). https://doi.org/10.1111/jfs.12379.

[90] G.C. Ling, M.H. Low, M. Erken, S. Longford, S. Nielsen, A.J. Poole, P. Steinberg, D. McDougald, S. Kjelleberg, Micro-fabricated polydimethyl siloxane (PDMS) surfaces regulate the development of marine microbial biofilm communities, Biofouling. 30 (2014) 323–335. https://doi.org/10.1080/08927014.2013.872778.

[91] R. Vasudevan, A.J. Kennedy, M. Merritt, F.H. Crocker, R.H. Baney, Microscale patterned surfaces reduce bacterial fouling-microscopic and theoretical analysis, Colloids Surfaces B Biointerfaces. 117 (2014) 225–232. https://doi.org/10.1016/j.colsurfb.2014.02.037.

[92] N. Lu, W. Zhang, Y. Weng, X. Chen, Y. Cheng, P. Zhou, Fabrication of PDMS surfaces with micro patterns and the effect of pattern sizes on bacteria adhesion, Food Control. 68 (2016) 344–351. https://doi.org/10.1016/j.foodcont.2016.04.014.

[93] P. Halder, M. Nasabi, N. Jayasuriya, J. Shimeta, S. Bhattacharya, A. Mitchell, M.A. Bhuiyan, An assessment of the dynamic stability of microorganisms on patterned surfaces in relation to biofouling control, Biofouling. 30 (2014) 699–716. https://doi.org/10.1080/08927014.2014.914177.

[94] C. Díaz, P.L. Schilardi, R.C. Salvarezza, M. Fernández Lorenzo de Mele, Have flagella a preferred orientation during early stages of biofilm formation?: AFM study using patterned substrates, Colloids Surfaces B Biointerfaces. 82 (2011) 536–542. https://doi.org/10.1016/j.colsurfb.2010.10.013.

[95] L. Wang, W. Chen, E. Terentjev, Effect of micro-patterning on bacterial adhesion on polyethylene terephthalate surface, J. Biomater. Appl. 29 (2015) 1351–1362. https://doi.org/10.1177/0885328214563998.

[96] S. Pogodin, J. Hasan, V.A. Baulin, H.K. Webb, V.K. Truong, T.H. Phong Nguyen, V.

Boshkovikj, C.J. Fluke, G.S. Watson, J.A. Watson, R.J. Crawford, E.P. Ivanova, Biophysical model of bacterial cell interactions with nanopatterned cicada wing surfaces, Biophys. J. 104 (2013) 835–840. https://doi.org/10.1016/j.bpj.2012.12.046.

[97]   E.P. Ivanova, J. Hasan, H.K. Webb, V.K. Truong, G.S. Watson, J.A. Watson, V.A. Baulin, S. Pogodin, J.Y. Wang, M.J. Tobin, C. Löbbe, R.J. Crawford, Natural bactericidal surfaces: Mechanical rupture of pseudomonas aeruginosa cells by cicada wings, Small. 8 (2012) 2489–2494. https://doi.org/10.1002/smll.201200528.

[98]   J. Hasan, H.K. Webb, V.K. Truong, S. Pogodin, V.A. Baulin, G.S. Watson, J.A. Watson, R.J. Crawford, E.P. Ivanova, Selective bactericidal activity of nanopatterned superhydrophobic cicada Psaltoda claripennis wing surfaces, Appl. Microbiol. Biotechnol. 97 (2013) 9257–9262. https://doi.org/10.1007/s00253-012-4628-5.

[99]   D.H.K. Nguyen, C. Loebbe, D.P. Linklater, X. Xu, N. Vrancken, T. Katkus, S. Juodkazis, S. Maclaughlin, V. Baulin, R.J. Crawford, E.P. Ivanova, The idiosyncratic self-cleaning cycle of bacteria on regularly arrayed mechano-bactericidal nanostructures, Nanoscale. 11 (2019) 16455–16462. https://doi.org/10.1039/c9nr05923g.

[100] J. Hasan, S. Raj, L. Yadav, K. Chatterjee, Engineering a nanostructured "super surface" with superhydrophobic and superkilling properties, RSC Adv. 5 (2015) 44953–44959. https://doi.org/10.1039/c5ra05206h.

[101] D.P. Linklater, M. De Volder, V.A. Baulin, M. Werner, S. Jessl, M. Golozar, L. Maggini, S. Rubanov, E. Hanssen, S. Juodkazis, E.P. Ivanova, High Aspect Ratio Nanostructures Kill Bacteria via Storage and Release of Mechanical Energy, ACS Nano. 12 (2018) 6657–6667. https://doi.org/10.1021/acsnano.8b01665.

[102] E.P. Ivanova, J. Hasan, H.K. Webb, G. Gervinskas, S. Juodkazis, V.K. Truong, A.H.F. Wu, R.N. Lamb, V.A. Baulin, G.S. Watson, J.A. Watson, D.E. Mainwaring, R.J. Crawford, Bactericidal activity of black silicon, Nat. Commun. 4 (2013) 1–7. https://doi.org/10.1038/ncomms3838.

[103] S. Wu, F. Zuber, J. Brugger, K. Maniura-Weber, Q. Ren, Antibacterial Au nanostructured surfaces, Nanoscale. 8 (2016) 2620–2625. https://doi.org/10.1039/c5nr06157a.

[104] S.M. Kelleher, O. Habimana, J. Lawler, B. O'reilly, S. Daniels, E. Casey, A. Cowley, Cicada Wing Surface Topography: An Investigation into the Bactericidal Properties of Nanostructural Features, ACS Appl. Mater. Interfaces. 8 (2016) 14966–14974. https://doi.org/10.1021/acsami.5b08309.

[105] G.S. Watson, D.W. Green, L. Schwarzkopf, X. Li, B.W. Cribb, S. Myhra, J.A. Watson, A gecko skin micro/nano structure - A low adhesion, superhydrophobic, anti-wetting, self-cleaning, biocompatible, antibacterial surface, Acta Biomater. 21 (2015) 109–122. https://doi.org/10.1016/j.actbio.2015.03.007.

[106] C. Sengstock, M. Lopian, Y. Motemani, A. Borgmann, C. Khare, P.J.S. Buenconsejo, T.A. Schildhauer, A. Ludwig, M. Köller, Structure-related antibacterial activity of a titanium nanostructured surface fabricated by glancing angle sputter deposition, Nanotechnology. 25 (2014) 195101. https://doi.org/10.1088/0957-4484/25/19/195101.

[107] C. Sengstock, M. Lopian, A. Borgmann, Y. Motemani, C. Khare, T. Schildhauer, M. Köller, Titanium Nanostructured Surfaces Fabricated by Glancing Angle Sputter Deposition : Anti-bacterial Activity (Cicada Wing Effect) and Influence on Human Mesenchymal Stem Cells, in: ORS 2014 Annu. Meet., 2014.

[108] X. Wang, C.M. Bhadra, T.H. Yen Dang, R. Buividas, J. Wang, R.J. Crawford, E.P. Ivanova, S. Juodkazis, A bactericidal microfluidic device constructed using nano-textured black silicon, RSC Adv. 6 (2016) 26300–26306. https://doi.org/10.1039/c6ra03864f.

[109] P.W. May, M. Clegg, T.A. Silva, H. Zanin, O. Fatibello-Filho, V. Celorrio, D.J. Fermin, C.C. Welch, G. Hazell, L. Fisher, A. Nobbs, B. Su, Diamond-coated "black silicon" as a promising material for high-surface-area electrochemical electrodes and antibacterial surfaces, J. Mater. Chem. B. 4 (2016) 5737–5746. https://doi.org/10.1039/c6tb01774f.

[110] S. Kang, M. Herzberg, D.F. Rodrigues, M. Elimelech, Antibacterial effects of carbon nanotubes: Size does matter!, Langmuir. 24 (2008) 6409–6413. https://doi.org/10.1021/la800951v.

[111] J. Hasan, S. Jain, R. Padmarajan, S. Purighalla, V.K. Sambandamurthy, K. Chatterjee, Multi-scale surface topography to minimize adherence and viability of nosocomial drug-resistant bacteria, Mater. Des. 140 (2018) 332–344. https://doi.org/10.1016/j.matdes.2017.11.074.

[112] C.M. Bhadra, V. Khanh Truong, V.T.H. Pham, M. Al Kobaisi, G. Seniutinas, J.Y. Wang, S. Juodkazis, R.J. Crawford, E.P. Ivanova, Antibacterial titanium nano-patterned arrays inspired by dragonfly wings, Sci. Rep. 5 (2015) 1–12. https://doi.org/10.1038/srep16817.

[113] M. Lorenzetti, I. Dogša, T. Stošicki, D. Stopar, M. Kalin, S. Kobe, S. Novak, The Influence of Surface Modification on Bacterial Adhesion to Titanium-Based Substrates, ACS Appl. Mater. Interfaces. 7 (2015) 1644–1651. https://doi.org/10.1021/am507148n.

[114] T. Sjöström, A.H. Nobbs, B. Su, Bactericidal nanospike surfaces via thermal oxidation of Ti alloy substrates, Mater. Lett. 167 (2016) 22–26.

https://doi.org/10.1016/j.matlet.2015.12.140.

[115] T. Diu, N. Faruqui, T. Sjöström, B. Lamarre, H.F. Jenkinson, B. Su, M.G. Ryadnov, Cicada-inspired cell-instructive nanopatterned arrays, Sci. Rep. 4 (2014) 7122. https://doi.org/10.1038/srep07122.

[116] S.D. Puckett, E. Taylor, T. Raimondo, T.J. Webster, The relationship between the nanostructure of titanium surfaces and bacterial attachment, Biomaterials. 31 (2010) 706–713. https://doi.org/10.1016/j.biomaterials.2009.09.081.

[117] L.-C. Xu, Y. Wo, M.E. Meyerhoff, C.A. Siedlecki, Inhibition of bacterial adhesion and biofilm formation by dual functional textured and nitric oxide releasing surfaces, Acta Biomater. 51 (2017) 53–65. https://doi.org/10.1016/j.actbio.2017.01.030.

[118] S. Kim, U.T. Jung, S.K. Kim, J.H. Lee, H.S. Choi, C.S. Kim, M.Y. Jeong, Nanostructured multifunctional surface with antireflective and antimicrobial characteristics, ACS Appl. Mater. Interfaces. 7 (2015) 326–331. https://doi.org/10.1021/am506254r.

[119] S.S. Justice, D.A. Hunstad, L. Cegelski, S.J. Hultgren, Morphological plasticity as a bacterial survival strategy, Nat. Rev. Microbiol. 6 (2008) 162–168. https://doi.org/10.1038/nrmicro1820.

[120] M. Wainwright, L.T. Canham, K. Al-Wajeeh, C.L. Reeves, Morphological changes (including filamentation) in Escherichia coli grown under starvation conditions on silicon wafers and other surfaces, Lett. Appl. Microbiol. 29 (1999) 224–227. https://doi.org/10.1046/j.1365-2672.1999.00602.x.

[121] E.S. Giotis, I.S. Blair, D.A. McDowell, Morphological changes in Listeria monocytogenes

subjected to sublethal alkaline stress, Int. J. Food Microbiol. 120 (2007) 250–258. https://doi.org/10.1016/j.ijfoodmicro.2007.08.036.

[122] T.H. Jones, K.M. Vail, L.M. McMullen, Filament formation by foodborne bacteria under sublethal stress, Int. J. Food Microbiol. 165 (2013) 97–110. https://doi.org/10.1016/j.ijfoodmicro.2013.05.001.

[123] L. Liu, B. Ercan, L. Sun, K.S. Ziemer, T.J. Webster, Understanding the Role of Polymer Surface Nanoscale Topography on Inhibiting Bacteria Adhesion and Growth, ACS Biomater. Sci. Eng. 2 (2016) 122–130. https://doi.org/10.1021/acsbiomaterials.5b00431.

[124] F. Hizal, I. Zhuk, S. Sukhishvili, H.J. Busscher, H.C. Van Der Mei, C.H. Choi, Impact of 3D hierarchical nanostructures on the antibacterial efficacy of a bacteria-triggered self-defensive antibiotic coating, ACS Appl. Mater. Interfaces. 7 (2015) 20304–20313. https://doi.org/10.1021/acsami.5b05947.

[125] X. Li, Bactericidal mechanism of nanopatterned surfaces, Phys. Chem. Chem. Phys. 18 (2015) 1311–1316. https://doi.org/10.1039/c5cp05646b.

[126] G. Bhardwaj, T. Webster, Reduced bacterial growth and increased osteoblast proliferation on titanium with a nanophase TiO2 surface treatment, Int. J. Nanomedicine. Volume 12 (2017) 363–369. https://doi.org/10.2147/IJN.S116105.

[127] A. Rifai, N. Tran, P. Reineck, A. Elbourne, E. Mayes, A. Sarker, C. Dekiwadia, E.P. Ivanova, R.J. Crawford, T. Ohshima, B.C. Gibson, A.D. Greentree, E. Pirogova, K. Fox, Engineering the Interface: Nanodiamond Coating on 3D-Printed Titanium Promotes Mammalian Cell Growth and Inhibits Staphylococcus aureus Colonization, ACS Appl. Mater. Interfaces. 11 (2019) 24588–24597. https://doi.org/10.1021/acsami.9b07064.

[128] L. Ploux, K. Anselme, A. Dirani, A. Ponche, O. Soppera, V. Roucoules, Opposite responses of cells and bacteria to micro/nanopatterned surfaces prepared by pulsed plasma polymerization and UV-irradiation, Langmuir. 25 (2009) 8161–8169. https://doi.org/10.1021/la900457f.

[129] H. Gu, S.W. Lee, S.L. Buffington, J.H. Henderson, D. Ren, On-Demand Removal of Bacterial Biofilms via Shape Memory Activation, ACS Appl. Mater. Interfaces. 8 (2016) 21140–21144. https://doi.org/10.1021/acsami.6b06900.

[130] A.K. Epstein, D. Hong, P. Kim, J. Aizenberg, Biofilm attachment reduction on bioinspired, dynamic, micro-wrinkling surfaces, New J. Phys. 15 (2013). https://doi.org/10.1088/1367-2630/15/9/095018.

[131] P. Shivapooja, Q. Wang, L.M. Szott, B. Orihuela, D. Rittschof, X. Zhao, G.P. López, Dynamic surface deformation of silicone elastomers for management of marine biofouling: laboratory and field studies using pneumatic actuation, Biofouling. 31 (2015) 265–274. https://doi.org/10.1080/08927014.2015.1035651.

[132] P. Shivapooja, Q. Wang, B. Orihuela, D. Rittschof, G.P. Lõpez, X. Zhao, Bioinspired surfaces with dynamic topography for active control of biofouling, Adv. Mater. 25 (2013) 1430–1434. https://doi.org/10.1002/adma.201203374.

[133] H. Gu, S.W. Lee, S.L. Buffington, J.H. Henderson, D. Ren, On-Demand Removal of Bacterial Biofilms via Shape Memory Activation, ACS Appl. Mater. Interfaces. 8 (2016) 21140–21144. https://doi.org/10.1021/acsami.6b06900.

[134] S.W. Lee, H. Gu, J.B. Kilberg, D. Ren, Sensitizing bacterial cells to antibiotics by shape recovery triggered biofilm dispersion, Acta Biomater. 81 (2018) 93–102.

https://doi.org/10.1016/j.actbio.2018.09.042.

[135] V. Leveri, Q. Wang, P. Shivapooja, X. Zhao, G.P. Lõpez, Soft Robotic Concepts in Catheter Design: an On-demand Fouling-release Urinary Catheter, Adv Heal. Mater. 3 (2014) 1588–1596. https://doi.org/10.1002/ana.22528.Toll-like.

[136] H. Gu, S.W. Lee, J. Carnicelli, T. Zhang, D. Ren, Magnetically driven active topography for long-term biofilm control, Nat. Commun. 11 (2020) 2211. https://doi.org/10.1038/s41467-020-16055-5.

Chapter 3

Effects of static surface topography on *E. coli* RP437/pRSH103 attachment

and its biofilm formation

3.1 Abstract

Recent years have witnessed increasing cases of breast implant-associated anaplastic large cell lymphoma (BIA-ALCL) related to textured implants. Researchers and regulatory authorities have started to investigate the correlation between bacterial colonization of textured breast implants and BIA-ALCL. However, it is still unclear how bacterial colonization may cause BIA-ALCL.

In this study, we developed a high-throughput approach to quantify bacterial adhesion on a library of differentially textured surfaces. By varying the size of features and the distance between features, we were able to specify the relationship between recessive surface topography and bacterial adhesion. The attachment behavior of a Gram-negative bacterium *Escherichia coli* was investigated under both static and dynamic fluid conditions. Our results indicate that *E. coli* prefers to attach in recessive features than bridges between features. Similar results were obtained from the features mimicking commercial breast implants associated with BIA-ALCL. We speculate that bacteria attached in the area of the interfacial junction may evade host immune clearance and trigger inflammation leading to BIA-ALCL. These results provide new information helpful for classifying implants for the risk of BIA-ALCL.

3.2 Introduction

The US Food and Drug Administration (FDA) has received 573 medical device reports (MDRs) as of July 6, 2019 [1]. A total of 385 reports (67%) among these MDRs are related to textured breast implant devices. There were 15 deaths, which covers 48% of the textured breast implant devices out of a total of 33 anaplastic large cell lymphoma (ALCL) deaths. On the other hand, only 5% and 3% for MDRs and ALCL deaths, respectively, were resulted from the smooth breast implant devices. Due to the strong correlation between textured breast implants and breast implant-associated ALCL (BIA-ALCL), FDA announced on July 24, 2019, that one of the manufacturers, Allergan, to recall their textured breast implant, Natrelle Biocell [2].

As concerns of BIA-ALCL increase, intensive studies were conducted to identify the correlation between textured breast implant devices and BIA-ALCL [3–11]. It is hypothesized that bacterial attachment causes BIA-ALCL [3–6]. Hu *et al.* [4] discovered bacterial biofilm formation on implants associated with BIA-ALCL; and *Ralstonia* spp. were dominantly observed from ALCL specimens while more portion of *Staphylococcus* spp. was found from non-tumor capsule specimens. From a study of pig model, a linear correlation was found between the number of bacteria detected and the number of T and B cells, which can be related to the incidence of ALCL [3]. This is not surprising since chronic biofilm infection may cause T-cell hyperplasia [3]. However, Walker *et al.* [7] reported recently that there was no difference in bacterial observed between BIA-ALCL and control specimens. Other hypotheses were also suggested. Hallalb *et al.* [12] claimed the increased numbers of breast implant debris may cause a high level of pathogenic inflammation, which is related to BIA-ALCL occurrence. A study by Urbaniak *et al.* [13] suggests that microbiome from the female mammary gland differs among country regions; and Shively *et al.* [14] suggested diverse diets directly contribute to the

variation. However, it is still unclear why a higher incidence rate of BIA-ALCL occurs among the textured breast implants than the smooth implants.

The total surface area of a textured breast implant is higher than that of a smooth implant of the same size. Loch-Wilkinson *et al.* [6] demonstrated that higher surface area is associated with more bacterial contamination and it can lead to chronic antigen stimulation resulting in the onset of BIA-ALCL. Department of Health (Therapeutic Goods Administration) of the Australian Government recently reported the specifications (surface roughness, surface area, surface area ratio (3D/2D), etc.) of commercial textured breast implant devices [15]. Even though there is a clear correlation between surface area and BIA-ALCL incidence rate, not all cases follow this rule. Moreover, there are different types of textures due to the fabrication methods used, which can contribute to the complexity of surface topography and thus bacterial response. Even though a causative mechanism of BIA-ALCL has not been established yet, regulatory agencies are considering to classify textured breast implants based on their surface area [16–19], rather than the 3D topography. Thus, it is important to understand how surface topography affects bacterial adhesion.

In this study, we created a library of well-defined recessive textures by varying feature sizes and distances between features, including similar feature sizes to the commercial breast implant which has the highest BIA-ALCL prevalence (salt-loss method). Through a high throughput screening, we identified the features that promote bacterial adhesion and verified the findings using confocal microscopy.

3.3 Materials and Methods

3.3.1 PDMS surface fabrication

To obtain polydimethylsiloxane (PDMS) surfaces with topographic patterns of interest, a Si wafer with complementary patterns was fabricated at Cornell NanoScale Science & Facility (CNF) using photolithography as shown in Figure 3.1. Briefly, the pattern features with different sizes of side length and spacing were designed by L-edit computer-aided design (CAD) software. To investigate the effects of feature size on bacterial adhesion, we varied the side length from 2 µm to 300 µm and the distance between features from 2 µm to 100 µm. All patterns had a depth of 10 µm. A positive photoresist (PR) layer on a Cr deposited quartz mask was exposed by UV using DWL 2000 Heidelberg mask writer (Heidelberg Instruments Mikrotechnik GmbH, Heidelberg, Germany) based on the CAD file followed by the development of PR and Cr layers. The rest of the PR layer was stripped by N-Methyl-2-pyrrolidone (NMP) and tetramethylammonium hydroxide (TMAH) based cleaning solution for 30 min in a 60°C hot bath.

To create features on a silicon (Si) wafer, a 30-50 nm P20 adhesion layer, and a 1.8-2.5 µm positive PR layer (S1813) were deposited first using a spin coater at 2000 rpm for 60 sec. An ABM contact aligner (1:1 ratio photolithography; ABM USA Inc., San Jose, CA, USA) was used to draw features on the Si wafer by exposing UV light through the Cr mask followed by a development process using the TMAH based cleaning solution. The developed Si wafer was then etched to produce 10 µm depth by deep reactive ion Si etcher (DRIE; Plasma-Therm LLC, St. Petersburg, FL, USA). A YES Asher (Yield Engineering Systems Inc., Livermore, CA, USA) stripper was used to strip the remained PR from the etched Si wafer. To ease the peeling of the PDMS layer from the Si wafer, a surface of the etched Si wafer was made hydrophobic by

molecular vapor deposition (MVD; Applied Microstructures, San Jose, CA, USA) of fluorooctyltrichlorosilane (FOTS).

The patterned Si wafer was then used as a master to fabricate PDMS with designed features. A mixture of 10:1 weight ratio of Dow Sylgard 184 base and curing agent (The Dow Chemical Company, Midland, MI, USA) was mixed and vacuumed for 1 h to remove air bubbles produced during the chemical reaction of base and curing agent. The vacuumed mixture was then poured on the Si master, spin-coated for 1 min at 50 rpm, and vacuumed again for 1 h to remove all trapped air bubbles inside the features. After 1 h of vacuum, the sample was cured at 60°C for 2 h and cooled down at room temperature for 1 h.
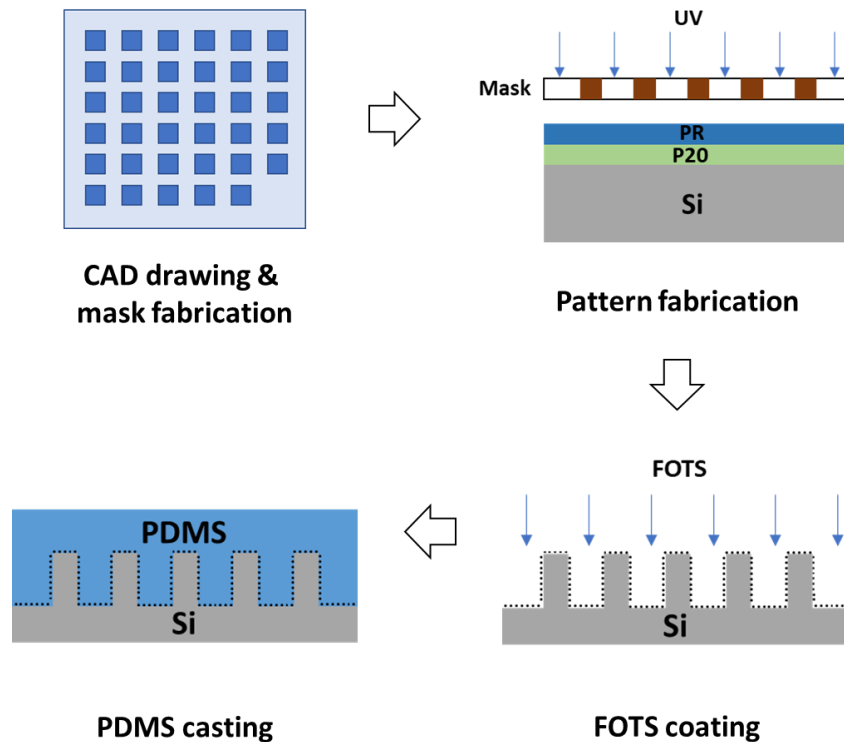
Figure 3.1. Schematic of patterned PDMS fabrication. A combination of features was drawn by CAD software, L-edit, and a quartz mask was fabricated based on the design. P20 (an adhesion layer) and a photoresist (PR) layer were deposited by a spin coater and it was exposed and etched through a 1:1

53

contact photolithography and an etcher, respectively, to create features. A fluorooctyltrichlorosilane (FOTS) layer was then deposited to modify the surface into hydrophobic. Lastly, polydimethylsiloxane (PDMS) was cast using the patterned Si master as a mold.

3.3.2 Bacterial strains and growth medium

E. coli RP437/pRSH103 [20] was grown in tryptic soy broth (TSB) (Thermo Fisher Scientific, Waltham, MA, USA) or lysogeny broth (LB) [21] supplemented with 30 µg/mL of tetracycline (Sigma Aldrich, St. Louis, MO, USA).

3.3.3 Biomass

To quantify the biomass on PDMS surfaces in a high-throughput manner, each PDMS sample was punched with a 6 mm Biopsy puncher (Integra Lifesciences, Plainsboro Township, NJ, USA) and transferred into a well of a 96 well plate (Santa Cruz Biotechnology, Inc., Dallas, TX, USA). The PDMS sample was attached to the bottom of the well using three additional droplets of PDMS mixture which cover the rest of the well surface and make the PDMS sample stick to the well and cured at 60°C for 2 h. The loaded PDMS surfaces were then sterilized by UV for 1 h prior to inoculation.

E. coli RP437/pRSH103 was used to inoculate biofilm cultures in each well with 100 µL growth medium covering the PDMS sample. The culture was inoculated with a starting optical density (OD) at 600 nm (OD_{600}) of 0.1. To remove trapped air bubbles from the PDMS surface, 100 µL sterile phosphate-buffered saline (PBS) was added in each well and vacuumed for 30 min prior to inoculation. The cultures were incubated for 4 h at 37°C with/without shaking at 200 rpm.

After incubation, the samples were washed three times with PBS using a plate washer (BioTek 50TS microplate washer, BioTek, Winooski, VT, USA). At the excitation wavelength of 558 nm and an emission wavelength of 583 nm, the red fluorescent protein (RFP) signal intensity was measured using a plate reader (TECAN infinite M1000, Tecan, Mannedorf, Switzerland) to quantify biomass.

3.3.4 Surface analysis

PDMS surfaces were also analyzed using scanning electron microscopy (SEM, JEOL Ltd., Tokyo, Japan). The PDMS samples were coated with gold (Au) using sputter (Denton Vacuum LLC, Moorestown, NJ, USA).

To visualize the biofilms in 3D, biofilms were analyzed using confocal microscopy (Leica SP8, Leica Camera AG, Wetzlar, Germany) and fluorescent microscopy (Axio Imager M1, Carl Zeiss Inc., Berlin, Germany). To quantify the biomass, Z-stack images with 3D information were obtained by the fluorescent microscopy followed by quantification using the software COMSTAT [22]. The experiments were conducted with three biological replicates with 5 random images analyzed from each sample.

3.3.5 Statistics

SAS 9.1.3, Windows version (SAS, Cary, NC, USA) was used for all statistical analyses. Results with $p<0.05$ were considered as statistically significant.

3.4 Results

3.4.1 Design of topographic features

To systematically characterize the effects of surface topography on bacterial attachment, we varied the side length of 10 µm-deep recessive square patterns as 2, 5, 10, 50, 100, 200, and 300 µm, and distance between squares as 2, 5, 10, 50, and 100 µm. In addition to the fundamental study, these features also cover those of commercial textured breast implants [15]. The surface area ratios included in this study are summarized in Table 3.1, with surface area ratios (total surface vs. the projected area in the x-y plane) varying from 1 (flat control) to 4.70.

Table 3.1. Surface area and surface area ratio (3D/2D) of both PDMS samples and commercial textured breast implants.

PDMS samples		Distance (µm)									
		2		5		10		50		100	
		Surface area (mm²)	Surface ratio (3D/2D)	Surface area (mm²)	Surface ratio (3D/2D)	Surface area (mm²)	Surface ratio (3D/2D)	Surface area (mm²)	Surface ratio (3D/2D)	Surface area (mm²)	Surface ratio (3D/2D)
Side (µm)	2	90.04	3.18	52.02	1.84	36.47	1.29	28.67	1.01	28.43	1.01
	5	132.99	4.70	73.23	2.59	51.39	1.82	29.66	1.05	28.79	1.02
	10	84.96	3.00	73.41	2.60	50.05	1.77	30.94	1.09	29.02	1.03
	50	41.16	1.46	42.34	1.50	42.45	1.50	34.31	1.21	31.34	1.11
	100	42.25	1.49	36.54	1.29	36.45	1.29	34.32	1.21	31.23	1.10
	200	34.20	1.21	34.61	1.22	34.67	1.23	31.66	1.12	31.53	1.11
	300	31.11	1.10	31.40	1.11	31.50	1.11	31.53	1.12	29.92	1.06
Commercial textured breast implants		Allergan Smooth		Mentor Siltex		Allergan Biocell		Nagor Nagotex		Silimed PU	
		Surface area (mm²)	Surface ratio (3D/2D)	Surface area (mm²)	Surface ratio (3D/2D)	Surface area (mm²)	Surface ratio (3D/2D)	Surface area (mm²)	Surface ratio (3D/2D)	Surface area (mm²)	Surface ratio (3D/2D)
		28.8 ~ 36	~ 1	36 ~ 72	~ 2.2	72 ~ 108	~ 3.6	> 108	~ 3.3	> 108	~ 8.6

3.4.2 Biomass

To study the effects of topography on bacterial attachment, we tested the 4 h attachment of *E. coli* RP437/pRSH103 expressing constitutive red fluorescence. To characterize a large number of surface features with sufficient repeats, we developed a new high-throughput assay using a plate washer and a plate reader with PDMS plugs with topographic features fixed in the wells of 96-well plates. The operating condition of the plate reader was optimized by adjusting the flow rate

to effectively remove planktonic cells but not to disturb the attached cells. As presented in Figure 3.2, a signal intensity varied in terms of the 'position height' of the plate reader and the dispense flow rate of the plate washer during a washing process. The 'position height' is the height of the focal point for the plate reader that can move from the bottom to the top of 96 wells relatively. To get the reliable data of the signal intensity, it is important to get the optimum focal point on the sample surface to obtain the highest signal intensity. As shown in Figure 3.2, the signal intensity at position 4,000 µm showed the highest signal intensity among the entire dispense flow rate. For the plate washer, it is essential to have the consistent and reliable ability of the washing process and the dispense flow rate of PBS solution from the manifold can be a major factor to affect results. The dispense flow rate of the manifold can vary from 200 µL/sec to 800 µL/sec. From the data of Figure 3.2, the highest signal intensity with a narrow standard deviation range was observed at the dispense flow rate of 800 µL/sec with a position height of 4,000 µm. Through the same principles, other conditions of the plate washer such as manifold position height during aspiration and dispense process were determined at 8.89 mm and 13.97 mm, respectively.
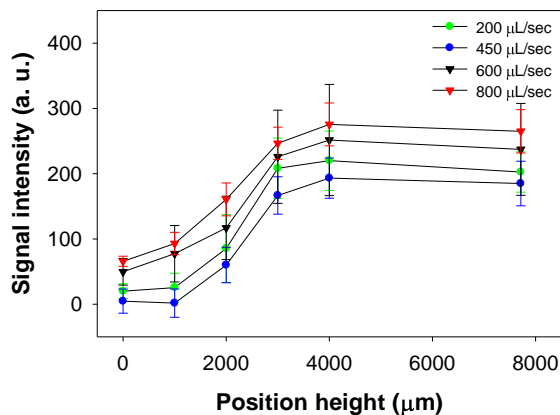
Figure 3.2. Red fluorescent signal intensity was analyzed by a plate reader with varying focal position height from 0 μm (bottom) to 8000 μm (top) of the well. The dispense flow rate of PBS solution varied from 200 μL/sec to 800 μL/sec.

The topographic features were tested under both the static condition (no agitation) and with the flow (rotation at 200 rpm). The features that mimic two commercial textured breast implants are marked as A (green square) and B (blue triangle) in Figure 3.3a. Most features showed similar biomass as the flat control (red circle). However, there were five conditions, three outliers from the PDMS library and two of the commercial textured breast implants, that showed up to 2.1 times higher biomass than the flat control ($p<0.05$, one-way ANOVA adjusted by Turkey test). The three outliers from the PDMS library were S5 D2, S10 D2, and S10 D5 [S: feature side length (μm), D: distance between features (μm)]. However, no significant difference among these features was observed under flow ($p>0.05$, one-way ANOVA adjusted by Turkey test; Figure 3.3b).

To corroborate the results of the biomass under the static condition for *E. coli* RP437/pRSH103 attachment, the two surfaces with the highest biomass(1: S10 D5 and 2: S10 D2) and the flat control were imaged using confocal microscopy as shown in Figure 3.3c. The images are consistent with the plate reader results, showing more cells attached to the S10 D5 and S10 D2 samples than the flat control. In addition, more cells were found to attach at the edges/corners of the recessive features than the horizontal surface of these patterns. We then quantified the biomass of cell attachment inside of features and compared them with the flat control (Figure 3.3d). The S10 D5 and S10 D2 patterns showed biomass of 0.73 ± 0.05 μm^3/μm^2 and 0.50 ± 0.02 μm^3/μm^2, respectively, which are 10.2 and 7.0 times higher than the flat control (0.07 ± 0.01 μm^3/μm^2), respectively ($p<0.001$, t-test).

(a)
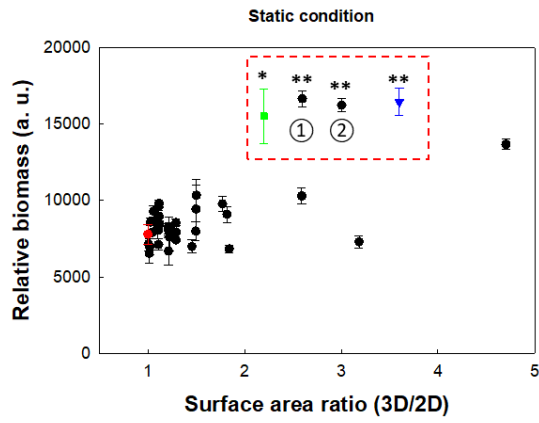
(b)
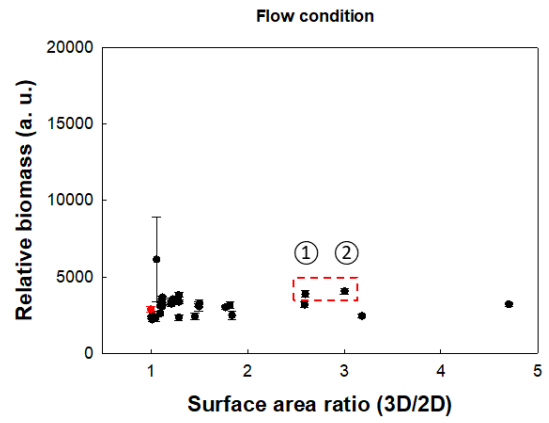
(c)

Flat   **① S10 D5**   **② S10 D2**
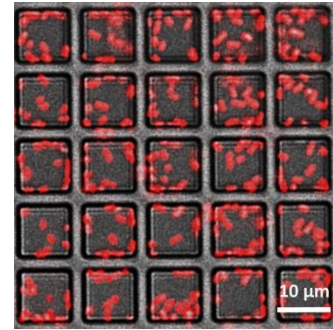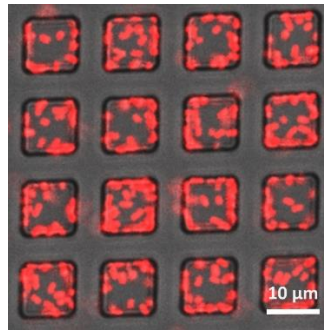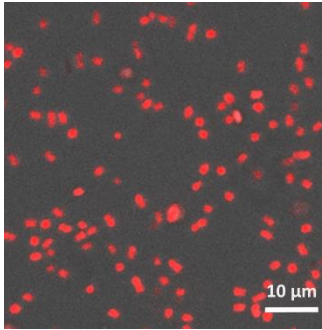
(d)
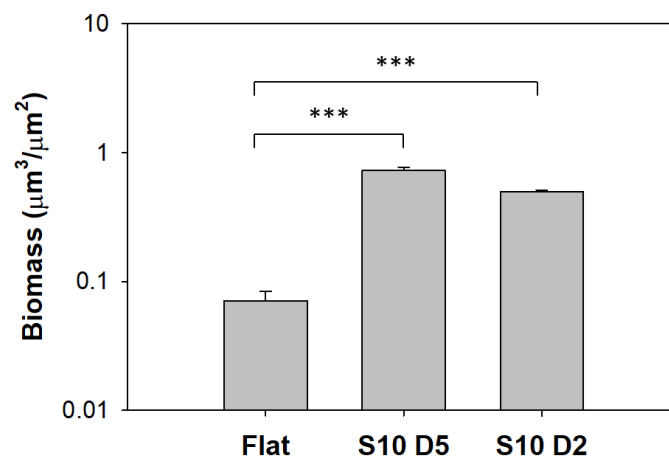
Figure 3.3. Relative biomass of *E. coli* RP437/pRSH103 after 4 h attachment on the PDMS surfaces under (a) static condition (no agitation) and (b) flow condition (200 rpm). (Red circle: flat control. Green square: commercial textured breast implant A. Blue triangle: commercial textured breast implant B. ①:S10 D5. ②:S10 D2) * p<0.05 and ** p<0.01. Representative fluorescent confocal microscopic images of (c) flat, S10 D5, and S10 D2 are shown. S: a dimension of feature side (µm), D: a dimension of the distance between features (µm). Scale bar = 10 µm (d) Biomass of *E. coli* cells on flat PDMS and in the wells of S10 D5 and S10 D2 patterns. ***p<0.001.

3.4.3 4 h Tracking of E. coli RP437/pRSH103 during attachment

To understand if there is a preferred area for cells to attach in the topographic features, we followed cell adhesion on S10 D5 surfaces over time up to 4 h. These surfaces have recessive features with 10 µm side length and 5 µm distance in between. A number of the attached cells normalized by the surface area was used to calculate the ratio of horizontal surface area to edge area. Figure 3.4a shows the areas categorized as an edge (red) and the horizontal a surface area (blue) of the pattern, along with representative microscopic images focused on the top and bottom as a biofilm. Representative confocal microscopic images during 4 h attachment are shown in Figure 3.5. The ratio was found to increase over time (Figure 3.4b), which refers that the cells prefer to adhere more at the edges/corners than face area as the attachment time increases or one or two generations of cell growth from the attached cells.

(a)

Top focused

Bottom focused
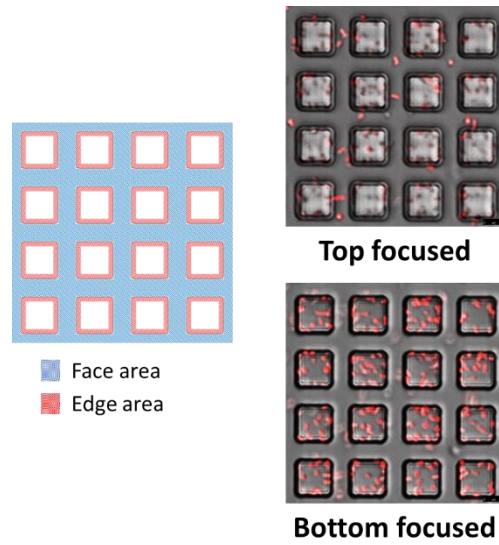
Face area
Edge area

(b)
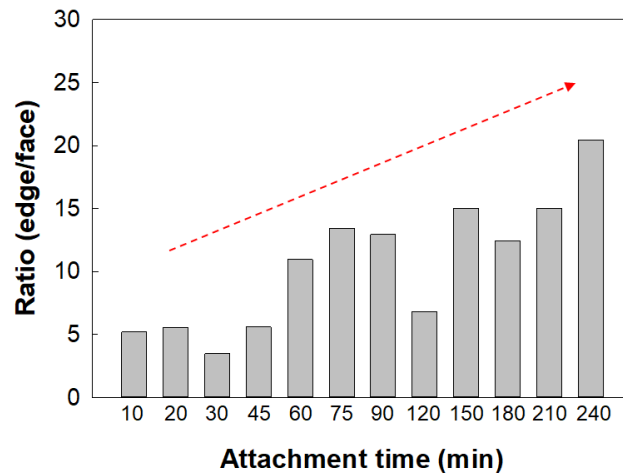
Figure 3.4. Schematic of (a) edge area (36 µm^2, red) and face area (125 µm^2, blue) for calculating a ratio of the attached cell numbers on the same features with different focal points. Top focused and bottom focused fluorescent confocal microscopic images show the attached cells on the focal area of face and edge, respectively. (b) A ratio of the attached cell numbers on the edge area to the face area (*E. coli* RP437/pRSH103) in terms of the attachment time normalized by surface area.
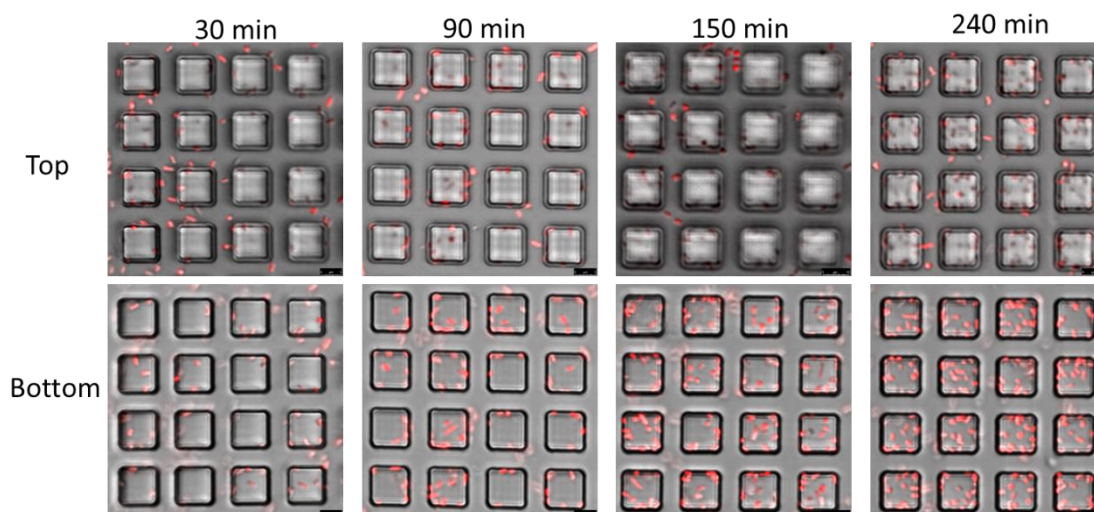
Figure 3.5. Representative confocal microscopic images of patterns (top and bottom focal point) with the attached cells in terms of attachment time; 30, 90, 150, and 240 min. Scale bar = 5 µm.

To avoid the effects of gravity, we repeated the 4 h attachment on 'facing down' surfaces of the same PDMS library. Figure 3.6 showed that 5.3 times and 5.0 times higher numbers of cells were attached to S10 D5 and S10 D2 surfaces respectively, compared to the flat control. The Video 3.1 showed where the individual cells adhered on the feature and demonstrated that the cells preferred to attach on the edges rather than the face area. We could also see some of the attached cells started to multiply from the interfacial junctions. The video provided further evidence that *E. coli* RP437/pRSH103 adheres more on certain features (S10 D5, S10 D2, and S5 D2) than the flat control irrespective of the gravity.
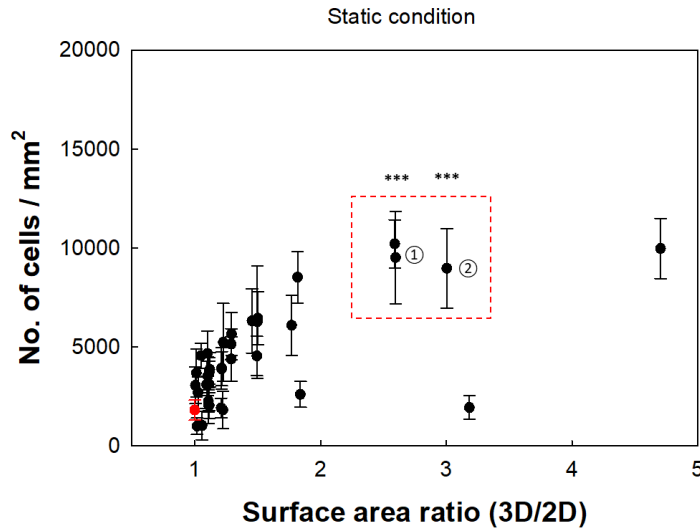
Figure 3.6. The number of attached *E. coli* RP437/pRSH103 cells on 'facing down' patterned PDMS

surfaces after 4 h attachment under static (no agitation) condition. (Red circle: flat control. ①:S10 D5.

②:S10 D2) *** $p<0.001$.
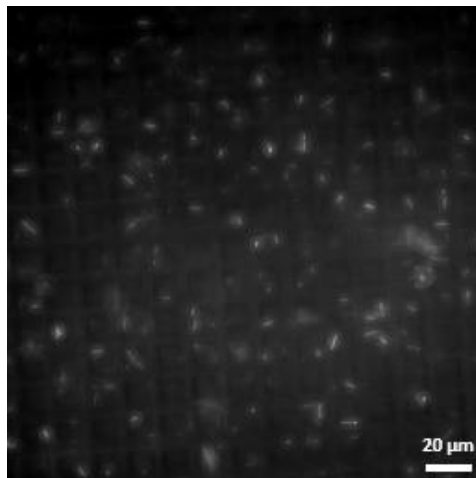
Video 3.1. Snapshot from a video of tracking for *E. coli* RP437/pRSH103 4 h attachment on S10 D5

'facing down' surface in a LB media. Scale bar = 20 μm.

3.4.4 24 h biofilm growth of E. coli RP437/pRSH103

To further understand the effects of topography on biofilm growth, we tested a longer time

point than the initial 4 h attachment. From the data of biofilm growth for 24 h, Figure 3.7, about

5 times more biomass was observed than the biomass from 4 h attachment. The biomass of

biofilm on most of PDMS feature samples, however, showed lower biomass than the flat control

(some are significant, and others are not). Only one condition (S300 D50) plus one commercial

breast implant (blue triangle) showed a significant higher biomass (1.49 times and 2.11 times,

respectively) than flat control ($p<0.05$, one-way ANOVA adjusted by Turkey test).
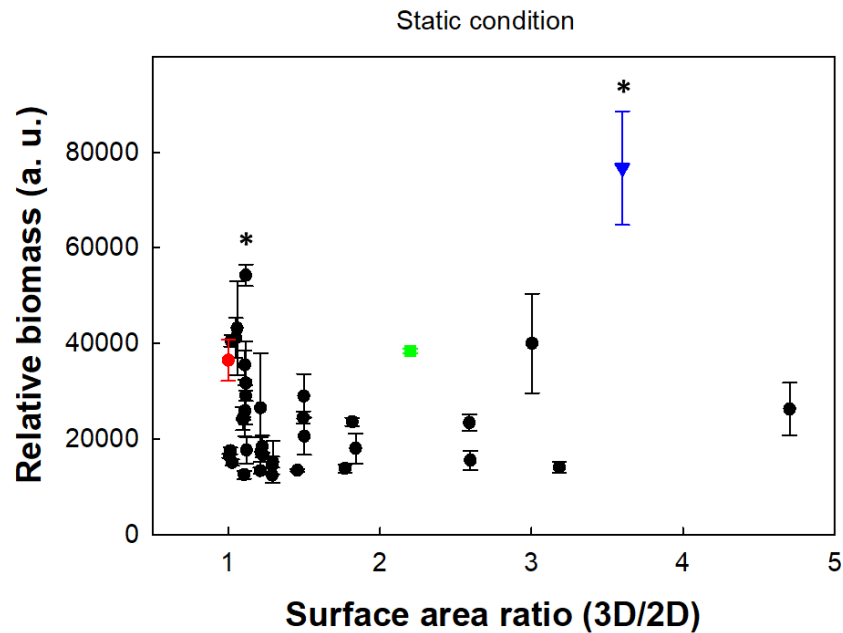
Figure 3.7. Relative biomass of *E. coli* RP437/pRSH103 after 24 h biofilm growth on patterned PDMS

surfaces under static condition (Red circle: flat control. Green square: commercial textured breast

implant A. Blue triangle: commercial textured breast implant B.) * *p<0.05*.

3.5 Discussion

The concern of breast implant associated-anaplastic large cell lymphoma (BIA-ALCL) has been on the rise due to the increasing cases of BIA-ALCL especially from textured breast implants [1]. Recent studies have demonstrated that chronic inflammation resulted from microbial colonization may mediate hyperplasia of T cells and the development of BIA-ALCL [3,4,6]. Biofilm caused increased T-cell response and the number of T and B cells was found proportional to the number of bacteria from the capsules of patients who have removed the breast implants due to Baker grade IV contracture [3]. Gram-negative *Ralstonia* spp. was found to be dominant on the breast implants associated with BIA-ALCL; while more *Staphylococcus* spp. was associated with non-tumor capsule specimens [4]. Loch-Wilkinson *et al.* [6] claimed that the surface area of textured breast implants is positively correlated with the risk of BIA-ALCL. However, the surface area does not accurately describe the 3D topography of a surface and further study is needed to understand the real causative factor(s).

To understand the effects of surface topography on bacterial colonization, we developed a high throughput method to investigate initial microbial attachment and biofilm growth of *E. coli* RP437/pRSH103, a Gram-negative strain, on PDMS surfaces with systemically varied recessive patterns. The data provide evidence that bacterial colonization is not proportional to the surface area but decided by the 3D topography. The results also reveal the features that are more prone to bacterial attachment. For example, the cells prefer to attach at two or three interfacial junctions. To verify the effect of interfacial junctions, we think it is a good starting point to plot the graph in terms of surface area ratio (3D/2D). The surface area ratio affects more on 3D topography properties especially interfacial junctions and it covers 3D places to count the areas of overhangs, caves, and other embedded areas that 2D surface area cannot include. However, even

the surface area ratio could not explain all the results that we obtained from 4 h cell attachment and 24 h biofilm growth test. Even though certain features such as S10 D2, S10 D5, and S5 D5 showed more cell attachment from 4 h attachment than the flat control, not a consistent result has demonstrated from 24 h biofilm growth. This refers that the physiology of bacterial cells as well as the virulence factor which affects cell attachment may change between a short and long period. This study is still ongoing and an investigation on physiological changes of the attached cells in terms of adhesion time will be needed to understand the mechanism of biomass on the implantable medical devices.

Based on the literature [6], Allergan Biocell (58.7%) implants have the highest percentage of getting BIA-ALCL among six commercial textured breast implants. The Allergan Biocell textured breast implant is manufactured through the 'Salt-loss' method which creates negative square-like topography. Based on the PDMS patterns with the side length of 2 µm to 300 µm and the distance between features from 2 µm to 100 µm, the majority of textures of Biocell breast implant, maximum 300 µm side and 100 µm distance between squares, were covered. By comparing the surface topography of Biocell with other commercial breast implants, we can see that the 'Salt-loss' process produces more interfacial junctions than other methods such as 'Imprinting stamping', 'polyurethane (PU) foam coating', and 'vulcanization' method. The features tested in this study do not include the "bridge" structures. Further studies using 3D printing can help understand the additional risk associated with those structures.

3.6 Conclusion

   In summary, we developed a high-throughput method to study bacterial attachment on PDMS

surfaces with recessive patterns that have a systemically varied size and spacing. By examining

bacterial adhesion on these surfaces, we found that *E. coli,* a Gram-negative strain, prefer on

certain features (S10 D5, S10 D2, and S5 D2) and the features that mimic the commercial breast

implants associated with a high prevalence of BIA-ALCL. Besides the size of patterns, *E. coli*

exhibits a preference to adhere more to the interfacial junction area rather than the open flat area.

The area of interfacial junctions may also help microorganisms to escape the attack by the host

immune cells. Overall, these results indicate that surface area is not the deciding factor of BIA-

ALCL and the 3D topography is important. Further study is needed to elucidate the causative

factors of BIA-ALCL.

3.7 Acknowledgements

3.8 References

[1]   U.S. Food and Drug Administration, Medical Device Reports of Breast Implant-
        Associated Anaplastic Large Cell Lymphoma, (n.d.). https://www.fda.gov/medical-
        devices/breast-implants/medical-device-reports-breast-implant-associated-anaplastic-
        large-cell-lymphoma.

[2]   U.S. Food and Drug Administration, Allergan Recalls Natrelle Biocell Textured Breast
        Implants Due to Risk of BIA-ALCL Cancer, (n.d.). https://www.fda.gov/medical-
        devices/medical-device-recalls/allergan-recalls-natrelle-biocell-textured-breast-implants-
        due-risk-bia-alcl-cancer.

[3]   H. Hu, A. Jacombs, K. Vickery, S.L. Merten, D.G. Pennington, A.K. Deva, Chronic
        Biofilm Infection in Breast Implants Is Associated with an Increased T-Cell Lymphocytic
        Infiltrate, Plast. Reconstr. Surg. 135 (2015) 319–329.
        https://doi.org/10.1097/PRS.0000000000000886.

[4]   H. Hu, K. Johani, A. Almatroudi, K. Vickery, B. Van Natta, M.E. Kadin, G. Brody, M.
        Clemens, C.Y. Cheah, S. Lade, P.A. Joshi, H.M. Prince, A.K. Deva, Bacterial Biofilm
        Infection Detected in Breast Implant-Associated Anaplastic Large-Cell Lymphoma, Plast.
        Reconstr. Surg. 137 (2016) 1659–1669. https://doi.org/10.1097/PRS.0000000000002010.

[5]   A. Jacombs, S. Tahir, H. Hu, A.K. Deva, A. Almatroudi, W.L.F. Wessels, D.A. Bradshaw,
        K. Vickery, In vitro and in vivo investigation of the influence of implant surface on the
        formation of bacterial biofilm in mammary implants, Plast. Reconstr. Surg. 133 (2014)
        471–480. https://doi.org/10.1097/PRS.0000000000000020.

[6]   A. Loch-Wilkinson, K.J. Beath, R.J.W. Knight, W.L.F. Wessels, M. Magnusson, T.

Papadopoulos, T. Connell, J. Lofts, M. Locke, I. Hopper, R. Cooter, K. Vickery, P.A. Joshi, H.M. Prince, A.K. Deva, Breast implant-associated anaplastic large cell lymphoma in Australia and New Zealand: High-surface-area textured implants are associated with increased risk, Plast. Reconstr. Surg. 140 (2017) 645–654. https://doi.org/10.1097/PRS.0000000000003654.

[7]   J.N. Walker, B.M. Hanson, C.L. Pinkner, S.R. Simar, J.S. Pinkner, R. Parikh, M.W. Clemens, S.J. Hultgren, T.M. Myckatyn, Insights into the Microbiome of Breast Implants and Periprosthetic Tissue in Breast Implant-Associated Anaplastic Large Cell Lymphoma, Sci. Rep. 9 (2019) 1–12. https://doi.org/10.1038/s41598-019-46535-8.

[8]   M. Mempin, H. Hu, D. Chowdhury, A. Deva, K. Vickery, The A, B and C's of silicone breast implants: Anaplastic large cell lymphoma, biofilm and capsular contracture, Materials (Basel). 11 (2018). https://doi.org/10.3390/ma11122393.

[9]   M. Magnusson, K. Beath, R. Cooter, M. Locke, H.M. Prince, E. Elder, A.K. Deva, The Epidemiology of Breast Implant-Associated Anaplastic Large Cell Lymphoma in Australia and New Zealand Confirms the Highest Risk for Grade 4 Surface Breast Implants, Plast. Reconstr. Surg. 143 (2019) 1285–1292. https://doi.org/10.1097/PRS.0000000000005500.

[10]   G. Cappellano, C. Ploner, S. Lobenwein, S. Sopper, P. Hoertnagl, C. Mayerl, N. Wick, G. Pierer, G. Wick, D. Wolfram, Immunophenotypic characterization of human T cells after in vitro exposure to different silicone breast implant surfaces, PLoS One. 13 (2018) 1–14. https://doi.org/10.1371/journal.pone.0192108.

[11]   S. Hoda, R. Rao, R.S. Hoda, Breast Implant-Associated Anaplastic Large Cell

Lymphoma, Int. J. Surg. Pathol. 23 (2015) 209–210.
https://doi.org/10.1177/1066896915576406.

[12]   N.J. Hallab, L. Samelko, D. Hammond, The Inflammatory Effects of Breast Implant
       Particulate Shedding: Comparison with Orthopedic Implants, Aesthetic Surg. J. 39 (2019)
       S36–S48. https://doi.org/10.1093/asj/sjy335.

[13]   C. Urbaniak, J. Cummins, M. Brackstone, J.M. Macklaim, G.B. Gloor, C.K. Baban, L.
       Scott, D.M. O'Hanlon, J.P. Burton, K.P. Francis, M. Tangney, G. Reida, Microbiota of
       human breast tissue, Appl. Environ. Microbiol. 80 (2014) 3007–3014.
       https://doi.org/10.1128/AEM.00242-14.

[14]   C.A. Shively, T.C. Register, S.E. Appt, T.B. Clarkson, B. Uberseder, K.Y.J. Clear, A.S.
       Wilson, A. Chiba, J.A. Tooze, K.L. Cook, Consumption of Mediterranean versus Western
       Diet Leads to Distinct Mammary Gland Microbiome Populations, Cell Rep. 25 (2018) 47-
       56.e3. https://doi.org/10.1016/j.celrep.2018.08.078.

[15]   Australian Government (Department of Health), Biomaterials & Engineering Laboratory
       Report Project : Surface Topography Device : Non-active mammary implants, 2019.

[16]   U.S. Food and Drug Administration, Statement from Binita Ashar, M.D., of the FDA's
       Center for Devices and Radiological Health on agency's commitment to studying breast
       implant safety, (2018). https://www.fda.gov/news-events/press-announcements/statement-
       binita-ashar-md-fdas-center-devices-and-radiological-health-agencys-commitment-
       studying.

[17]   World Health Organization, Silicone implants, (2012).
       https://www.who.int/csr/don/2012_01_17/en/.

[18]   International Organization for Standardization, ISO 14602 - Non-active surgical implants

        - Implants for osteosynthesis - Particular requirements, (2018).

        https://www.iso.org/obp/ui/#iso:std:iso:14607:ed-3:v2:en.

[19]   International Organization for Standardization, ISO 10993-1:2018(en) Biological

        evaluation of medical devices — Part 1: Evaluation and testing within a risk management

        process, (2018). https://www.iso.org/obp/ui/#iso:std:iso:10993:-1:ed-5:v2:en.

[20]   Y. Han, S. Hou, K.A. Simon, D. Ren, Y.Y. Luk, Identifying the important structural

        elements of brominated furanones for inhibiting biofilm formation by Escherichia coli,

        Bioorganic Med. Chem. Lett. 18 (2008) 1006–1010.

        https://doi.org/10.1016/j.bmcl.2007.12.032.

[21]   G. Bertani, Studies on lysogenesis. I. The mode of phage liberation by lysogenic

        Escherichia coli., J. Bacteriol. 62 (1951) 293–300. https://doi.org/citeulike-article-

        id:149214.

[22]   A. Heydorn, A. Heydorn, A.T. Nielsen, A.T. Nielsen, M. Hentzer, M. Hentzer,

        Quantication of biofilm structures by the novel computer program, Image Process. 146

        (2000) 2395–2407. https://doi.org/10.1099/00221287-146-10-2395.

Chapter 4

Effects of one-way dynamic surface topography

on *Pseudomonas aeruginosa* biofilm removal

4.1 Abstract

Bacterial biofilms are a major cause of chronic infections and biofouling; however, effective removal of established biofilms remains challenging. Here we report a new strategy for biofilm control using biocompatible shape memory polymers with defined surface topography. These surfaces can both prevent bacterial adhesion and remove established biofilms upon rapid shape change with a moderate increase of temperature, thereby offering more prolonged antifouling properties. We demonstrate that this strategy can achieve a total reduction of *Pseudomonas aeruginosa* biofilms by 99.9% compared to the static flat control.

4.2 Introduction

A large number of studies on topographic effects have been conducted to investigate how micron and nanoscale topographies affect cell adhesion and biofilm formation. Some nanoscale topographies have been demonstrated to have bactericidal effects through direct damage to bacterial membranes [1]. In contrast, micron-scale topographies do not have bactericidal effects but may inhibit bacterial adhesion through specific effects on bacteria-material interactions [2]. Topographic features associated with a bacterial infection on medical devices were also studied and it can be organized based on their locations of use such as breast implants [3], bone implants [4–6], catheters [7], and oral implants [8–10]. Among these, orthopedics devices and dental implants have been explored more than the other devices. It will be helpful to investigate the effects of surface topography of soft materials such as breast implants and catheters.

As mentioned above, lots of researches about surface topography have been stated, and recommended topographic designs to prevent bacterial adhesion were also suggested. However, most of the topography studies on bacterial attachment were investigated based on static features and suggested most strategies for biofilm control lost their abilities after mature biofilms are fully formed on the surfaces. In other words, it is a lack of studies for the effects of dynamic topography features on bacterial adhesion and biofilm control strategy on post-mature biofilms.

To remove mature biofilms from the surface, we developed a novel strategy of dynamic topography using shape memory polymer (SMP). Based on the similar polymeric materials used for urinary catheter devices, we used *tert*-butyl acrylate-based polymers and studied the effects of dynamic change in topography on *Pseudomonas aeruginosa* biofilm removal.

4.3 Materials and Methods

4.3.1 Bacterial strains and growth medium

Pseudomonas aeruginosa PAO1 [11] was routinely grown in Lysogeny Broth (LB) [12] consisting of 10 g/L NaCl, 5 g/L yeast extract, and 10 g/L tryptone at 37°C with shaking at 200 rpm.

4.3.2 SMP substrate preparation

To enable the change in surface topography and biofilm removal, we prepared a glassy SMP using t-Butyl acrylate (tBA), poly (ethylene glycol)$_n$ dimethacrylate (PEGDMA) with a molecular weight of $M_n=750$, and photoinitiator 2,2-dimethoxy-2-phenylacetophenone (DMPA) (Sigma Aldrich, St. Louis, MO, USA), as described previously [13]. The tBA-co-PEGDMA networks were synthesized by free radical photo-polymerization using a 0.4% (wt%) photoinitiator (DMPA). The weight ratio between the linear chain building monomer (tBA) and di-functional crosslinking monomer (PEGDA) was set as 9 to 1 to synthesize polymer networks with a transition temperature slightly higher than body temperature (37°C) [13].

4.3.3 Preparation of SMP surfaces for biofilm formation

To prepare programmable SMP substrates that are flat as the permanent shape, the mixture was injected between two glass slides with a 1 mm thick PDMS spacer using a syringe (Figure 4.1a). The glass slides were pretreated with Rain-X to prevent the adhesion with cured SMPs [14]. Pre polymerization was conducted under 365 nm UV irradiation for 10 min, followed by a thermal post-cure for 1 h at 90°C to maximize the conversion of monomers [13]. The SMPs were stored at room temperature until further processing. To prepare programmable SMP substrates with recessive hexagonal patterns as the permanent topography, PDMS surfaces with 10 µm tall

systematically designed hexagonal patterns with side length (L) of 5, 10, 15, 20, 30, 40, or 50 µm and inter-pattern distance (D) of 2, 5, 10, 15, or 20 µm were used as molds to recreate the recessive hexagonal patterns on the SMP surface during casting, by injecting the mixture between a PDMS surface and a glass slide as described above (Figure 4.1b). These PDMS surfaces were obtained using silicon wafers with complementary patterns etched via photolithography as described previously [15,16].

To ensure uniform deformation during shape fixing (shape memory programming), both flat and topographically patterned substrates were cut into dog bone-shaped specimens, which were incubated at 50°C for 5 min and then gradually stretched using a manual stretcher to 1.5 times of the original length. After an SMP substrate was deformed, the temporary shape was fixed via approximately 5 min cooling at room temperature. To trigger the transition to the permanent shape, these SMP substrates with their temporary shape were incubated in pre-warmed 0.85% NaCl for 10 min at 40°C. To produce a static flat control substrate (that do not undergo shape change when heated), flat SMP substrates after 1 h post-cure at 90°C were cut into small pieces (2 mm in length and 1 mm in width) for biofilm formation. These surfaces were not stretched and fixed in a temporary shape, so no shape change would occur at 40 ℃, serving as a control group.

(a)
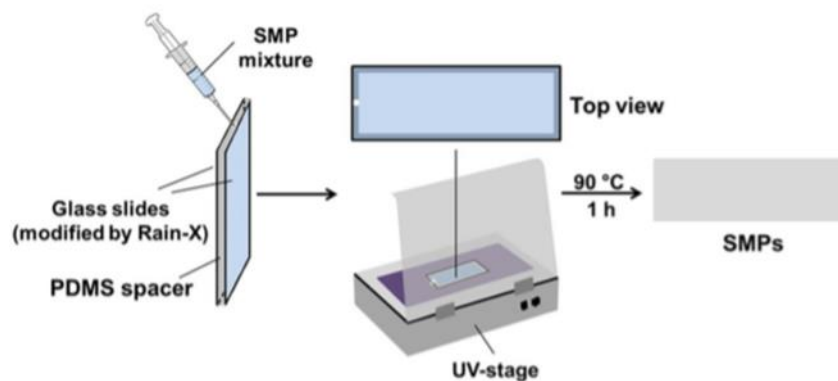
(b)
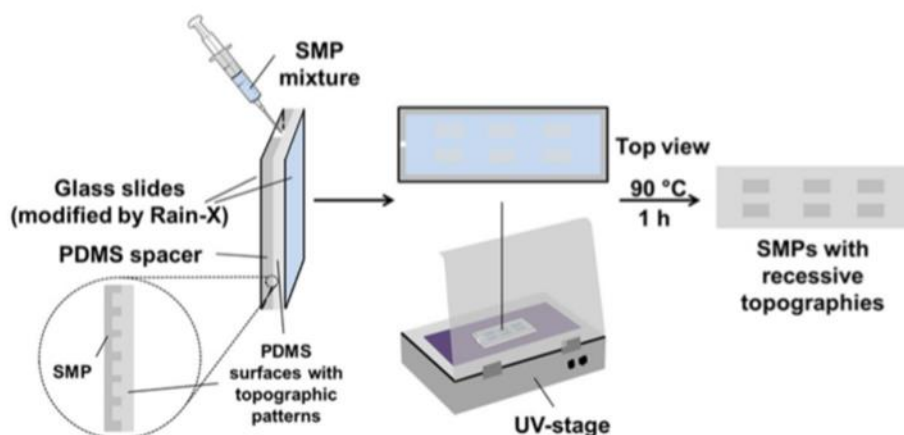
Figure 4.1. Schematic illustration of the substrate preparation process. (a) Programmable SMP

substrates that are flat as the permanent shape. (b) Programmable SMP substrates with hexagonal

patterns as the permanent topography.

4.3.4 Biofilm formation

Flat control substrates and both flat and topographically patterned programmed substrates were

cleaned with deionized water, wiped to dry, and then sterilized in sterile Petri-dishes by 1 h UV

exposure per side. Overnight cultures of *P. aeruginosa* PAO1 was used to inoculate fresh LB

solution to an OD_{600} of 0.05.

The biofilm cultures were incubated at room temperature for 48 h. Then, static flat controls and programmed SMPs in their temporary shape (flat and topographically patterned programmed substrates) with biofilms were gently washed three times with 0.85% NaCl solution and stained with SYTO®9 from the Live/Dead® Backlight™ bacterial viability kit (Life Technologies, Carlsbad, CA, USA) before imaging using an upright fluorescence microscope (Axio Imager M1, Carl Zeiss Inc., Berlin, Germany). To determine biomass, 3D information was obtained from a series of z stack images (1 µm interval), which were then analyzed using the software COMSTAT [17]. To prevent the substrates with attached biofilms from drying during imaging, the samples were soaked in clean 0.85% NaCl solution during imaging. After imaging, the surfaces with biofilms were transferred to 0.85% NaCl solution pre-warmed at 40°C for 10 min to trigger shape recovery. After shape change at 40°C for 10 min, the substrates were gently washed three times again with a clean 0.85% NaCl solution and imaged. Flat control substrates incubated at 40°C for 10 min but without shape change (no fixed temporary shape) were used as the control. At least three biological replicates were tested for each condition and six positions were randomly selected and imaged for each surface.

4.3.5 Statistics

All statistical analyses were performed using SAS 9.1.3, Windows version (SAS, Cary, NC, USA). Results with $p < 0.05$ were considered statistically significant.

4.4 Results

4.4.1 P. aeruginosa biofilm removals by shape memory polymer (SMP)

Bacteria can attach to any surface and biofilms are difficult to eradicate once they are formed. To develop a new strategy of biofilm removal, we tested a shape memory polymer (SMP) with topography for removing mature biofilms. SMP is a class of polymeric materials which has an ability to change its deformation from a temporary shape to a permanent shape triggered by stimuli such as heat, light, magnetic field, etc. We used *tert*-butyl acrylate (tBA)-based one-way SMP to apply dynamic topography and added patterns to enhance the performance of biofilm removal [18]. This polymer system was chosen because it has biocompatibility and shape memory effect around glass transition temperature [19].

As shown in Figure 4.2a, about 2.5 logs of biofilms were detached by shape recovery within 10 min after temperature changed to 40°C. With 10 μm deep recessive hexagonal patterns, about 3 logs of 48 h mature biofilms (99.9% of biofilm cells) were removed from the surfaces. These results were corroborated by fluorescence images (Figure 4.2b). To clarify the mechanism of biofilm removal by shape recovery, it was needed to investigate whether the biofilm cells were actively leaving from the surface or passively be detached by dynamic topographic change.

(a)
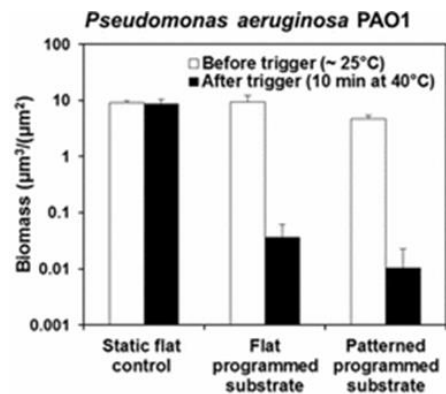
(b)
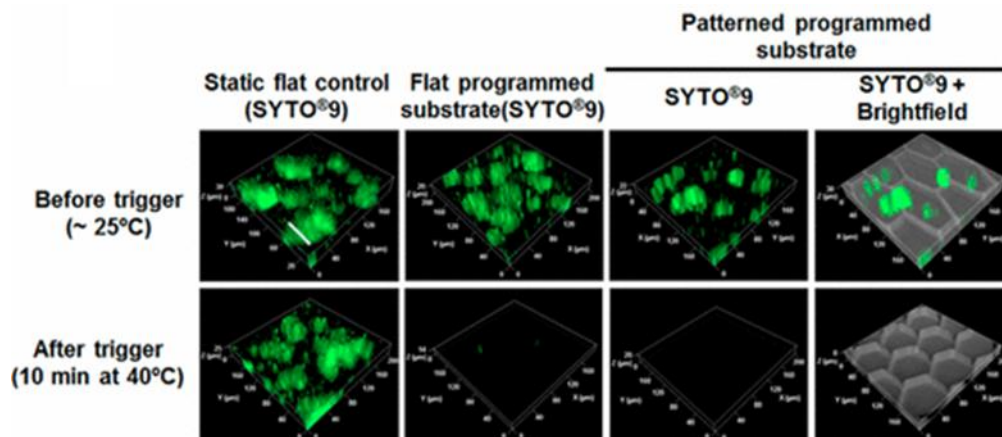
Figure 4.2. Biofilm formation of *P. aeruginosa* PAO1 on static flat control and programmed substrates (both flat substrates and substrates patterned with 10 μm deep recessive hexagonal patterns) fixed with a temporary but stable uniaxial strain of >50% to contract by ~50% when heated to 40 °C. The figures show the biomass (a) and representative fluorescence images (b) of *P. aeruginosa* PAO1 biofilms on different surfaces before and after trigger (10 min incubation at 40°C) (bar = 50 μm). Mean ± standard deviation shown.

4.4.2 Biofilm removal during shape change

Most changes in shape occurred in the first 6 min after shape recovery started (Figure 4.3a and 4.3b). Surface coverage by biofilms was 33.0% before shape recovery (t = 0 s) and dropped to 19.9% after just 4.3 s of shape recovery (Figure 4.3b). At 6 min, surface coverage further decreased to 11.1% (Figure 4.3b). It is worth noticing that this experiment was conducted without flow, and a gentle wash after shape change was sufficient to remove nearly all detached cells (Figures 4.2 and 4.3c). Such detachment was not observed for the static flat control (no shape recovery), which was also incubated at 40°C for 10 min (Figure 4.3d). After 10 min of shape recovery, the same cell clusters remained on these static control surfaces (Figure 4.3d).
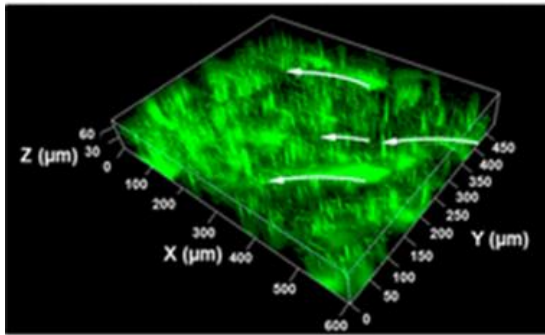
(a)   (b)
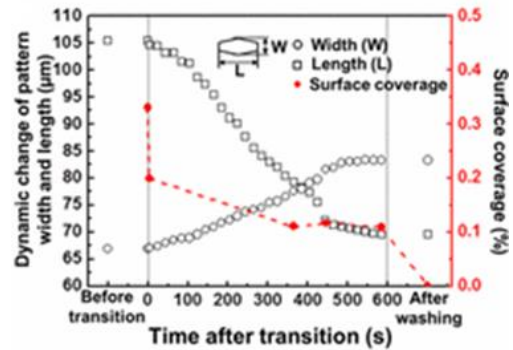
(c)
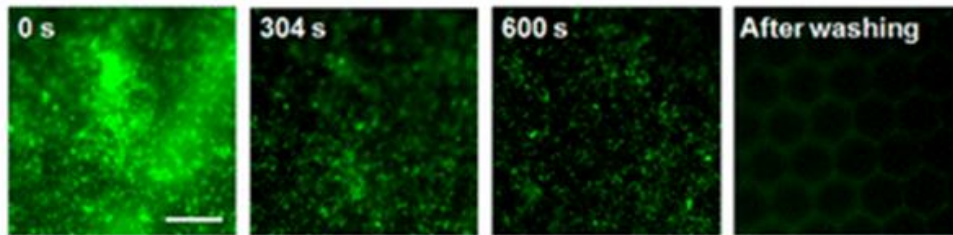
(d)
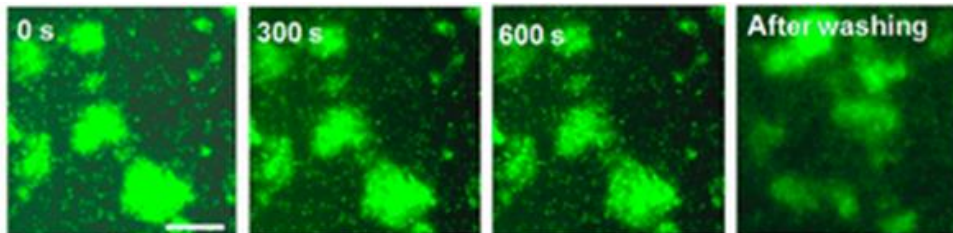
Figure 4.3. Biofilm removal during shape change. (a) A 3D image of *P. aeruginosa* PAO1 biofilm

detachment. This 3D image was taken when the rapid biofilm detachment occurred in the first 4.3 s after

topographic transition started. Due to the fast cell movement, trajectories of detached cells and cell

clusters were recorded as the z stage moved upward (representative cells highlighted using white arrows).

(b) Length and width of recessive hexagonal patterns measured during topographic change and the

surface coverage of *P. aeruginosa* PAO1 biofilms at 0, 4.3, 360, and 600 s after the beginning of shape

recovery and the final surface after washing. (c and d) Fluorescence images of *P. aeruginosa* PAO1

82

biofilms on topographically patterned programmed substrates (c) and static flat control (d) during

triggered shape change (10 min incubation at 40°C) (bar = 50 µm). Images show that cell clusters were

removed from the patterned SMP with shape change but remained on the flat control surfaces.

4.5 Discussion

Despite the extensive research on fouling control during the past decades [20,21], biocompatible materials that offer long-term biofilm control in a complex environment are still yet to be developed. Moreover, removing mature biofilms that have large cell clusters and thick extracellular matrices remains an unmet challenge. In this study, we introduced recessive hexagonal patterns on SMP substrates to inhibit biofilm formation and obtained a dynamic change in surface topography upon triggered shape memory recovery. The shape-change induced biofilm dispersion was fast (~6 min) and can remove large clusters from mature biofilms. This material is also biocompatible [19], and the shape change can be triggered by gentle heating, without using an electric or magnetic field as required by some other systems [22,23].

The topography was created using soft lithography [24]; thus, it is well-defined and can be applied to a large surface area. Despite these advantages, we are aware that this SMP only has one-way shape change. To be broadly adapted for diverse applications, the capability to go through cyclic changes in shape is desirable. Some shape memory polymer chemistries have been demonstrated to have two-way, triple shape, or other forms of multi-shape [25–28]. In the future, we plan to test such polymers to obtain more sustainable antifouling properties. It will also be helpful for biomedical applications to have the temporary shape maintained at body temperature rather than room temperature. With regards to the mechanism of biofilm dispersion, data presented herein revealed that biofilm dispersion was rapid and cell clusters were disrupted. The exact mechanism of shape memory recovery triggered biofilm removal is unknown. We speculate that the observed effects might be caused by the disruption of the biofilm matrix and cell−surface interactions.

4.6 Conclusion

In summary, we developed new antifouling surfaces based on shape memory triggered changes in surface topography. This strategy was found effective for the removal of established biofilms of *P. aeruginosa* PAO1. It is needed to understand the underlying mechanism and develop biocompatible polymers for *in vivo* use. Long-term biofilm control may be possible by employing surface topographies on such polymers to achieve biofilm inhibition and self-cleaning.

4.7 Acknowledgements

4.8 References

[1]   M.N. Dickson, E.I. Liang, L.A. Rodriguez, N. Vollereaux, A.F. Yee, Nanopatterned polymer surfaces with bactericidal properties, Biointerphases. 10 (2015) 021010. https://doi.org/10.1116/1.4922157.

[2]   H. Gu, D. Ren, Materials and surface engineering to control bacterial adhesion and biofilm formation: A review of recent advances, Front. Chem. Sci. Eng. 8 (2014) 20–33. https://doi.org/10.1007/s11705-014-1412-3.

[3]   B.H. Shin, B.H. Kim, S. Kim, K. Lee, Y. Bin Choy, C.Y. Heo, Silicone breast implant modification review: Overcoming capsular contracture, Biomater. Res. 22 (2018) 37. https://doi.org/10.1186/s40824-018-0147-5.

[4]   K. Kapat, P.P. Maity, A.P. Rameshbabu, P.K. Srivas, P. Majumdar, S. Dhara, Simultaneous hydrothermal bioactivation with nano-topographic modulation of porous titanium alloys towards enhanced osteogenic and antimicrobial responses, J. Mater. Chem. B. 6 (2018) 2877–2893. https://doi.org/10.1039/c8tb00382c.

[5]   W.J. Metsemakers, T. Schmid, S. Zeiter, M. Ernst, I. Keller, N. Cosmelli, D. Arens, T.F. Moriarty, R.G. Richards, Titanium and steel fracture fixation plates with different surface topographies: Influence on infection rate in a rabbit fracture model, Injury. 47 (2016) 633–639. https://doi.org/10.1016/j.injury.2016.01.011.

[6]   P.M. Tsimbouri, L. Fisher, N. Holloway, T. Sjostrom, A.H. Nobbs, R.M.D. Meek, B. Su, M.J. Dalby, Osteogenic and bactericidal surfaces from hydrothermal titania nanowires on titanium substrates, Sci. Rep. 6 (2016) 36857. https://doi.org/10.1038/srep36857.

[7]   O. Mrad, J. Saunier, C. Aymes-Chodur, V. Rosilio, S. Bouttier, F. Agnely, P. Aubert, J. Vigneron, A. Etcheberry, N. Yagoubi, A multiscale approach to assess the complex surface of polyurethane catheters and the effects of a new plasma decontamination treatment on the surface properties, Microsc. Microanal. 16 (2010) 764–778. https://doi.org/10.1017/S1431927610093876.

[8]   J. Verran, C.J. Maryan, Retention of Candida albicans on acrylic resin and silicone of different surface topography, J. Prosthet. Dent. 77 (1997) 535–539. https://doi.org/10.1016/S0022-3913(97)70148-3.

[9]   A. Ionescu, E. Wutscher, E. Brambilla, S. Schneider-Feyrer, F.J. Giessibl, S. Hahnel, Influence of surface properties of resin-based composites on in vitro Streptococcus mutans biofilm development, Eur. J. Oral Sci. 120 (2012) 458–465. https://doi.org/10.1111/j.1600-0722.2012.00983.x.

[10]   P.P.C. Pita, J.A. Rodrigues, C. Ota-Tsuzuki, T.F. Miato, E.G. Zenobio, G. Giro, L.C. Figueiredo, C. Gonçalves, S.A. Gehrke, A. Cassoni, J.A. Shibli, Oral streptococci biofilm formation on different implant surface topographies, Biomed Res. Int. 2015 (2015) 1–6. https://doi.org/10.1155/2015/159625.

[11]   B.S. Tseng, W. Zhang, J.J. Harrison, T.P. Quach, J.L. Song, J. Penterman, P.K. Singh, D.L. Chopp, A.I. Packman, M.R. Parsek, The extracellular matrix protects Pseudomonas aeruginosa biofilms by limiting the penetration of tobramycin, Environ. Microbiol. (2013). https://doi.org/10.1111/1462-2920.12155.

[12]   J. Sambrook, D. Russell, Molecular Cloning: A Laboratory Manual, 3rd ed., Cold Spring Harbor Laboratory Press, 2001.

[13]   C.M. Yakacki, S. Willis, C. Luders, K. Gall, Deformation limits in shape-memory polymers, Adv. Eng. Mater. 10 (2008) 112–119. https://doi.org/10.1002/adem.200700184.

[14]   P. Yang, R.M. Baker, J.H. Henderson, P.T. Mather, In vitro wrinkle formation via shape memory dynamically aligns adherent cells, Soft Matter. 9 (2013) 4705. https://doi.org/10.1039/c3sm00024a.

[15]   H. Gu, S. Hou, C. Yongyat, S. De Tore, D. Ren, Patterned Biofilm Formation Reveals a Mechanism for Structural Heterogeneity in Bacterial Biofilms, Langmuir. 29 (2013) 11145–11153. https://doi.org/10.1021/la402608z.

[16]   S. Hou, H. Gu, C. Smith, D. Ren, Microtopographic patterns affect escherichia coli biofilm formation on poly(dimethylsiloxane) surfaces, Langmuir. 27 (2011) 2686–2691. https://doi.org/10.1021/la1046194.

[17]   A. Heydorn, A.T. Nielsen, M. Hentzer, C. Sternberg, M. Givskov, B.K. Ersbøll, S. Molin, Quantification of biofilm structures by the novel computer program comstat, Microbiology. 146 (2000) 2395–2407. https://doi.org/10.1099/00221287-146-10-2395.

[18]   H. Gu, S.W. Lee, S.L. Buffington, J.H. Henderson, D. Ren, On-Demand Removal of Bacterial Biofilms via Shape Memory Activation, ACS Appl. Mater. Interfaces. 8 (2016) 21140–21144. https://doi.org/10.1021/acsami.6b06900.

[19]   C.M. Yakacki, R. Shandas, C. Lanning, B. Rech, A. Eckstein, K. Gall, Unconstrained recovery characterization of shape-memory polymer networks for cardiovascular applications, Biomaterials. 28 (2007) 2255–2263. https://doi.org/10.1016/j.biomaterials.2007.01.030.

[20] V. Levering, C. Cao, P. Shivapooja, H. Levinson, X. Zhao, G.P. López, Urinary catheter capable of repeated on-demand removal of infectious biofilms via active deformation, Biomaterials. 77 (2016) 77–86. https://doi.org/10.1016/j.biomaterials.2015.10.070.

[21] P. Shivapooja, Q. Wang, L.M. Szott, B. Orihuela, D. Rittschof, X. Zhao, G.P. López, Dynamic surface deformation of silicone elastomers for management of marine biofouling: laboratory and field studies using pneumatic actuation, Biofouling. 31 (2015) 265–274. https://doi.org/10.1080/08927014.2015.1035651.

[22] P. Shivapooja, Q. Wang, B. Orihuela, D. Rittschof, G.P. Lõpez, X. Zhao, Bioinspired surfaces with dynamic topography for active control of biofouling, Adv. Mater. 25 (2013) 1430–1434. https://doi.org/10.1002/adma.201203374.

[23] M. Vilfan, A. Potočnik, B. Kavčič, N. Osterman, I. Poberaj, A. Vilfan, D. Babič, Self-assembled artificial cilia, Proc. Natl. Acad. Sci. 107 (2010) 1844–1847. https://doi.org/10.1073/pnas.0906819106.

[24] D. Qin, Y. Xia, G.M. Whitesides, Soft lithography for micro- and nanoscale patterning, Nat. Protoc. 5 (2010) 491–502. https://doi.org/10.1038/nprot.2009.234.

[25] J. Hu, Y. Zhu, H. Huang, J. Lu, Recent advances in shape–memory polymers: Structure, mechanism, functionality, modeling and applications, Prog. Polym. Sci. 37 (2012) 1720–1763. https://doi.org/10.1016/j.progpolymsci.2012.06.001.

[26] Y. Yu, M. Nakano, T. Ikeda, Directed bending of a polymer film by light, Nature. 425 (2003) 145–145. https://doi.org/10.1038/425145a.

[27] A. Agrawal, P. Luchette, P. Palffy-Muhoray, S.L. Biswal, W.G. Chapman, R. Verduzco,

Surface wrinkling in liquid crystal elastomers, Soft Matter. 8 (2012) 7138.

https://doi.org/10.1039/c2sm25734c.

[28] S. Chen, J. Hu, H. Zhuo, Y. Zhu, Two-way shape memory effect in polymer laminates,

Mater. Lett. 62 (2008) 4088–4090. https://doi.org/10.1016/j.matlet.2008.05.073.

Chapter 5

Physiological changes of *Pseudomonas aeruginosa* biofilm cells

by one-way dynamic surface topography

This chapter has been published as below with minor modifications. Sang Won Lee, Huan Gu, James Bryan Kilberg, and Dacheng Ren. Sensitizing bacterial cells to antibiotics by shape recovery triggered biofilm dispersion. *Acta Biomaterialia*. 2018 Nov; 81: 93–102.

5.1 Abstract

Microbial biofilms are a leading cause of chronic infections in humans and persistent biofouling in industries due to the extremely high-level tolerance of biofilm cells to antimicrobial agents. Eradicating mature biofilms is especially challenging because of the protection of the extracellular matrix and the slow growth of biofilm cells. In Chapter 4, we reported that established biofilms can be effectively removed (e.g. 99.9% dispersion of 48 h *Pseudomonas aeruginosa* PAO1 biofilms) by shape memory polymer-based dynamic changes in surface topography. Here, we demonstrate that such biofilm dispersion also sensitizes biofilm cells to conventional antibiotics. For example, shape recovery in the presence of 50 mg/mL tobramycin reduced biofilm cell counts by more than 3 logs (2,479-fold) compared to the static flat control. The
observed effects were attributed to the disruption of biofilm structure and increase in cellular activities as evidenced by an 11.8-fold increase in the intracellular level of adenosine triphosphate (ATP), and a 4.1-fold increase in expression of the *rrnB* gene in detached cells. These results can help guide the design of new control methods to better combat biofilm-associated antibiotic-resistant infections.

5.2 Introduction

Bacteria can survive in challenging environments by attaching to a surface and developing a biofilm that consists of sessile bacterial cells and an extracellular matrix [1]. Cells in mature biofilms are also associated with slow growth, which renders most antibiotics ineffective [2,3]. Consequently, biofilms are up to 1,000 times more tolerant to antibiotics compared to planktonic cells; and biofilms are involved in more than 65% of nosocomial infections according to the Centers for Disease Control and Prevention (CDC) [4–6].

The economical and clinical significance of biofilm-related problems has stimulated intensive research to design more effective anti-fouling strategies [7–10]. To prevent bacteria from colonizing a surface, different approaches have been explored to alter the properties of the substrate materials such as surface chemistry [11–24], topography [8,25,34,35,26–33], and stiffness [36–39]. Strategies for modifying surface chemistry include coating with antibacterial agents [11–13,16,17,20–22] or other compounds that can change the charge [23] or hydrophobicity [15,18,19]. Surface hydrophobicity can also be changed by altering surface topography [35]. Inspired by natural anti-fouling surfaces such as sharkskin [28], lotus leaves [15], taro leaves [19], and cicada wings [26], static micron- and nano-scale patterns and roughness have been created and demonstrated to prevent biofilm formation without using antimicrobial agents that can potentially promote resistance [8,25,34,26–33]. These chemical and physical approaches have been demonstrated to inhibit bacterial adhesion for up to 14 days; however, challenges such as the sustaining efficacy of agents, adverse effects of environmental and host factors (e.g., covering by body fluid or metabolic products during bacterial growth), and the remarkable capabilities of bacteria to adapt to challenging environments can allow bacteria to

94

overcome unfavorable surface properties and eventually form biofilms over time [7]. Thus, it is important to develop new technologies that can effectively remove mature biofilms.

Previous studies showed that, by altering the surface features using pneumatic actuation [40], electrical voltage [41], and air-pressure or water inflation generated strain [42,43], up to 90% of mature biofilm could be removed. In Chapter 4, we demonstrated strong activities of biofilm removal by dynamic changes in surface topography using shape memory polymer (SMP). Using *tert*-butyl acrylate (tBA) based SMP, on-demand shape recovery of the substrate material (both flat SMP and that with micron-scale topographic patterns) can be triggered with gentle heating (10 min at 40°C), which led to effective removal of 48 h *Pseudomonas aeruginosa* biofilms by 99.9% [44]. The observed biofilm removal was attributed to the physical disruption of biofilm structure and cell-surface interactions. Because biofilm and planktonic cells have major differences in physiology and antibiotic susceptibility [45], we hypothesize that shape recovery triggered biofilm dispersion can also alter the antibiotic susceptibility of biofilm cells. To test this hypothesis, we followed the antibiotic susceptibility of biofilm cells before and after shape recovery and compared it with the control surfaces that were not programmed to have shape change (henceforth "static flat control"). We also tracked the changes in intracellular ATP level and gene expression profiles to understand the mechanism of observed results. The findings of this study may help design the next generation of smart anti-fouling materials by combining dynamic surface topography with antimicrobials.

5.3 Materials and Methods

5.3.1 Bacterial strains and medium

P. aeruginosa PAO1 [46] was grown in Lysogeny Broth (henceforth LB medium) [47] consisting of 10 g/L tryptone, 10 g/L NaCl, and 5 g/L yeast extract (Thermo Fisher Scientific, Waltham, MA, USA). The reporter strain PAO1::*rrnB*P1-*gfp(AGA)* was constructed by integrating *rrnB*P1-*gfp(AGA)* into the genome of *P. aeruginosa* PAO1 using the miniTn5 system to monitor the expression of *rrnB* gene with the signal from unstable GFP(AGA).

5.3.2 SMP substrate fabrication

The shape memory polymer was synthesized by following the protocols reported previously [44,48]. Briefly, the shape memory polymer (SMP) was synthesized using t-butyl acrylate (tBA), poly (ethylene glycol)$_n$ dimethacrylate (PEGDMA) with M_n=750 molecular weight, and photoinitiator 2,2-dimethoxy-2-phenylacetophenone (DMPA) (Sigma Aldrich, St. Louis, MO, USA). The weight ratio between tBA and PEGDMA was set as 9:1; and a photoinitiator, DMPA, was added as 0.4 wt.% to synthesize the tBA-co-PEGDMA polymer networks with a transition temperature slightly above the body temperature (37°C). In our previous study [44], this tBA based SMP exhibited a recovery ratio of 98.9% with a glass transition temperature of 44.3°C.

To make flat SMP, a sandwich structure was assembled with two glass slides as frames and a 1 mm thick PDMS spacer in-between. To minimize the adhesion of SMP to the glass slides, the surfaces of both glass slides were modified with RainX. A mixture of tBA, PEGDMA, and DMPA was injected between two glass slides. The mixture spread uniformly into the gap between two glass slides (created by the PDMS spacer) due to the capillary effect. To cure the mixture for pre-polymerization, 365 nm UV radiation was applied for 10 min. Post-curing was

96

conducted at 90°C for 1 h to finish the synthesis of SMP networks. To ensure complete

crosslinking, we compared the swelling ratios after 1, 3, 5, and 10 min of UV exposure and

different amounts of post-curing time. As shown in Figure 5.1a, extending UV exposure time

beyond 3 min did not further change the swelling ratio, indicating that 3 min is sufficient. Figure

5.1b also shows that increasing post-curing time beyond 1 h did not change the swelling ratio.

Thus, we chose 10 min UV exposure with 1 h post-curing under 90°C to ensure complete

crosslinking, and keep consistency with the protocol that we followed [48] and our previous

study [44]. If further developed for real applications, it will be important to test other sterilization

methods that are easier to scale up, e.g. gamma radiation. This is beyond the scope of this study.

However, because we have achieved complete crosslinking, we do not expect significant changes

in biofilm control activities if gamma were used for sterilization.
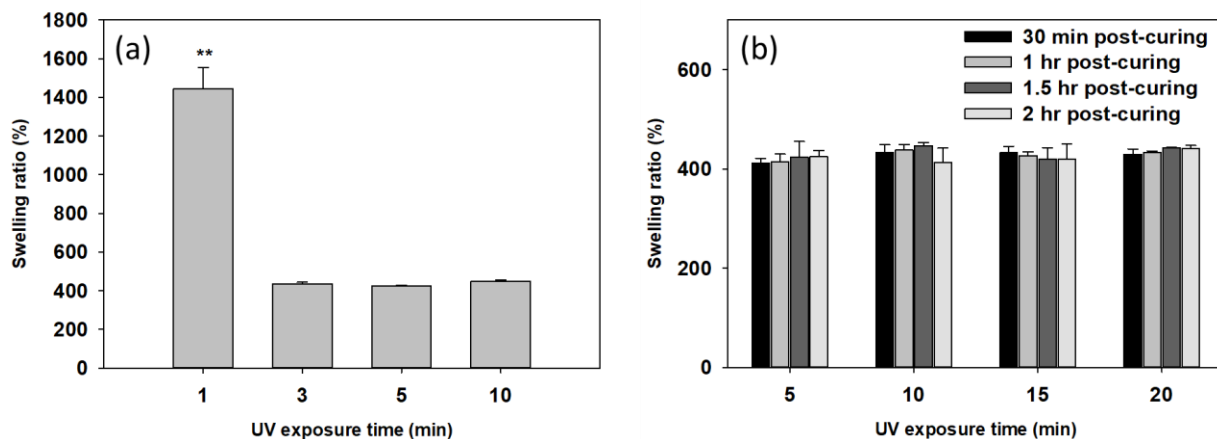
Figure 5.1. The swelling ratio of tBA shape memory polymer prepared by varying UV exposure time

alone (a) and both exposure time and post-curing heating time at 90°C (b) The results indicate that 3 min

of UV exposure is enough to fully crosslink tBA. **p<0.01.

5.3.3 Programmable SMP substrate preparation

To obtain the stretched temporary shape, flat SMPs were cut into a dog bone shape using a manual stretcher. The manual stretcher with the dog bone shape SMP was incubated at 50°C for 8 min and stretched gently by 50% elongation. After the deformation, SMP was cooled to room temperature for 5 min. To recover the SMP with temporary shape, it was incubated in 0.85 wt.% NaCl solution at 40°C for 10 min. In our previous study [44], we have tested the recovery ratio of this SMP and found it is 98.9%.

5.3.4 Biofilm formation

To grow biofilms, SMPs were cut into 0.5 cm by 1.5 cm coupons and then sterilized by exposure to UV for 1 h for each side. Overnight cultures of *P. aeruginosa* PAO1 grown in LB medium were used to inoculate the biofilm cultures in petri dishes containing SMPs to an optical density at 600 nm (OD_{600}) of 0.05. Each petri dish held three biological replicates of SMP coupons. Biofilms were cultured for 48 h at room temperature.

5.3.5 Antibiotic susceptibility test

After 48 h incubation, SMPs with attached biofilms were washed with 0.85 wt.% NaCl solution three times to remove non-specifically attached planktonic cells. After washing, each SMP was transferred to a pre-warmed test tube containing 2 mL of 0.85 wt.% NaCl solution and incubated for 10 min at 40°C to trigger shape change. During this process, the programmed SMP recovered to its permanent shape, while the static flat control maintained its own shape. After the 10 min incubation, shape recovery dispersed biofilm cells were harvested for analysis. For the static flat control samples (biofilms on surfaces without stretching), biofilm cells were harvested by 25 Hz bead beating for 30 s using 0.1 g of 0.1 mm zirconia/silica bead (BioSpec Products,

Inc., Bartlesville, OK, USA). This approach was found effective to detach PAO1 biofilm cells without affecting PAO1 cell viability (Figure 5.2). To avoid any possible confounding effect of bead beating, cells detached by shape recovery were also processed with bead beating for 30 s before further analysis. The harvested biofilm cells were transferred to a 96-well plate and tested for susceptibility to six antibiotics including tobramycin (Tokyo Chemical Industry Co., Tokyo, Japan), ofloxacin (Sigma Aldrich, St. Louis, MO, USA), tetracycline (Sigma Aldrich), minocycline (Sigma Aldrich), ciprofloxacin hydrochloride (Sigma Aldrich), and chloramphenicol (Sigma Aldrich) added at different concentrations. After 1 h incubation at 37°C, samples were washed three times with 0.85wt.% NaCl solution before plating on LB agar plates to count colony forming units (CFU) by following a published protocol [49] after a series dilution.
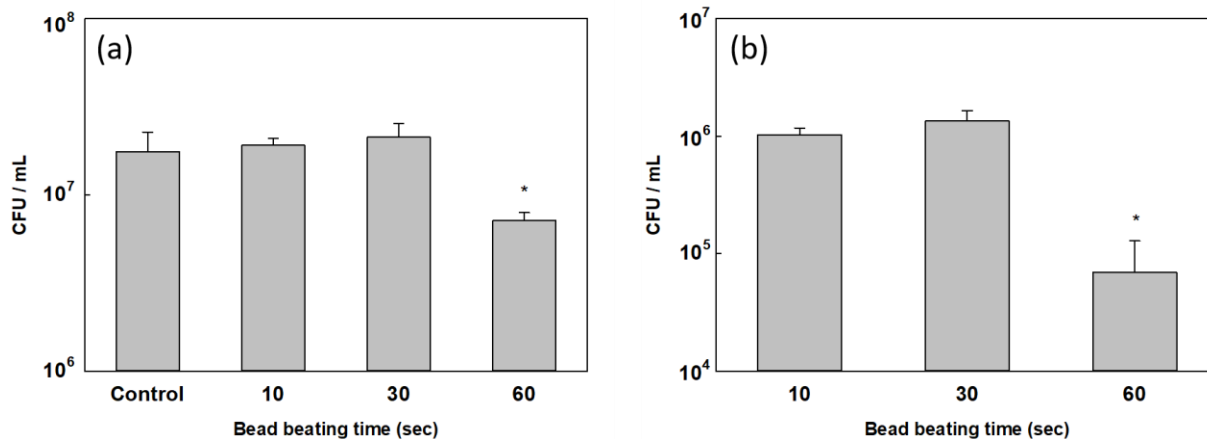
Figure 5.2. Viability of *P. aeruginosa* PAO1 planktonic cells (a) and biofilm cells (b) after bead beating for a different amount of time. The results indicate that 30 s of beating is safe to cells. Bead beating was required to remove biofilms from the surface. Thus, it is impractical to test the 0s sample. *p<0.05.

5.3.6 Biomass quantification and cell viability test

   The 48 h *P. aeruginosa* PAO1 biofilm cells on SMP were stained with SYTO$^®$9 and propidium iodine from the Live/Dead$^®$ Backlight^{TM} bacterial viability kit (Life Technologies, Carlsbad, CA, USA) after three times of washing with 0.85wt% NaCl solution. Imaging analysis was conducted using an upright fluorescence microscope (Axio Imager M1, Carl Zeiss Inc., Berlin, Germany). To quantify the biomass, z stack images with 3D information were obtained followed by quantification analysis using software COMSTAT [50]. Three biological replicates were tested for each condition and five images were randomly obtained for each surface.

5.3.7 Scanning electron microscope (SEM) analysis

   The biofilm cells on SMP substrates with different conditions were analyzed including 48 h biofilms without treatment, biofilm cells detached by bead beating/shape recovery, and SMP substrate surfaces after bead beating/shape recovery. The samples were immersed in a fixing agent containing 2.5% glutaraldehyde (Electron Microscopy Sciences, Hatfield, PA, USA) for 1 h after three times of washing with 0.85wt% NaCl solution. Then, the substrates were transferred into 1% Osmium tetroxide (OsO$_4$, Sigma Aldrich) solution for post-fixation for 1 h followed by further washing steps with 15, 30, 50, 70, 95, and 100% ethanol for 15 min each. The 100% ethanol washing step was conducted three times. The samples were coated using a platinum sputter (Edwards S150A, Edwards, Burgess Hill, England) under 30 mV with 75 sec deposition time. SEM images were obtained using JEOL JSM-IT100LA (JEOL Ltd., Tokyo, Japan). Three biological replicates were imaged with five positions randomly selected from each sample.

5.3.8 Intracellular level of adenosine triphosphate (ATP)

The ENLITEN ATP Assay System (Promega, Madison, WI, USA) was used for the ATP test by following the manufacture's protocol. Briefly, the biofilm cells of both stretched and static flat control samples were obtained as described above. The luminescence of each sample was measured using a microplate reader (BioTek Synergy 2, BioTek, Winooski, VT, USA). We first established a standard curve using samples with known concentrations of ATP. The amount of ATP in actual samples was determined by fitting the ATP standard curve and normalized by the number of cells in each sample. Three replicates were tested for each condition.

5.3.9 Expression level of rrnB

To monitor the growth activity of biofilm cells released by shape recovery and those of the static flat control, an engineered reporter strain, PAO1::*rrnB*$_{P1}$-*gfp* was used to determine the *rrnB* expression level as indicated by the GFP signal intensity. Biofilm cells were harvested as described above in the antibiotic susceptibility test. The intensity of the GFP signal was measured using a BioTek Synergy2 microplate reader and normalized by cell number. Each condition was tested with three replicates.

5.3.10 RNA extraction and cDNA synthesis

Total RNA of detached biofilm cells was extracted using the RNeasy mini kit (Qiagen, Hilden, Germany). Biofilm cells were cultured in the same way as described above except that more and bigger SMP coupons were used to obtain 9 times more cells per sample to ensure the abundance of RNA needed for RNA-seq and quantitative PCR (qPCR) analyses. The cells were collected by centrifugation for 3 min at 8,000 rpm at 4°C. RNA was isolated by following the protocol of the RNeasy mini kit. The purity of RNA samples was evaluated using a Nanodrop tool of microplate

reader EPOCH 2 (BioTek, Winooski, VT, USA). The quality of extracted RNA samples was quantified using an Agilent 2,100 Bioanalyzer (Agilent Technologies, Santa Clara, CA, USA) and the RNA samples with an RNA integrity number (RIN) > 9 were chosen for rRNA depletion using Ribo-zero rRNA removal kit (Illumina, San Diego, CA, USA) prior to RNA-seq analysis.

For qPCR analysis, the extracted RNA samples were used to synthesize cDNA using iScript^{TM} cDNA Synthesis Kit (Bio-Rad, Hercules, CA, USA). The quality of the cDNA samples was checked using the microplate reader as mentioned above.

5.3.11 RNA-seq library construction

RNA-seq libraries were constructed using the NEBNext Ultra RNA Library Prep kit (New England Biolabs, Ipswich, MA, USA). Each library was quantified with Qubit 2.0 (dsDNA HS kit; Thermo Fisher Scientific, Waltham, MA, USA) and the size distribution was determined using a Fragment Analyzer (Advanced Analytical Technologies, Ankeny, IA, USA) prior to pooling. Libraries were sequenced on a NextSeq 500 instrument (Illumina, San Diego, CA, USA) at the RNA Sequencing Core (RSC) Facility at Cornell University. At least 20 M single-end 75 bps reads were generated per library.

5.3.12 Validation of RNA-seq results using quantitative PCR (qPCR) analysis

qPCR analysis was conducted to validate the RNA-seq results. The synthesized cDNA template, DNA primer templates of interest (Table 5.1), and SYBR Green PCR master mix (Thermo Fisher Scientific, Waltham, MA, USA) were well mixed. The qPCR reactions were conducted using an Eppendorf Mastercycler Realplex Thermal Cycler (Eppendorf, Hamburg, Germany) with the following condition: initial denaturation at 95°C for 1 min, followed by 40 cycles of denaturation at 95°C for 10 s and annealing at 60°C for 1 min. The melting curve was

conducted at 95°C for 20 min. The fluorescent signals were measured at the end of each cycle. The expression ratios of the genes of interest were analyzed by the LinReg PCR program (Heart Failure Research Center, Amsterdam, Netherlands). Five representative genes were tested including *proC*, *cynT*, *hirQ*, *hdhA*, *phnW*, *oprB*, *rrnB*, and *kdpB* (Table 5.1). *proC* was chosen as a housekeeping gene as used in previous studies both by us and other groups [51,52].

Table 5.1. Primers used in this study

Selected genes	Forward primer sequence 5' → 3'	Reverse primer sequence 5' → 3'
proC (housekeeping gene)	ACCCCGCATAGCGTTCATC	GGAGACGATCAGTTGCTCCG
cynT	GCTCGCAACTGTTCAAGTCC	GCCGCTTTCGATGTCGTAGA
kdpB	ATGCTGGTGGTCGAACTGAC	CAGGAAGATCAGGGTCAGGC
nirQ	GCGGTATCTGCTACCTGGAC	GGGTTGTAGGACACCACCAG
hdhA	TACTTCACCAACACCTCGCC	AAGCCCTGGACGACATTGAG
phnW	TGGGACAGCGATTTCAACGA	TCATGGCATCGACGATCAGG
rrnB	TGCCTGGTAGTGGGGGATAA	GGACCGTGTCTCAGTTCCAG

5.3.13 Analysis of RNA-seq results

RNA-seq reads were processed with Cutadapt (version 1.8) to trim low quality and adaptor sequences [53]. The mapping process to align the paired-end reads against *P. aeruginosa* PAO1 reference genome was performed using Tophat (version 2.1). Cufflinks (version 2.2) was used to generate fragments per kilobase of transcript per million (FPKM) values and statistical analysis of differential gene expression [54,55]. RNA-seq analysis was conducted with two biological replicates. The results with absolute value of fold change > 2, $p < 0.05$, and $q < 0.05$ were considered significant using Cufflinks (version 2.2) as mentioned above.

5.3.14 Statistics

SAS 9.1.3, Windows version (SAS, Cary, NC, USA), was used for all statistical analyses.

Results with $p < 0.05$ were considered as statistically significant.

5.4 Results

5.4.1 Shape recovery sensitized biofilm cells to bactericidal antibiotics.

To understand if better biofilm control can be obtained by concurrent treatment of biofilms with antibiotics during shape recovery, we first tested shape recovery with 48 h *P. aeruginosa* PAO1 biofilms in the presence of selected conventional antibiotics (including both bactericidal and bacteriostatic agents). The unstretched samples were used as static flat control. As shown in Figure 5.3, after such concurrent treatment with 50 µg/mL tobramycin, 5 µg/mL ofloxacin, 500 µg/mL tetracycline, or 200 µg/mL minocycline, the number of viable cells attached on the surface was reduced by 4.4 ± 0.3 logs, 2.9 ± 0.06 logs, 2.1 ± 0.1 logs, and 3.1 ± 0.05 logs of the original biofilm cell numbers, respectively. These correspond to 2,480, 710, 116, and 962 folds of reduction by tobramycin, ofloxacin, tetracycline, and minocycline, respectively (p values < 0.001, one-way ANOVA adjusted by Tukey test) compared to the static flat control biofilm cells, which went through the same treatment except that the cells were not detached (the SMP was not stretched and thus no shape change) during incubation with the antibiotic.
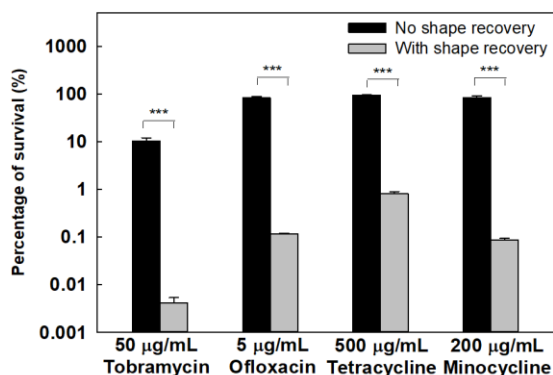
Figure 5.3. Concurrent treatment of *P. aeruginosa* PAO1 biofilm cells. Shape recovery (10 min at 40°C) was triggered in the presence of an antibiotic. Four antibiotics were tested including tobramycin, ofloxacin, tetracycline, and minocycline. *** p<0.001.

The above results demonstrate potent activities in biofilm control. However, the data do not reveal if the effects were due to dispersion, killing by antibiotics, or both. To more specifically evaluate the antibiotic susceptibility of detached cells, we also conducted a sequential treatment with shape recovery followed by antibiotic treatment. After growing *P. aeruginosa* PAO1 for biofilm formation on stretched SMP and static flat controls for 48 h, two types of biofilm cells were harvested including (1) cells dispersed by shape recovery during 10 min incubation of stretched SMPs at 40°C and (2) biofilms cells on static flat controls that went through the same 10 min incubation and detached by bead beating (no effects on cell viability, Figure 5.2) prior to antibiotic treatment. To specifically study the effects of shape recovery on bacterial antibiotic susceptibility, biofilm cells detached by shape recovery were also treated with the same bead beating step as the control samples (the method to harvest biofilm cells of the control samples) before antibiotic treatment. The bead beating process was verified effective for biofilm removal. As shown in Figure 5.4a, compared to the $9.1 \pm 0.8 \ \mu m^3/\mu m^2$ biomass of 48 h *P. aeruginosa* PAO1 biofilms, it was dramatically reduced to $0.04 \pm 0.004 \ \mu m^3/\mu m^2$ and $0.04 \pm 0.03 \ \mu m^3/\mu m^2$ after bead beating or shape recovery, respectively ($p = 0.001$ for both; one-way ANOVA adjusted by Turkey test). These results were corroborated by the SEM images shown in Figure 5.4. To verify that the bead beating condition is safe to cells, we further examined the cells using Live/Dead staining and SEM analysis. No cell death was noted based on Live/Dead staining (Figure 5.5a) and cell integrity was verified by SEM results (Figure 5.5b).
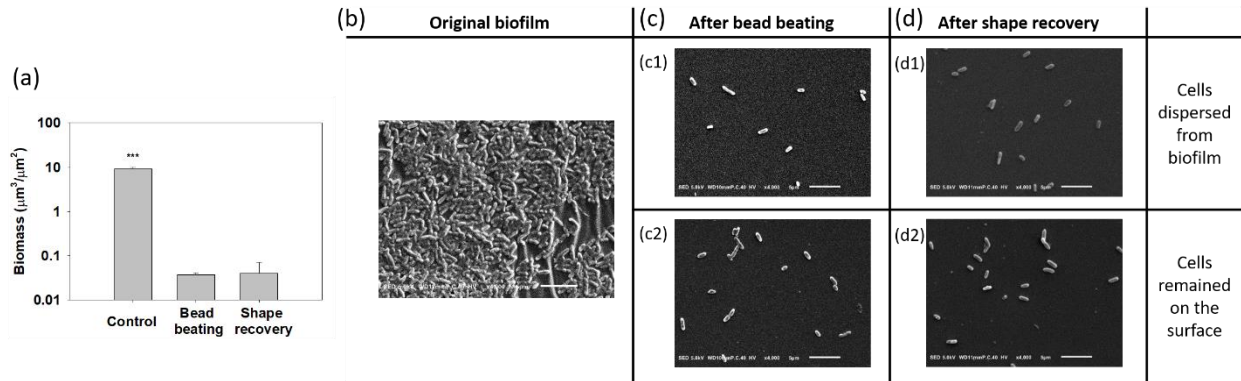
Figure 5.4. SEM analysis of biofilm removal by shape recovery and bead beating. (a) Biomass of 48 h *P. aeruginosa* PAO1 biofilm cells before and after shape recovery or bead beating. (b) Image of 48 h biofilm cells prior to treatment. (c) Biofilm cells after bead beating (c1: detached biofilm cells. c2: Biofilm cells remained on the surface). (d) Biofilm cells after shape recovery (d1: detached biofilm cells. c2: Biofilm cells remained on the surface). *** $p<0.001$. Bar = 5 μm.
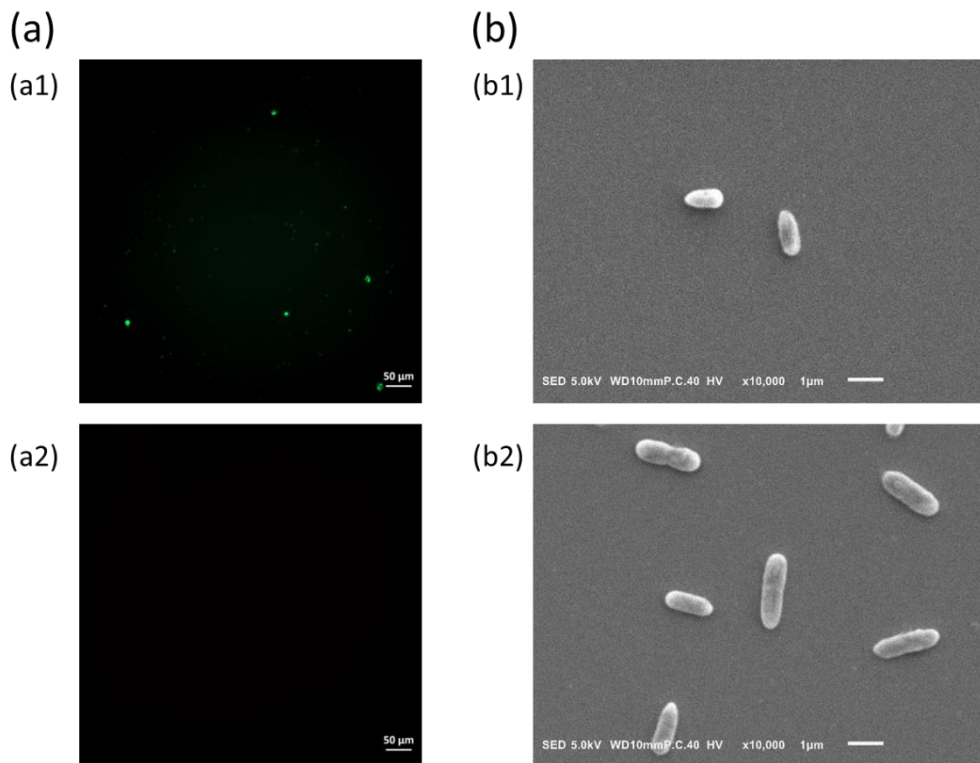
Figure 5.5. Miscropic images of *P. aeruginosa* PAO1 cells after bead beating. (a) Live/Dead staining of *P. aeruginosa* PAO1 biofilm cells after bead beating (a1: GFP. a2: DsRed). (b) SEM images of biofilm

cell morphology after bead beating (b1) and shape recovery (b2). Bar = 50 µm (a1 & a2) or 1 µm (b1 & b2).

After harvesting the biofilm cells, tobramycin was added to treat both the static flat control and shape recovery-dispersed biofilm cells for 1 h. As shown in Figure 5.6a, the log reduction after treatment with 2, 10, and 50 µg/ml tobramycin was 0.7 ± 0.1, 1.2 ± 0.1, and 1.7 ± 0.1, respectively, for static flat control biofilm cells. In comparison, 1.6 ± 0.2, 2.1 ± 0.1, and 2.4 ± 0.1 logs of shape recovery-dispersed biofilm cells were killed, indicating a 0.9 ± 0.2, 0.9 ± 0.01, and 0.7 ± 0.02 log increase in antibiotic susceptibility compared to static flat control ($p = 0.01$, 0.01, and 0.002, one-way ANOVA adjusted by Turkey test). This suggests that shape recovery triggered dispersion did not simply detach biofilm cells via physical forces but affected the physiological stage of biofilm cells.

Consistent with the result of tobramycin, shape recovery triggered dispersion also sensitized the biofilm cells to ofloxacin. As shown in Figure 5.6b, shape recovery released biofilm cells were 0.4 ± 0.1 logs ($p = 0.001$, one-way ANOVA adjusted by Turkey test) more sensitive to 5 µg/mL ofloxacin than the static flat control biofilm cells. Similar results were also obtained for ciprofloxacin (Figure 5.7a). Compared to these three bactericidal antibiotics, biofilms were not sensitized to bacteriostatic antibiotics tested including tetracycline, minocycline, and chloramphenicol (Figure 5.6c, d, and Figure 5.7b). This is likely due to the static nature of these agents and indicates that the detached cells were not actively growing.
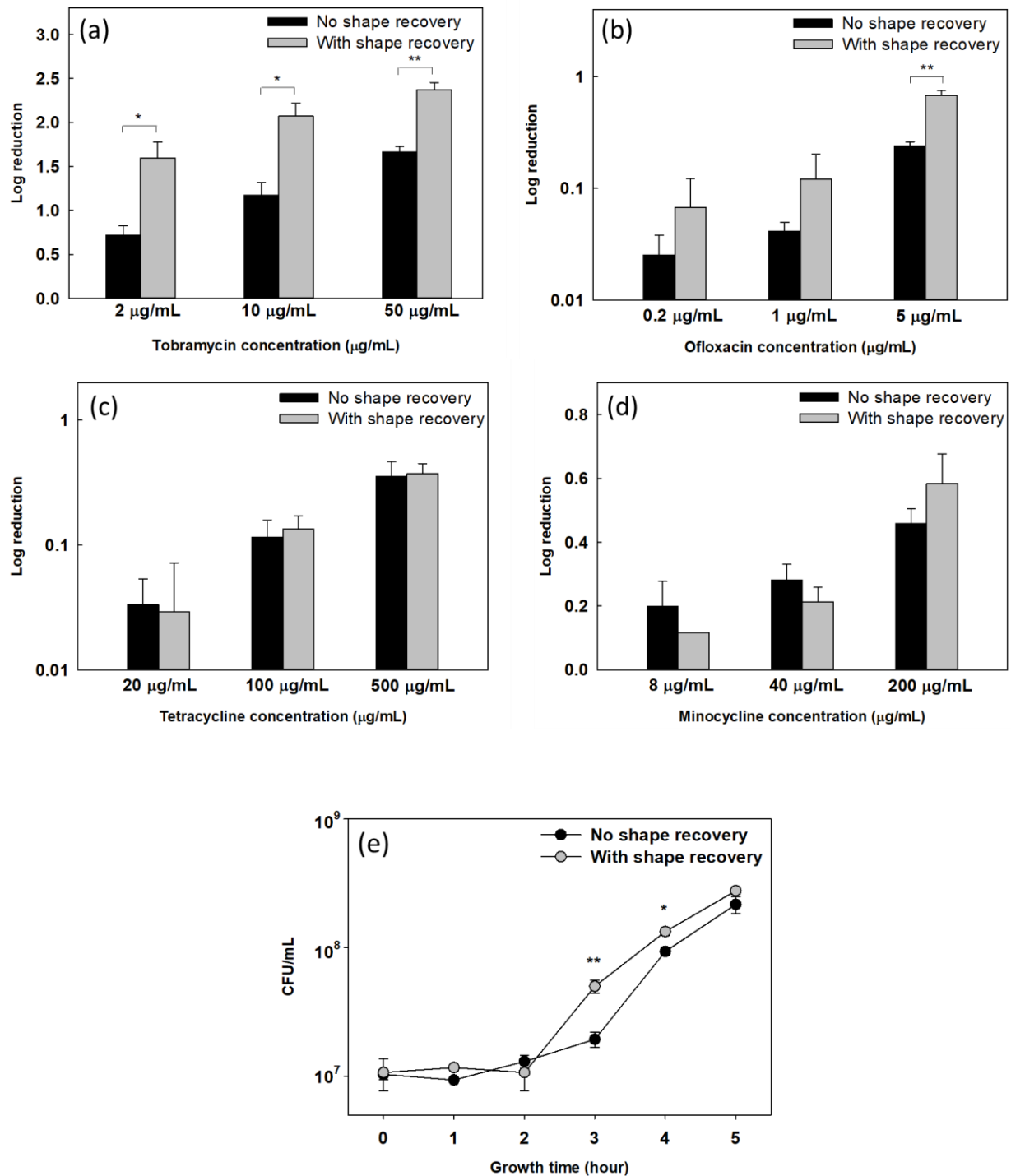
Figure 5.6. Sequential antibiotic susceptibility test on *P. aeruginosa* PAO1 biofilm cells. Four antibiotics were tested by adding to the biofilm cells dispersed by shape recovery including tobramycin (a), ofloxacin (b), tetracycline (c), and minocycline (d). (e) Growth curves of collected biofilm cells. The biofilm cells of

static flat control were detached by bead beating. The biofilm cells released by shape recovery were also processed with bead beating to avoid any confounding effects. * $p<0.05$** $p<0.01$.
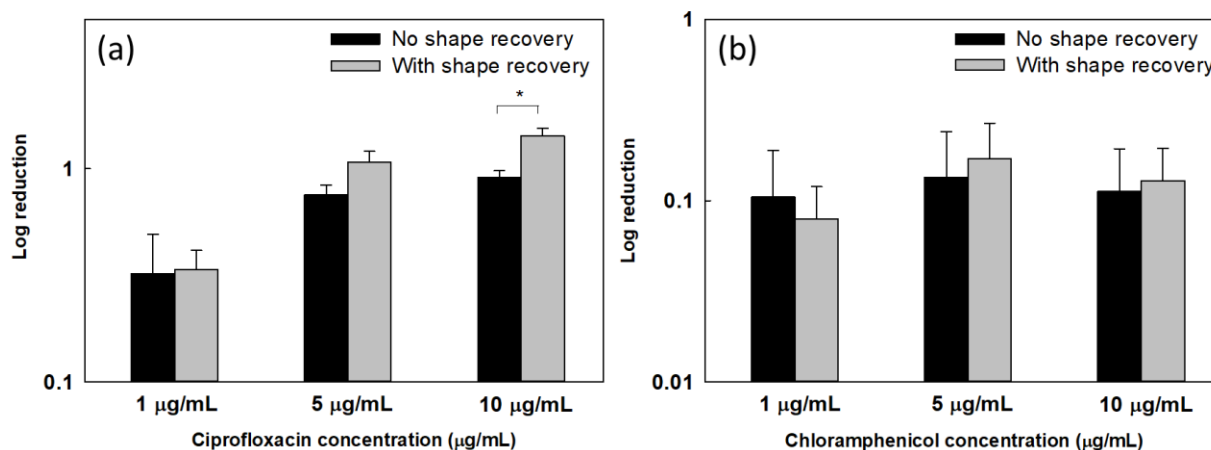
Figure 5.7. Sequential treatment of *P. aeruginosa* PAO1 biofilm cells by adding antibiotics to shape recovery released biofilm cells. This figure shows the results of ciprofloxacin (a) and chloramphenicol (b).

5.4.2 Effects of shape recovery triggered biofilm dispersion on the physiology of P. aeruginosa cells.

An increase in antibiotic susceptibility of dispersed cells led to our speculation that shape recovery may change the physiological stage of biofilm cells. To answer this question, we first tested if dispersion affected the growth of these cells by incubating detached cells in LB medium. After 2 h of inoculation, there was no difference in cell number between shape recovery released cells and the static flat control sample released by bead beating (both were in lag phase; Figure 5.6e). The cells released by shape recovery were also processed by bead beating to avoid any confounding effects. After the lag phase, cells in both samples started growing but at different growth rates. The CFU number of shape recovery released biofilm cells after 3 h and 4 h of incubation was 2.7 ± 0.6 and 1.5 ± 0.2 times higher than the static flat control biofilm cells, respectively ($p = 0.008$ and 0.02, respectively, one-way ANOVA adjusted by Turkey test). This

110

result indicates that the shape recovery released biofilm cells were at a relatively more active stage, which is consistent with their enhanced antibiotic susceptibility.

To understand if shape recovery released cells were more active metabolically, we compared the intracellular level of ATP in *P. aeruginosa* PAO1 biofilm cells between shape recovery samples and static flat controls. ATP level is an indicator of cellular activities and known to be associated with bacterial antibiotic susceptibility [56]. As shown in Figure 5.8a, the ATP level in biofilm cells dispersed by shape recovery was 11.8 ± 2.7 times of the static flat control cells ($p = 0.003$, one-way ANOVA adjusted by Tukey test). This result indicates higher metabolic activities in shape recovery-dispersed cells and corroborates the increase in antibiotic susceptibility of these cells.

Intracellular ATP level is also known to affect the expression of the *rrnB* gene, which encodes 16s rRNA for cell growth [57,58]. Thus, we measured the expression level of the *rrnB* gene using a reporter strain PAO1::*rrnB*P1-*gfp(AGA)*. Consistent with the increase in ATP level, shape recovery triggered dispersion led to a 4.1 ± 0.4-fold increase in *rrnB* expression compared to the static flat control (Figure 5.8b) ($p = 0.007$, one-way ANOVA adjusted by Tukey test). The higher expression level of the *rrnB* gene in dispersed cells was also verified using qPCR (2.0 ± 0.2-fold increase compared to static flat control; $p = 0.002$, one-way ANOVA adjusted by Tukey test). The *rrnB* expression results are consistent with the increase in ATP level and higher antibiotic susceptibility in dispersed biofilm cells.
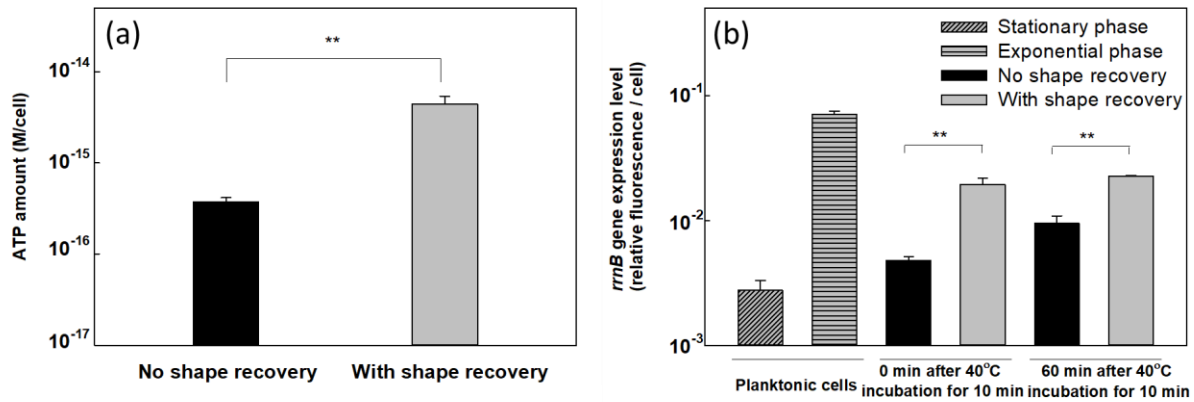
Figure 5.8. (a) Intracellular ATP level in shape recovery released *P. aeruginosa* PAO1 biofilm cells and static flat control. (b) Expression level of *rrnB* gene in *P. aeruginosa* PAO1::*rrnB*$_{P1}$*gfp*$_{(AGA)}$ including planktonic cells, shape recovery released cells, and static flat control. ** *p<0.01*.

5.4.3 Effects of shape recovery on P. aeruginosa gene expression

To further understand the effects of shape recovery triggered biofilm dispersion at the genome-wide scale, RNA-seq analysis was used to compare the gene expression profiles between biofilm cells dispersed by shape recovery and the static flat control. The RNA-seq results indicate that 70 genes were differentially expressed between dispersed cells and the control, including 47 up-regulated genes and 23 down-regulated genes (Tables 5.2 and 5.3). Eight up-regulated genes and 6 down-regulated genes are related to ATP or metabolic activities (Figure 5.9a). Among these genes, *cynT, PA2843, mdlC, katB, phnW, hisD,* and *PA5312* were up-regulated and *PA2550*, *acsA*, *hdhA*, and *glpK* were down-regulated. For ATP-related genes, *nirQ* was up-regulated by 3.1-fold, while *kdpB* was down-regulated by 3.6-fold. *nirQ* encodes denitrification regulatory protein (nitric oxide reductase), also known as ATP-related protein NirQ, which reduces nitric oxide (NO) to nitrous oxide (N_2O) to avoid the accumulation of toxic NO in the cell [59]. During the denitrification process, NirQ induces a concentration gradient of hydrogen ion through cell

112

membrane which leads the synthesis of ATP [60]. *kdpB* is associated with potassium ion (K^+) transport, which requires ATP as an energy source [61]. Thus, the induction of *nirQ* and repression of *kapB* is consistent with the increase in ATP level in dispersed cells.

To validate the RNA-seq data especially the genes related to metabolic activities, qPCR was conducted for 5 representative genes, including *cynT*, *nirQ*, *phnW*, *hdhA*, and *kdpB*, plus *rrnB* discussed above. The *rrnB* gene was not shown in the RNA-seq results because rRNA was depleted during the pretreatment step before sequencing. All 5 representative genes showed consistent results between RNA-seq and qPCR (Figure 5.9b). Thus, the qPCR data validated the RNA-seq results and provided additional evidence that the shape recovery triggered dispersion rendered *P. aeruginosa* biofilm cells to leave the physiological stage of biofilm growth, becoming more active metabolically and consequently more sensitive to antibiotics.
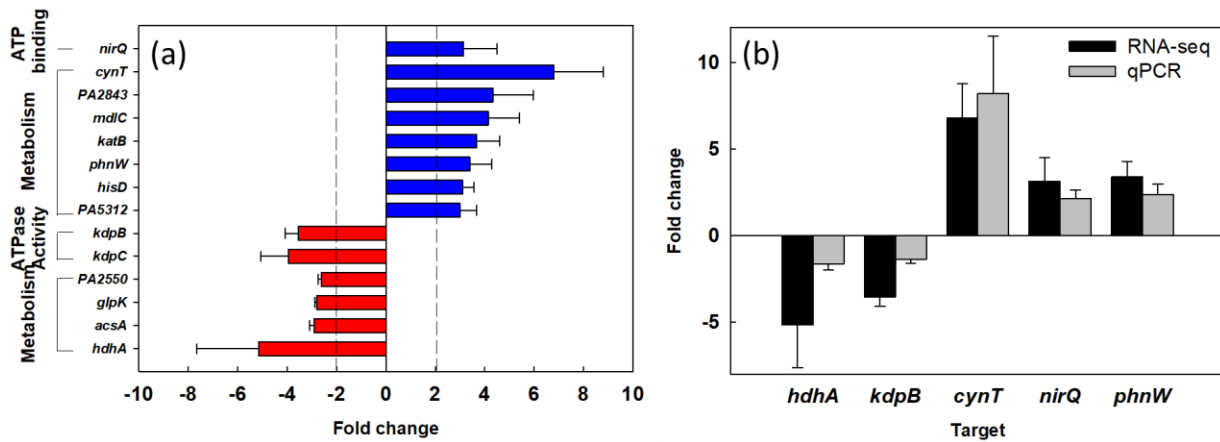
Figure 5.9. Effects of shape recovery triggered dispersion on *P. aeruginosa* PAO1 gene expression. (a) RNA-seq results of induced/repressed genes. (b) qPCR results of representative genes.

Table 5.2. Up-regulated genes in response to dispersion (RNA-seq analysis).

Gene	Log2 (fold change)	Function
PA2807	3.6	Hypothetical
PA3237	3.6	Hypothetical
PA3732	2.9	Hypothetical
PA1137	2.7	Zinc ion binding, oxidation-reduction process
PA1942	2.7	Hypothetical
PA3320	2.7	Hypothetical
PA2753	2.5	Hypothetical
cynT	2.4	Carbonate dehydratase activity
PA1283	2.4	Transcriptional regulators
PA0250	2.4	Hypothetical
PA4610	2.3	Hypothetical
PA3731	2.3	Hypothetical
PA4354	2.3	Hypothetical
PA0449	2.1	Hypothetical
PA2868	2.1	Hypothetical
PA2498	2.1	Hypothetical
PA1503	1.9	Hypothetical
mdlC	1.9	Hypothetical
PA3762	1.9	Hypothetical
PA3287	1.9	Hypothetical
PA3278	1.8	Hypothetical
PA0526	1.7	Hypothetical
katB	1.7	Adaptation (response to oxidative stress, response to stimulus)
phnW	1.7	Metabolic process, organic phosphonate catabolic process
ohr	1.7	Adaptation (response to oxidative stress, response to stimulus)
PA4577	1.6	Hypothetical
nirQ	1.6	ATPase activity, ATP binding
PA4917	1.6	Hypothetical
PA1673	1.6	Hypothetical
PA5312	1.6	Aldehyde dehydrogenase [NAD(P)+] activity
PA3496	1.6	Hypothetical
PA4575	1.6	Hypothetical
PA5494	1.6	Hypothetical
PA0545	1.6	Hypothetical
PA1518	1.6	Hypothetical
PA3662	1.6	Hypothetical
PA2843	1.6	Biosynthetic process
hisD	1.5	Histidine biosynthetic process
ahpC	1.5	Adaptation (response to oxidative stress, response to stimulus)

Gene		Function
PA1029	1.5	Hypothetical
ohrR	1.5	Adaptation (response to oxidative stress, response to stimulus)
PA3238	1.5	Hypothetical
PA0201	1.5	Hypothetical
PA0251	1.5	Hypothetical
PA1140	1.4	Hypothetical
ppgL	1.4	Hypothetical
PA5519	1.4	Hypothetical

Table 5.3. Down-regulated genes in response to dispersion (RNA-seq analysis).

Gene	Log2 (fold change)	Function
PA3518	-2.7	Hypothetical
PA1346	-2.5	Hypothetical
PA3284	-2.4	Hypothetical
PA3283	-2.2	Hypothetical
PA3233	-2.1	Hypothetical
PA3234	-2.1	Transporter activity, membrane protein
hdhA	-2.0	Metabolic process, oxidation-reduction process
PA3519	-2.0	Hypothetical
kdpC	-1.9	Potassium-transporting ATPase activity
PA4637a	-1.9	Hypothetical
kdpB	-1.8	Potassium-transporting ATPase activity
PA1345	-1.6	Hypothetical
PA4023	-1.6	Amino acid transmembrane transport
PA2174	-1.6	Hypothetical
PA4139	-1.5	Hypothetical
acsA	-1.5	Metabolic process, acetyl-CoA biosynthetic process from acetate
PA3919	-1.5	Hypothetical
glpK	-1.5	Carbohydrate metabolic process, phosphotransferase activity
PA3922	-1.5	Hypothetical
oprB	-1.5	Carbohydrate transport
PA2550	-1.4	Acyl-CoA dehydrogenase activity
PA2511	-1.4	Regulation of transcription
PA0107	-1.3	Hypothetical

5.5 Discussion

Despite the well-recognized significance, biofilm control strategies have been largely limited to biofilm prevention and the direct killing of biofilm cells. Eradicating established biofilms remains challenging. Previous research on biofilm removal has been largely based on the use of forces generated by air bubbles [62,63], shock wave [64,65], water jet [66], acoustic energy [67], and magnetically rotating micro rods [68,69]. These conditions can be harsh and require additional equipment, which may hinder *in vivo* applications. In comparison, SMP enabled shape recovery can be achieved under rather gentle conditions such as moderate temperature change in this study, or by the electrical current [70–72] and light [73].

In Chapter 4, we demonstrated that mature biofilms can be effectively removed by using on-demand changes in the substrate configuration of SMP [44]. In the present study, we further demonstrate that such on-demand dispersion can also sensitize biofilm cells to conventional antibiotics. Up to 9-fold increase in antibiotic susceptibility was observed when antibiotics were added after dispersion and more than 3 logs (2,479 times) reduction of biofilm cells was obtained by adding antibiotics during shape recovery. While bactericidal antibiotics showed significant differences between shape recovery conditions and control biofilm cells during sequential treatment, there was no significant difference for bacteriostatic antibiotics tested. This is not unexpected because what we did was a killing test and thus static agents would not show the same effects. It will be interesting to further test different classes of bactericidal compounds.

The synergy between physical factors and antibiotics in biofilm control has been reported. For example, using ultrasound [74,75] or ultrasound targeted microbubble destruction [76] in combination with antibiotics such as gentamicin and vancomycin can enhance the killing of biofilm cells due to the disruption of cell membranes [45]. However, the condition of shape

recovery in this study alone did not cause direct killing of biofilm cells as evidenced by Live/Dead staining and SEM analysis. Also, the released cells were able to grow faster than the static flat control that was detached by bead beating (verified not to affect viability). This result suggests that the effects were through a different mechanism and the cells were not just passively dispersed by shape recovery. Instead, it might be through physiological changes in these cells.

Consistent with the results of antibiotic susceptibility, shape recovery triggered biofilm dispersion led to a higher level of intracellular ATP, slightly faster growth, and significant changes in gene expression in the dispersed cells. No change in the expression of biofilm matrix genes was observed. This is not unexpected because shape recovery happened in minutes; and thus, biofilm dispersion can be largely attributed to physical factors. Nevertheless, the results do indicate that dispersion caused physiological changes to the dispersed cells, which rendered these cells to enter a more active stage and thus more susceptible to bactericidal antibiotics.

Increasing evidence indicates that bacteria have complex systems to sense environmental cues when deciding biofilm formation vs. planktonic growth [37,77–80]. Biofilm cells are also known to disperse naturally when the environment changes to be unfavorable for bacteria to stay [81,82]. Some cell signaling systems have been shown to trigger biofilm dispersion [82–84]. Based on the results of this study, we speculate that biofilm cells may also be able to sense and respond to physical factors and adjust their physiological status for dispersion, which alters antibiotic susceptibility of these cells. Further study on such a sensing mechanism may shed new light on the fundamental understanding of the biofilm life cycle.

Different technologies have been developed for biofilm removal, biofilm killing, or both. However, the options for biofilm removal with gentle conditions are limited. In a recent study, we reported effective (up to 99.9%) biofilm removal using shape memory polymers [44]. Here

we demonstrate that such removal also sensitizes biofilm cells to bactericidal antibiotics. It is encouraging to us since effective eradication of biofilm cells with lower doses of antibiotics can help reduce the risk of resistance development.

We chose room temperature incubation for biofilm growth and 40°C for triggering shape change to be consistent with our previous report [44], and allow us to study the effects on antibiotic susceptibility of dispersed cells specifically. To further develop this technology for *in vivo* applications, the polymer needs to be tested for antifouling activities at human body temperature and evaluated for cytotoxicity to mammalian cells. The temperature for triggering shape change can be adjusted by altering the ratio of tBA and PEGDMA. Alternatively, some shape memory polymers allow shape recovery to be triggered by other means such as electric signal [70–72] and light [73], which may ease medical applications. With further development, this technology has potential applications in medical devices that have major polymer components, e.g. catheters. This is part of our ongoing work.

5.6 Conclusion

The results of this study revealed that dynamic topography by shape recovery can sensitize the detached biofilm cells to conventional antibiotics. Specifically, the biofilm cells released by shape recovery were up to 9-fold more susceptible to antibiotics than the static flat control in sequential treatments; and more than 3 logs of biofilm reduction was achieved by concurrent treatment (shape recovery in the presence of antibiotics). Consistent with the increase in susceptibility to antibiotics, 11.8 times more ATP production and 4.1 times higher *rrnB* expression levels were observed in biofilm cells dispersed by shape recovery compared to the static flat control. These findings were corroborated by RNA-seq and qPCR results and indicate that shape recovery triggered dispersion rendered bacterial cells to leave the physiological stage of biofilm growth and entered a more active and drug-susceptible stage. The graphical abstract summarizes the main findings of this study. Collectively, the findings from this study suggest that effective controls can be developed to eradicate biofilm cells with combined physical (dynamic surface topography) and chemical (antibiotics) factors.

5.7 Acknowledgements

5.8 References

[1]   Hans-Curt Flemming, Jost Wingender Abstract, The Biofilm Matrix, Biofouling. 19
        (2003) 139–150. https://doi.org/10.1080/0892701031000072190.

[2]   I. Olsen, Biofilm-specific antibiotic tolerance and resistance, Eur. J. Clin. Microbiol.
        Infect. Dis. 34 (2015) 877–886. https://doi.org/10.1007/s10096-015-2323-z.

[3]   C.W. Hall, T.-F. Mah, Molecular mechanisms of biofilm-based antibiotic resistance and
        tolerance in pathogenic bacteria, FEMS Microbiol. Rev. 41 (2017) 276–301.
        https://doi.org/10.1093/femsre/fux010.

[4]   L. Hall-Stoodley, J.W. Costerton, P. Stoodley, Bacterial biofilms: from the Natural
        environment to infectious diseases, Nat. Rev. Microbiol. 2 (2004) 95–108.
        https://doi.org/10.1038/nrmicro821.

[5]   P. Sreeramoju, Preventing Healthcare-Associated Infections, Am. J. Med. Sci. (2012) 1.
        https://doi.org/10.1097/MAJ.0b013e31824435e6.

[6]   R.D. Wolcott, G.D. Ehrlich, Biofilms and chronic infections, JAMA - J. Am. Med. Assoc.
        299 (2008) 2682–2684. https://doi.org/10.1001/jama.299.22.2682.

[7]   H. Koo, R.N. Allan, R.P. Howlin, P. Stoodley, L. Hall-Stoodley, Targeting microbial
        biofilms: Current and prospective therapeutic strategies, Nat. Rev. Microbiol. 15 (2017)
        740–755. https://doi.org/10.1038/nrmicro.2017.99.

[8]   H. Gu, D. Ren, Materials and surface engineering to control bacterial adhesion and
        biofilm formation: A review of recent advances, Front. Chem. Sci. Eng. 8 (2014) 20–33.
        https://doi.org/10.1007/s11705-014-1412-3.

[9]   F. Song, H. Koo, D. Ren, Effects of Material Properties on Bacterial Adhesion and
       Biofilm Formation, J. Dent. Res. 94 (2015) 1027–1034.
       https://doi.org/10.1177/0022034515587690.

[10]   K. Liu, L. Jiang, Bio-inspired design of multiscale structures for function integration,
       Nano Today. 6 (2011) 155–175. https://doi.org/10.1016/j.nantod.2011.02.002.

[11]   L. Zhao, P.K. Chu, Y. Zhang, Z. Wu, Antibacterial coatings on titanium implants, J.
       Biomed. Mater. Res. - Part B Appl. Biomater. 91 (2009) 470–480.
       https://doi.org/10.1002/jbm.b.31463.

[12]   E.B.H. Hume, J. Baveja, B. Muir, T.L. Schubert, N. Kumar, S. Kjelleberg, H.J. Griesser,
       H. Thissen, R. Read, L.A. Poole-Warren, K. Schindhelm, M.D.P. Willcox, The control of
       Staphylococcus epidermidis biofilm formation and in vivo infection rates by covalently
       bound furanones, Biomaterials. 25 (2004) 5023–5030.
       https://doi.org/10.1016/j.biomaterials.2004.01.048.

[13]   J.S. Price, A.F. Tencer, D.M. Arm, G.A. Bohach, Controlled release of antibiotics from
       coated orthopedic implants, J. Biomed. Mater. Res. 30 (1996) 281–286.
       https://doi.org/10.1002/(SICI)1097-4636(199603)30:3<281::AID-JBM2>3.0.CO;2-M.

[14]   J. Hasan, R.J. Crawford, E.P. Ivanova, Antibacterial surfaces: The quest for a new
       generation of biomaterials, Trends Biotechnol. 31 (2013) 295–304.
       https://doi.org/10.1016/j.tibtech.2013.01.017.

[15]   X. Zhang, L. Wang, E. Levänen, Superhydrophobic surfaces for the reduction of bacterial
       adhesion, RSC Adv. 3 (2013) 12003. https://doi.org/10.1039/c3ra40497h.

[16]   A. Ewald, S.K. Glückermann, R. Thull, U. Gbureck, D. Lew, Antimicrobial

titanium/silver PVD coatings on titanium, Biomed. Eng. Online. 5 (2006) 22.

https://doi.org/10.1186/1475-925X-5-22.

[17]   K.C. Popat, M. Eltgroth, T.J. LaTempa, C.A. Grimes, T.A. Desai, Decreased

Staphylococcus epidermis adhesion and increased osteoblast functionality on antibiotic-

loaded titania nanotubes, Biomaterials. 28 (2007) 4880–4888.

https://doi.org/10.1016/j.biomaterials.2007.07.037.

[18]   E. Fadeeva, V.K. Truong, M. Stiesch, B.N. Chichkov, R.J. Crawford, J. Wang, E.P.

Ivanova, Bacterial retention on superhydrophobic titanium surfaces fabricated by

femtosecond laser ablation, Langmuir. 27 (2011) 3012–3019.

https://doi.org/10.1021/la104607g.

[19]   J. Ma, Y. Sun, K. Gleichauf, J. Lou, Q. Li, Nanostructure on taro leaves resists fouling by

colloids and bacteria under submerged conditions, Langmuir. 27 (2011) 10035–10040.

https://doi.org/10.1021/la2010024.

[20]   J.R. Chambers, K.E. Cherny, K. Sauer, Susceptibility of Pseudomonas aeruginosa

dispersed cells to antimicrobial agents is dependent on the dispersion cue and class of the

antimicrobial agent used, Antimicrob. Agents Chemother. 61 (2017) 1–18.

https://doi.org/10.1128/AAC.00846-17.

[21]   W.H. Kim, S.B. Lee, K.T. Oh, S.K. Moon, K.M. Kim, K.N. Kim, The release behavior of

CHX from polymer-coated titanium surfaces, Surf. Interface Anal. 40 (2008) 202–204.

https://doi.org/10.1002/sia.2809.

[22]   A.D. Russell, W.B. Hugo, Antimicrobial Activity and Action of Silver, Prog. Med. Chem.

31 (1994) 351–370. https://doi.org/10.1016/S0079-6468(08)70024-9.

[23]   D. Campoccia, L. Montanaro, C.R. Arciola, A review of the biomaterials technologies for infection-resistant surfaces, Biomaterials. 34 (2013) 8533–8554. https://doi.org/10.1016/j.biomaterials.2013.07.089.

[24]   F. Mabboux, L. Ponsonnet, J.J. Morrier, N. Jaffrezic, O. Barsotti, Surface free energy and bacterial retention to saliva-coated dental implant materials - An in vitro study, Colloids Surfaces B Biointerfaces. 39 (2004) 199–205. https://doi.org/10.1016/j.colsurfb.2004.08.002.

[25]   K. Anselme, P. Davidson, A.M. Popa, M. Giazzon, M. Liley, L. Ploux, The interaction of cells and bacteria with surfaces structured at the nanometre scale, Acta Biomater. 6 (2010) 3824–3846. https://doi.org/10.1016/j.actbio.2010.04.001.

[26]   M.N. Dickson, E.I. Liang, L.A. Rodriguez, N. Vollereaux, A.F. Yee, Nanopatterned polymer surfaces with bactericidal properties, Biointerphases. 10 (2015) 021010. https://doi.org/10.1116/1.4922157.

[27]   A.I. Hochbaum, J. Aizenberg, Bacteria pattern spontaneously on periodic nanostructure arrays, Nano Lett. 10 (2010) 3717–3721. https://doi.org/10.1021/nl102290k.

[28]   P. Ball, Shark skin and other solutions, Nat. Eng. 400 (1999) 507–508. https://doi.org/10.1038/22883.

[29]   H. Gu, A. Chen, X. Song, M.E. Brasch, J.H. Henderson, D. Ren, How Escherichia coli lands and forms cell clusters on a surface: A new role of surface topography, Sci. Rep. 6 (2016) 1–14. https://doi.org/10.1038/srep29516.

[30] D. Siegismund, A. Undisz, S. Germerodt, S. Schuster, M. Rettenmayr, Quantification of the interaction between biomaterial surfaces and bacteria by 3-D modeling, Acta Biomater. 10 (2014) 267–275. https://doi.org/10.1016/j.actbio.2013.09.016.

[31] H. Gu, K.W. Kolewe, D. Ren, Conjugation in Escherichia coli Biofilms on Poly(dimethylsiloxane) Surfaces with Microtopographic Patterns, Langmuir. 33 (2017) 3142–3150. https://doi.org/10.1021/acs.langmuir.6b04679.

[32] R. Xing, S.P. Lyngstadaas, J.E. Ellingsen, S. Taxt-Lamolle, H.J. Haugen, The influence of surface nanoroughness, texture and chemistry of TiZr implant abutment on oral biofilm accumulation, Clin. Oral Implants Res. 26 (2015) 649–656. https://doi.org/10.1111/clr.12354.

[33] A. Ionescu, E. Wutscher, E. Brambilla, S. Schneider-Feyrer, F.J. Giessibl, S. Hahnel, Influence of surface properties of resin-based composites on in vitro Streptococcus mutans biofilm development, Eur. J. Oral Sci. 120 (2012) 458–465. https://doi.org/10.1111/j.1600-0722.2012.00983.x.

[34] H. Yan Lin, Y. Liu, D. Wismeijer, W. Crielaard, D. Mei Deng, Effects of Oral Implant Surface Roughness on Bacterial Biofilm Formation and Treatment Efficacy, Int. J. Oral Maxillofac. Implants. 28 (2013) 1226–1231. https://doi.org/10.11607/jomi.3099.

[35] D. Perera-Costa, J.M. Bruque, M.L. González-Martín, A.C. Gómez-García, V. Vadillo-Rodríguez, Studying the influence of surface topography on bacterial adhesion using spatially organized microtopographic surface patterns, Langmuir. 30 (2014) 4633–4641. https://doi.org/10.1021/la5001057.

[36] F. Song, H. Wang, K. Sauer, D. Ren, Cyclic-di-GMP and oprF are involved in the

response of Pseudomonas aeruginosa to substrate material stiffness during attachment on polydimethylsiloxane (PDMS), Front. Microbiol. 9 (2018) 1–13. https://doi.org/10.3389/fmicb.2018.00110.

[37] F. Song, M.E. Brasch, H. Wang, J.H. Henderson, K. Sauer, D. Ren, How Bacteria Respond to Material Stiffness during Attachment: A Role of Escherichia coli Flagellar Motility, ACS Appl. Mater. Interfaces. 9 (2017) 22176–22184. https://doi.org/10.1021/acsami.7b04757.

[38] Y. Zhao, F. Song, H. Wang, J. Zhou, D. Ren, Phagocytosis of Escherichia coli biofilm cells with different aspect ratios: a role of substratum material stiffness, Appl. Microbiol. Biotechnol. 101 (2017) 6473–6481. https://doi.org/10.1007/s00253-017-8394-2.

[39] F. Song, D. Ren, Stiffness of cross-linked poly(dimethylsiloxane) affects bacterial adhesion and antibiotic susceptibility of attached cells, Langmuir. 30 (2014) 10354–10362. https://doi.org/10.1021/la502029f.

[40] P. Shivapooja, Q. Wang, L.M. Szott, B. Orihuela, D. Rittschof, X. Zhao, G.P. López, Dynamic surface deformation of silicone elastomers for management of marine biofouling: laboratory and field studies using pneumatic actuation, Biofouling. 31 (2015) 265–274. https://doi.org/10.1080/08927014.2015.1035651.

[41] P. Shivapooja, Q. Wang, B. Orihuela, D. Rittschof, G.P. Lõpez, X. Zhao, Bioinspired surfaces with dynamic topography for active control of biofouling, Adv. Mater. 25 (2013) 1430–1434. https://doi.org/10.1002/adma.201203374.

[42] V. Leveri, Q. Wang, P. Shivapooja, X. Zhao, G.P. Lõpez, Soft Robotic Concepts in Catheter Design: an On-demand Fouling-release Urinary Catheter, Adv Heal. Mater. 3

(2014) 1588–1596. https://doi.org/10.1002/ana.22528.Toll-like.

[43] P. Shivapooja, Q. Yu, B. Orihuela, R. Mays, D. Rittschof, J. Genzer, G.P. López, Modification of Silicone Elastomer Surfaces with Zwitterionic Polymers: Short-Term Fouling Resistance and Triggered Biofouling Release, ACS Appl. Mater. Interfaces. 7 (2015) 25586–25591. https://doi.org/10.1021/acsami.5b09199.

[44] H. Gu, S.W. Lee, S.L. Buffington, J.H. Henderson, D. Ren, On-Demand Removal of Bacterial Biofilms via Shape Memory Activation, ACS Appl. Mater. Interfaces. 8 (2016) 21140–21144. https://doi.org/10.1021/acsami.6b06900.

[45] C.M. Runyan, J.C. Carmen, B.L. Beckstead, J.L. Nelson, R. a Robison, W.G. Pitt, Low-frequency ultrasound increases outer membrane permeability of Pseudomonas aeruginosa., J. Gen. Appl. Microbiol. 52 (2006) 295–301. https://doi.org/10.2323/jgam.52.295.

[46] B.S. Tseng, W. Zhang, J.J. Harrison, T.P. Quach, J.L. Song, J. Penterman, P.K. Singh, D.L. Chopp, A.I. Packman, M.R. Parsek, The extracellular matrix protects Pseudomonas aeruginosa biofilms by limiting the penetration of tobramycin, Environ. Microbiol. 86 (2013) n/a-n/a. https://doi.org/10.1111/1462-2920.12155.

[47] G. Bertani, Studies on lysogenesis. I. The mode of phage liberation by lysogenic Escherichia coli., J. Bacteriol. 62 (1951) 293–300. https://doi.org/citeulike-article-id:149214.

[48] C.M. Yakacki, S. Willis, C. Luders, K. Gall, Deformation limits in shape-memory polymers, Adv. Eng. Mater. 10 (2008) 112–119. https://doi.org/10.1002/adem.200700184.

[49] S. Sieuwerts, F.A.M. De Bok, E. Mols, W.M. De Vos, J.E.T. Van Hylckama Vlieg, A simple and fast method for determining colony forming units, Lett. Appl. Microbiol. 47 (2008) 275–278. https://doi.org/10.1111/j.1472-765X.2008.02417.x.

[50] A. Heydorn, A. Heydorn, A.T. Nielsen, A.T. Nielsen, M. Hentzer, M. Hentzer, Quantication of biofilm structures by the novel computer program, Image Process. 146 (2000) 2395–2407. https://doi.org/10.1099/00221287-146-10-2395.

[51] J. Pan, A.A. Bahar, H. Syed, D. Ren, Reverting Antibiotic Tolerance of Pseudomonas aeruginosa PAO1 Persister Cells by (Z)-4-bromo-5-(bromomethylene)-3-methylfuran-2(5H)-one, PLoS One. 7 (2012). https://doi.org/10.1371/journal.pone.0045778.

[52] H. Savli, A. Karadenizli, F. Kolayli, S. Gundes, U. Ozbek, H. Vahaboglu, Expression stability of six housekeeping genes: A proposal for resistance gene quantification studies of Pseudomonas aeruginosa by real-time quantitative RT-PCR, J. Med. Microbiol. 52 (2003) 403–408. https://doi.org/10.1099/jmm.0.05132-0.

[53] M. Martin, Cutadapt removes adapter sequences from high-throughput sequencing reads, EMBnet.Journal. 17 (2011) 10. https://doi.org/10.14806/ej.17.1.200.

[54] A. Dobin, T.R. Gingeras, Comment on " TopHat2 : accurate alignment of transcriptomes in the presence of insertions , deletions and gene fusions " by Kim et al ., (2013) 0–9. https://doi.org/10.1101/000851.

[55] C. Trapnell, D.G. Hendrickson, M. Sauvageau, L. Goff, J.L. Rinn, L. Pachter, Differential analysis of gene regulation at transcript resolution with RNA-seq, Nat. Biotechnol. 31 (2013) 46–53. https://doi.org/10.1038/nbt.2450.

[56] Y. Shan, A. Brown Gandt, S.E. Rowe, J.P. Deisinger, B.P. Conlon, K. Lewis, ATP-Dependent Persister Formation in Escherichia coli, MBio. 8 (2017) 1–18. https://doi.org/10.1128/mBio.02267-16.

[57] D.A. Schneider, T. Gaal, R.L. Gourse, NTP-sensing by rRNA promoters in Escherichia coli is direct, Proc. Natl. Acad. Sci. 99 (2002) 8602–8607. https://doi.org/10.1073/pnas.132285199.

[58] B.J. Paul, W. Ross, T. Gaal, R.L. Gourse, rRNA Transcription in Escherichia coli, Annu. Rev. Genet. 38 (2004) 749–770. https://doi.org/10.1146/annurev.genet.38.072902.091347.

[59] H. Arai, T. Kodama, Y. Igarashi, Effect of nitrogen oxides on expression of the nir and nor genes for denitrification in Pseudomonas aeruginosa, FEMS Microbiol. Lett. 170 (1999) 19–24. https://doi.org/10.1016/S0378-1097(98)00517-5.

[60] R.K. Thauer, K. Jungermann, K. Decker, Energy conservation in chemotrophic anaerobic bacteria., Bacteriol. Rev. 41 (1977) 100–180. https://doi.org/10.1073/pnas.0803850105.

[61] W. Kühlbrandt, Biology, structure and mechanism of P-type ATPases, Nat. Rev. Mol. Cell Biol. 5 (2004) 282–295. https://doi.org/10.1038/nrm1354.

[62] H. Jang, R. Rusconi, R. Stocker, Biofilm disruption by an air bubble reveals heterogeneous age-dependent detachment patterns dictated by initial extracellular matrix distribution, Npj Biofilms Microbiomes. 3 (2017) 0–1. https://doi.org/10.1038/s41522-017-0014-5.

[63] S.A. Crusz, R. Popat, M.T. Rybtke, M. Cámara, M. Givskov, T. Tolker-Nielsen, S.P. Diggle, P. Williams, Bursting the bubble on bacterial biofilms: A flow cell methodology,

Biofouling. 28 (2012) 835–842. https://doi.org/10.1080/08927014.2012.716044.

[64]   N.C. Francis, W. Yao, W.S. Grundfest, Z.D. Taylor, Laser-Generated Shockwaves as a
Treatment to Reduce Bacterial Load and Disrupt Biofilm, IEEE Trans. Biomed. Eng. 64
(2017) 882–889. https://doi.org/10.1109/TBME.2016.2581778.

[65]   D.P. Gnanadhas, M. Elango, S. Janardhanraj, C.S. Srinandan, A. Datey, R.A. Strugnell, J.
Gopalan, D. Chakravortty, Successful treatment of biofilm infections using shock waves
combined with antibiotic therapy, Sci. Rep. 5 (2015) 1–13.
https://doi.org/10.1038/srep17440.

[66]   N. Abramzon, J.C. Joaquin, J. Bray, G. Brelles-Mariño, Biofilm destruction by RF high-
pressure cold plasma jet, IEEE Trans. Plasma Sci. 34 (2006) 1304–1309.
https://doi.org/10.1109/TPS.2006.877515.

[67]   N. Dror, M. Mandel, Z. Hazan, G. Lavie, Advances in Microbial Biofilm Prevention on
Indwelling Medical Devices with Emphasis on Usage of Acoustic Energy, Sensors. 9
(2009) 2538–2554. https://doi.org/10.3390/s90402538.

[68]   L.O. Mair, A. Nacev, R. Hilaman, P.Y. Stepanov, S. Chowdhury, S. Jafari, J. Hausfeld,
A.J. Karlsson, M.E. Shirtliff, B. Shapiro, I.N. Weinberg, Biofilm disruption with rotating
microrods enhances antimicrobial efficacy, J. Magn. Magn. Mater. 427 (2017) 81–84.
https://doi.org/10.1016/j.jmmm.2016.10.100.

[69]   I.B. Gomes, M. Lemos, L. Mathieu, M. Simões, L.C. Simões, The action of chemical and
mechanical stresses on single and dual species biofilm removal of drinking water bacteria,
Sci. Total Environ. 631–632 (2018) 987–993.
https://doi.org/10.1016/j.scitotenv.2018.03.042.

[70] S.S. Mahapatra, S.K. Yadav, H.J. Yoo, M.S. Ramasamy, J.W. Cho, Tailored and strong electro-responsive shape memory actuation in carbon nanotube-reinforced hyperbranched polyurethane composites, Sensors Actuators, B Chem. 193 (2014) 384–390. https://doi.org/10.1016/j.snb.2013.12.006.

[71] X. Qi, P. Dong, Z. Liu, T. Liu, Q. Fu, Selective localization of multi-walled carbon nanotubes in bi-component biodegradable polyester blend for rapid electroactive shape memory performance, Compos. Sci. Technol. 125 (2016) 38–46. https://doi.org/10.1016/j.compscitech.2016.01.023.

[72] J.W. Cho, J.W. Kim, Y.C. Jung, N.S. Goo, Electroactive shape-memory polyurethane composites incorporating carbon nanotubes, Macromol. Rapid Commun. 26 (2005) 412–416. https://doi.org/10.1002/marc.200400492.

[73] A. Lendlein, H. Jiang, O. Jünger, R. Langer, Light-induced shape-memory polymers, Nature. 434 (2005) 879–882. https://doi.org/10.1038/nature03496.

[74] G.T. Ensing, B.L. Roeder, J.L. Nelson, J.R. Van Horn, H.C. Van Der Mei, H.J. Busscher, W.G. Pitt, Effect of pulsed ultrasound in combination with gentamicin on bacterial viability in biofilms on bone cements in vivo, J. Appl. Microbiol. 99 (2005) 443–448. https://doi.org/10.1111/j.1365-2672.2005.02643.x.

[75] G.T. Ensing, D. Neut, J.R. van Horn, H.C. van der Mei, H.J. Busscher, The combination of ultrasound with antibiotics released from bone cement decreases the viability of planktonic and biofilm bacteria: An in vitro study with clinical strains, J. Antimicrob. Chemother. 58 (2006) 1287–1290. https://doi.org/10.1093/jac/dkl402.

[76] N. He, J. Hu, H. Liu, T. Zhu, B. Huang, X. Wang, Y. Wu, W. Wang, D. Qu, Enhancement

of vancomycin activity against biofilms by using ultrasound-targeted microbubble destruction, Antimicrob. Agents Chemother. 55 (2011) 5331–5337. https://doi.org/10.1128/AAC.00542-11.

[77] F. Song, H. Koo, D. Ren, Effects of material properties on bacterial adhesion and biofilm formation, J. Dent. Res. 94 (2015) 1027–1034. https://doi.org/10.1177/0022034515587690.

[78] L.D. Renner, D.B. Weibel, Physiochemical regulation of biofilm formation, MRS Bull. 36 (2011) 347–355. https://doi.org/10.1557/mrs.2011.65.Physicochemical.

[79] R. Belas, Biofilms, flagella, and mechanosensing of surfaces by bacteria, Trends Microbiol. 22 (2014) 517–527. https://doi.org/10.1016/j.tim.2014.05.002.

[80] P.P. Lele, B.G. Hosu, H.C. Berg, Dynamics of mechanosensing in the bacterial flagellar motor, Proc. Natl. Acad. Sci. 110 (2013) 11839–11844. https://doi.org/10.1073/pnas.1305885110.

[81] S.K. Kim, J.H. Lee, Biofilm dispersion in Pseudomonas aeruginosa, J. Microbiol. 54 (2016) 71–85. https://doi.org/10.1007/s12275-016-5528-7.

[82] J.B. Kaplan, Biofilm Dispersal: Mechanisms, Clinical Implications, and Potential Therapeutic Uses, J. Dent. Res. 89 (2010) 205–218. https://doi.org/10.1177/0022034509359403.

[83] C. Solano, M. Echeverz, I. Lasa, Biofilm dispersion and quorum sensing, Curr. Opin. Microbiol. 18 (2014) 96–104. https://doi.org/10.1016/j.mib.2014.02.008.

[84] C.N.H. Marques, D.G. Davies, K. Sauer, Control of biofilms with the fatty acid signaling

molecule cis-2-Decenoic acid, Pharmaceuticals. 8 (2015) 816–835.

https://doi.org/10.3390/ph8040816.

Chapter 6

Removal of *Pseudomonas aeruginosa* biofilms using reversible dynamic surface topographies

6.1 Abstract

Bacteria can colonize essentially any surface and form biofilms which are multicellular structures embedded in an extracellular matrix. Due to high-level resistance to antimicrobial agents, the significance of developing strategies to eliminate microbial biofilms in the biomedical field is growing. As described in Chapter 4, we developed a one-way shape memory polymer (SMP) that can create dynamic surface topography to remove 99.9% of 48 h *Pseudomonas aeruginosa* PAO1 biofilms via shape recovery effect. We further demonstrated that such a dynamic substratum can sensitize the detached biofilm cells to antibiotics, which was attributed to an increase in its metabolic activity and ribosome gene expression in Chapter 5. However, this SMP can only have recovery once, limiting its potential for long-term biofilm control. To prove the concept that biofilm can be more effectively removed by repeated shape change, we synthesized reversible shape memory polymers (rSMPs) with varying molecular weights of poly(ε-caprolactone) diisocyanatoethyl dimethacrylate (PCLDIMA), with 25 wt.% butyl acrylate (BA) as a linker, and 1 wt.% benzoyl peroxide (BPO) as a thermal initiator. Among various combinations of PCLDIMA with different molecular weights, we chose a 2:1 wt. ratio mixture of 2,000 g/mol and 15,000 g/mol PCLDIMA, which showed a transition temperature around body temperature (36.8°C). The synthesized rSMP demonstrated good reversible shape recovery for up to 3 cycles. We demonstrated up to 94.3±1.1% removal of 48 h *P. aeruginosa* PAO1 biofilm cells after three consecutive shape recovery cycles. Moreover, the detached biofilm cells were 5.0±1.2 times more prone to 50 µg/mL tobramycin than the biofilm cells on the static control. To the best of our knowledge, it is the first application of reversible SMP for biofilm control.

6.2 Introduction

Microorganisms can attach to any surfaces and develop multicellular structures known as biofilms. With a complex 3D structure and protection of an extracellular matrix, biofilms allow microbes to survive under challenging conditions such as antimicrobial agents and host immune systems [1–3]. In addition, the slow growth of bacterial cells in mature biofilms further contributes to the ineffectiveness of antibiotics, making biofilms highly difficult to control [4,5]. Although modern technologies have gradually reduced healthcare-associated infection (HAI) rates in the past decade [6], chronic infection associated with biofilms is still a major concern.

The significant challenges of biofilms have triggered intensive research on antifouling strategies. A common strategy is surface coating with antimicrobials [7–9] or creating materials that release antimicrobials [10–12] to kill bacterial cells directly. Alternatively, physical means have been explored to modify surface properties such as charge [13], hydrophobicity [14–17], stiffness [18–21], and topography [22–26]. Unfortunately, most methods developed to date are limited to short-term *in vitro* conditions. Long-term infection control is still challenging short duration of antimicrobial protection, and the capability of biofilm bacteria to overcome unfavorable conditions and host immune response [27,28]. New technologies are needed for long-term biofilm control.

Dynamic surface topography has been studied recently as an approach to remove mature biofilms. Epstein *et al.* [29] demonstrated up to 80% removal of 24 h *P. aeruginosa* biofilm from PDMS surfaces by creating 2 μm dynamic wrinkles with uniaxial mechanical strain. Pneumatic actuation [30], electrical voltage [31], magnetic field [32], and air pressure [33] were also used as a mean to change a surface and remove well-formed biofilms. In Chapter 4, we achieved on-demand biofilm control using *tert*-butyl acrylate (tBA) based shape memory polymer (SMP)

which demonstrated 99.9% removal of 48 h *P. aeruginosa* biofilm compared to the static control [34]. In addition, we found that cells detached by dynamic topography were sensitized to antibiotics static control [35]. However, one-way SMP can only go through shape change once, which limits its biomedical applications, especially for long-term use.

In this study, we synthesized a caprolactone based copolymer which has a reversible shape memory effect. We characterized the melting temperatures of the copolymers by changing the combination of caprolactone molecular weights. The reversible shape memory polymer (rSMP) with the melting temperature around body temperature was chosen and the shape recovery performance was investigated for its effects on biofilm removal and antibiotic susceptibility of detached cells.

6.3 Materials and Methods

6.3.1 Copolymer synthesis

Oligo(ε-caprolactone)diols (OCLs) was synthesized through a ring-opening polymerization reaction (Figure 6.1) using ε-caprolactone, ethylene glycol, 1,2-dichloroethane, and dibutyltin oxide as catalyst (Sigma Aldrich, St. Louis, MO, USA) as described previously [36]. The crude products were purified using silica gel and hexane (Sigma Aldrich, St. Louis, MO, USA). For end-group functionalization of OCLs, 2-isocyanatoethyl methacrylate (Sigma Aldrich, St. Louis, MO, USA) was added with dibutyltin dilaurate as catalyst (Sigma Aldrich, St. Louis, MO, USA) and dichloromethane as solvent (Sigma Aldrich, St. Louis, MO, USA) [37]. After synthesis, a mixture of hexane/methanol/diethyl ether (18:1:1) (Sigma Aldrich, St. Louis, MO, USA) was used to purify poly(ε-caprolactone) diisocyanatoethyl dimethacrylate (PCLDIMA) [37]. To obtain a final product of reversible shape memory polymers (rSMPs), PCLDIMAs with two different molecular weights were crosslinked with butyl acrylate (BA; Sigma Aldrich, St. Louis, MO, USA) under a thermal initiator benzoyl peroxide (BPO; Sigma Aldrich, St. Louis, MO, USA). A 1wt.% thermal initiator, BPO, was used to initiate the polymerization at high temperature (90°C) condition.
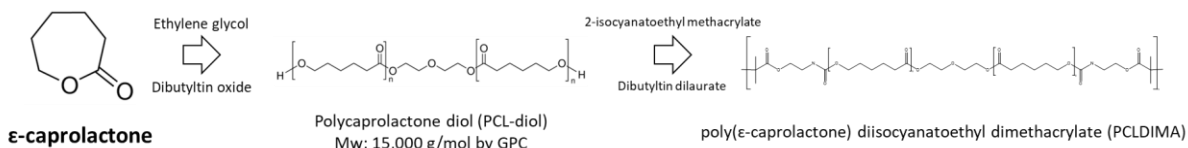
Figure 6.1. Schematic of polymer synthesis. Reactions for the synthesis of PCL-diol via ring-opening polymerization and PCLDIMAs. The rSMP was crosslinked with PCLDIMAs of two different molecular weights with adding 25 wt.% butyl acrylate (BA), and 1 wt.% benzoyl peroxide (BPO).

6.3.2 Programmable rSMP substrate preparation

To demonstrate a reversible shape recovery effect, flat rSMPs were programmed into a 18°

curved shape. The flat rSMP was incubated at 60°C for 10 min and the 18° (from the bottom)

curved shape was fixed using a glass cylinder and a tape. The tape-fixed rSMP was cooled down

to room temperature for 10 min to maintain its 18° curved shape and then the tape was removed.

The shape recovery performance was conducted between 0°C and 40°C for 10 min at each

temperature.

For a stretched rSMP, the flat surfaces were cut into a dog bone shape and stretched gently (in

10 min) with 18% elongation at 60°C using a manual stretcher. Under fixation, the stretched

rSMP was then cooled to room temperature for 10 min. To recover the programmed rSMP, it

was incubated in 0.85 wt.% NaCl solution at a low temperature (0°C or room temperature) and

then a high temperature (40°C) for 10 min at each temperature. These two incubation steps

comprise a cycle of shape recovery. The performance of a shape recovery test and a biofilm

removal test were conducted up to 3 cycles.

6.3.3 Bacterial strain and medium

Pseudomonas aeruginosa PAO1 [38] was grown at 37°C in Lysogeny Broth (henceforth LB

medium) [39] consisting of 10 g/L NaCl, 10 g/L tryptone, and 5 g/L yeast extract (Thermo Fisher

Scientific, Waltham, MA, USA).

6.3.4 Biofilm formation

To grow biofilms, rSMPs were sterilized by exposing UV light for 1 h each side, and *P.*

aeruginosa PAO1 was used to inoculate each biofilm culture in a petri dish containing sterilized

rSMP samples (three in each) to an optical density at 600 nm (OD_{600}) of 0.05. The biofilm samples were cultured at room temperature for 48 h before shape recovery.

6.3.5 Biomass

The effects of biofilm removal were evaluated using imaging analysis. First, the 48 h *P. aeruginosa* PAO1 biofilms were washed with 0.85 wt.% NaCl solution three times and stained with a Live/Dead® Backlight™ bacterial viability kit (Life Technologies, Carlsbad, CA, USA) for 15 min. The stained biofilm cells were then imaged using an upright fluorescence microscope (Axio Imager M1, Carl Zeiss Inc., Berlin, Germany). Biomass of biofilms was quantified by analyzing 3D Z-stack images using COMSTAT [40]. Three biological replicates were analyzed for each condition with five different positions randomly selected from each sample.

6.3.6 Antibiotic susceptibility

Antibiotic susceptibility of biofilm cells was determined by following the same procedure described in our previous studies [35,41]. Briefly, rSMPs with attached biofilm cells were washed three times with 0.85 wt.% NaCl solution and transferred to a 40°C pre-warmed test tube containing 2 mL of 0.85 wt.% fresh NaCl solution. After incubation for 10 min, the sample was moved to a test tube at room temperature containing the same 0.85 wt.% NaCl solution. Three cycles of temperature changes were applied. For the programmed rSMPs, biofilm cells detached by shape recovery were harvested upon the completion of the 3rd cycle of shape recovery. The biofilm cells on flat rSMPs were harvested by bead beating with the maximum frequency for 30 s using 0.1 g of 0.1 mm zirconia/silica bead (BioSpec Products, Inc., Bartlesville, OK, USA). To avoid the confounding effect of bead beating, the same process was also conducted with the biofilm cells detached by shape recovery. The harvested biofilm cells from both the programmed

rSMP and the control rSMP were then treated with 50 µg/mL tobramycin (Tokyo Chemical Industry Co., Tokyo, Japan) for 1 h at 37°C and washed three times with 0.85 wt.% NaCl solution. The washed samples were plated on LB agar plates to count colony forming units (CFU) [42] and determine antibiotic susceptibility by comparing to untreated controls.

6.3.7 Statistics

SAS 9.1.3, Windows version (SAS, Cary, NC, USA), was used for all statistical analyses. Data with $p < 0.05$ were considered as statistically significant.

6.4 Results

6.4.1 rSMP synthesis

   To synthesize a copolymer of rSMP, poly(ε-caprolactone) diisocyanatoethyl dimethacrylate (PCLDIMAs) with two different molecular weights need to be crosslinked with 25 wt.% butyl acrylate (BA) and 1 wt.% thermal initiator, benzoyl peroxide (BPO). Due to the combination of PCLDIMAs with two different molecular weights, the melting temperature can be adjusted. For possible use of rSMPs in biomedical applications, the melting temperature was adjusted around body temperature, 36.5°C, as indicated by differential scanning calorimetry (DSC) analysis. Among all combinations of copolymers shown in Table 6.1, two molecular weights of PCLDIMA (2,000 g/mol and 15,000 g/mol) with a weight ratio 2:1 was chosen to form the backbone of shape memory polymer with 25 wt.% BA added as a crosslinker (shown 36.8°C, Figure 6.2, for the melting temperature). A wide range of melting temperature was obtained with reversible shape recovery effects.

Table 6.1. Melting temperatures of copolymers crosslinked between PCLDIMAs of different molecular weights and 25 wt.% BA with 1 wt.% BPO.

Mw (g/mol)	400	600	2,000	4,000	8,000	15,000
400		-	-	24.5°C	47.1°C	-
600	-		-	32.9°C	47.6°C	-
2,000	-	-		-	-	45.4°C
4,000	24.5°C	32.9°C	-		45.5°C	53.3°C
8,000	47.1°C	47.6°C	-	45.5°C		-
15,000	-	-	43.2°C (1:1) / 36.7°C (2:1)	53.3°C	-	
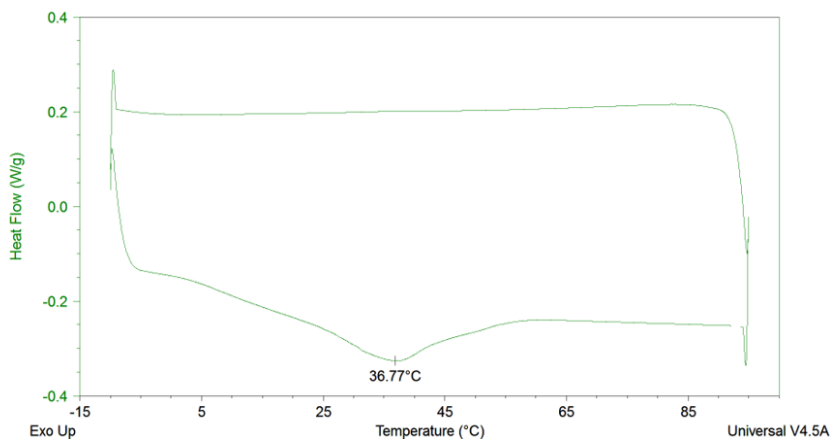
Figure 6.2. DSC result of a copolymer crosslinked between PCLDIMAs, 2,000 g/mol, and 15,000 g/mol, with a ratio of 2:1 and 25 wt.% BA as a crosslinker with 1 wt.% BPO as a thermal initiator.

6.4.2 Reversible shape recovery

Based on the melting temperature of 36.8°C, two temperatures were set up at 0°C and 40°C for repeated shape recovery. The reversible shape recovery was conducted three cycles first and then the high temperature gradually increased 5°C every cycle up to 60°C after the 3rd cycle to verify the reproducibility of the shape recovery effect in terms of the applied temperature. Figure 6.3 summarizes of shape recovery test results. A temporary U shape (18° curved from the bottom) of the rSMP was programmed and set as an initial state. At 40°C, the initially programmed rSMP changed its deformation into a widely opened phase (12°) and it was deformed back into a slightly opened phase (15°) at 0°C. After 1st cycle of shape recovery, the rSMP was at a more opened state (15°) than the initially programmed U shape presumably (18°) due to the reorientation of polymer chains. However, both the opened U shapes at 40°C and 0°C, respectively, were maintained over time by the 3rd cycle. As the set high temperature increased 5°C after the 3rd cycle, the rSMP gradually lost its original U shape. At 60°C the surface became

143

flat (0°). This result was expected because the applied high temperature of 60°C, exceeded the

range of melting temperature for programmed deformation.
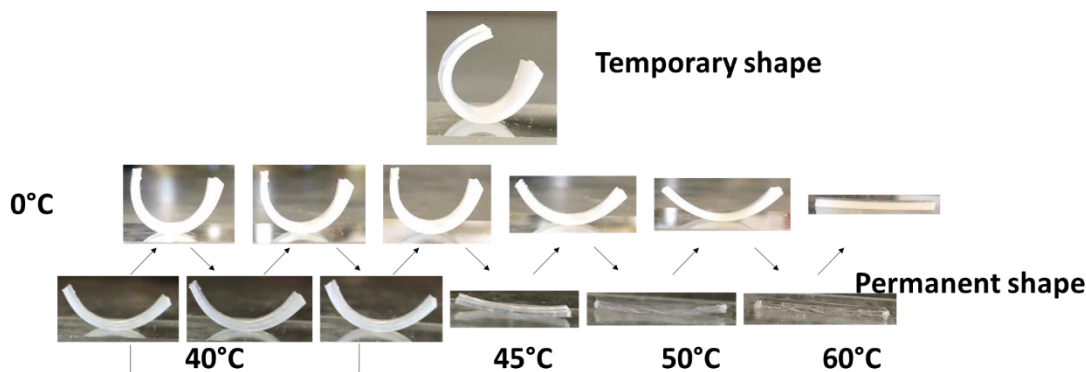
Figure 6.3. Reversible shape recovery of 2,000 and 15,000 g/mol (2:1 ratio) rSMPs (with adding 25 wt.%
BA and 1 wt.% BPO).

6.4.3 Biofilm removal by reversible shape recovery

After confirming repeated shape change, we tested biofilm removal by stretching rSMPs

bidirectionally with 18% elongation. *P. aeruginosa* PAO1 was cultured to form biofilms on UV-

sterilized rSMP samples at room temperature for 48 h. Each cycle of shape recovery was

conducted between 0°C and 40°C and the biomass on the substratum was measured through a

Live/Dead staining process and fluorescent microscopy. The collected 3D Z-stacked images

were quantified using COMSTAT [40]. Figure 6.4a shows good shape recovery by 3rd cycles,

e.g., 96.9±1.0% at the end of 3 cycles. As shown in Figure 6.4b, the biomass of *P. aeruginosa*

PAO1 was significantly reduced by shape recovery. There was no significant change of the

biomass on the flat control after 3 cycles of shape recovery. In comparison, the biomass on the

programmed rSMPs was 55.0±6.1, 77.6±6.5, and 93.6±0.8% lower than the flat control at every

cycle of shape recovery (p=0.004, 0.036, and 0.00004, t-test), corresponding to a total of

94.3±1.0% biomass reduction after 3 cycles compared to the biomass on the initial stage of the

programmed rSMPs (p<0.001, one way repeated measures ANOVA adjusted by Turkey test). The CFU results were corroborated by fluorescence microscopy, Figure 6.4c, which showed a substantial reduction of surface coverage.

(a)

(b)

(c)
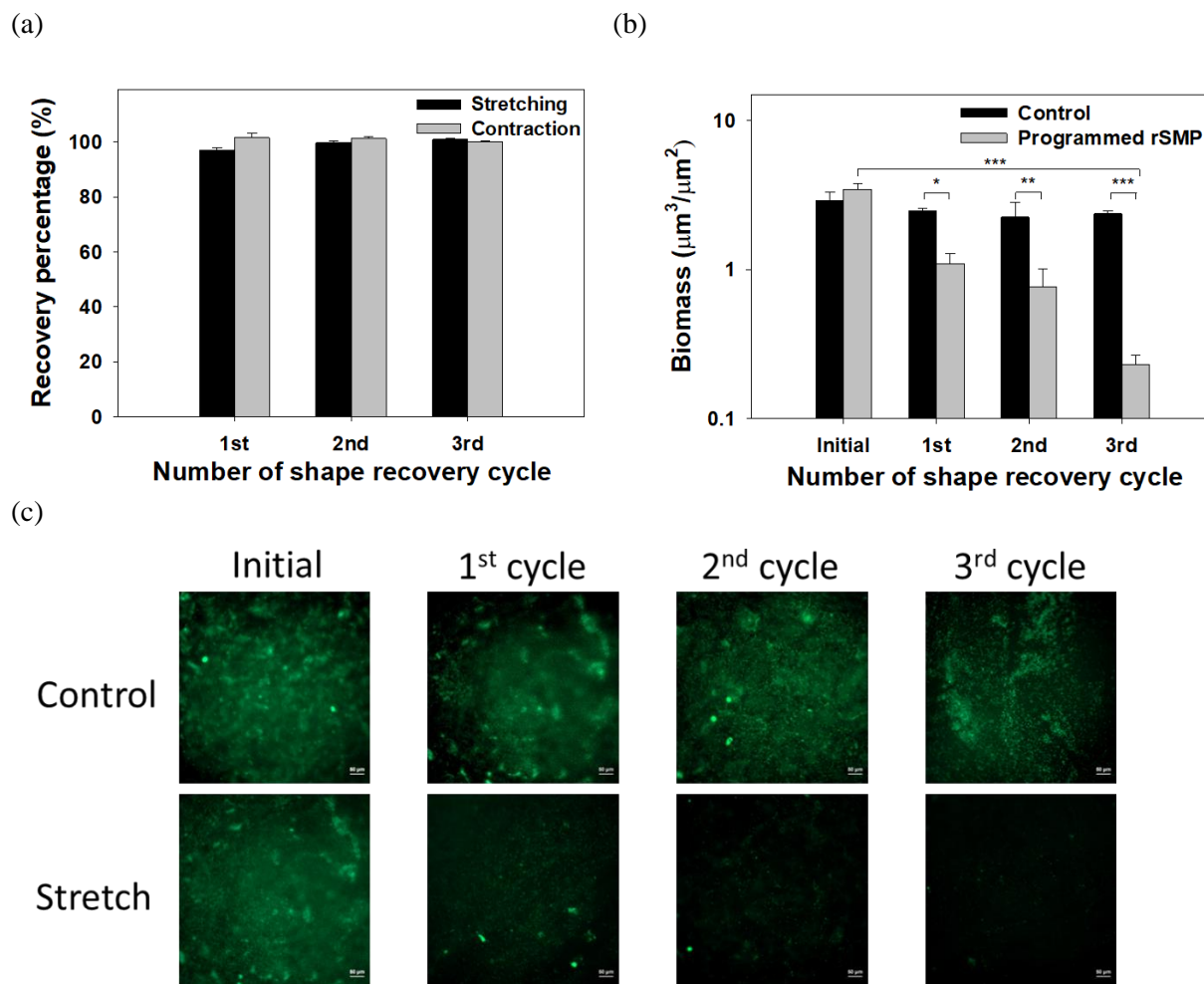
Figure 6.4. Shape recovery behavior and biofilm removal (0 degree and 40 degree). (a) The shape recovery percentage of the synthesized polymers. (b) Biomass after each cycle. (c) Representative images of biofilms. *p < 0.05, **p < 0.01, ***p<0.001.

The experiments above demonstrate the feasibility of additional biofilm removal using repeated shape recovery. However, 0°C is rather harsh for many applications. We repeated the biofilm tests between room temperature and 40°C. The effects were less potent than 0°C, but

145

significant biofilm removal was obtained; e.g., 21.6±1.7% (p=0.014, t-test) after 3 cycles of shape recovery, Figure 6.5a. The biofilm results are consistent with shape recovery property (Figure 6.5b) and the results of fluorescence microscopy (Figure 6.5c).

(a)

(b)

(c)
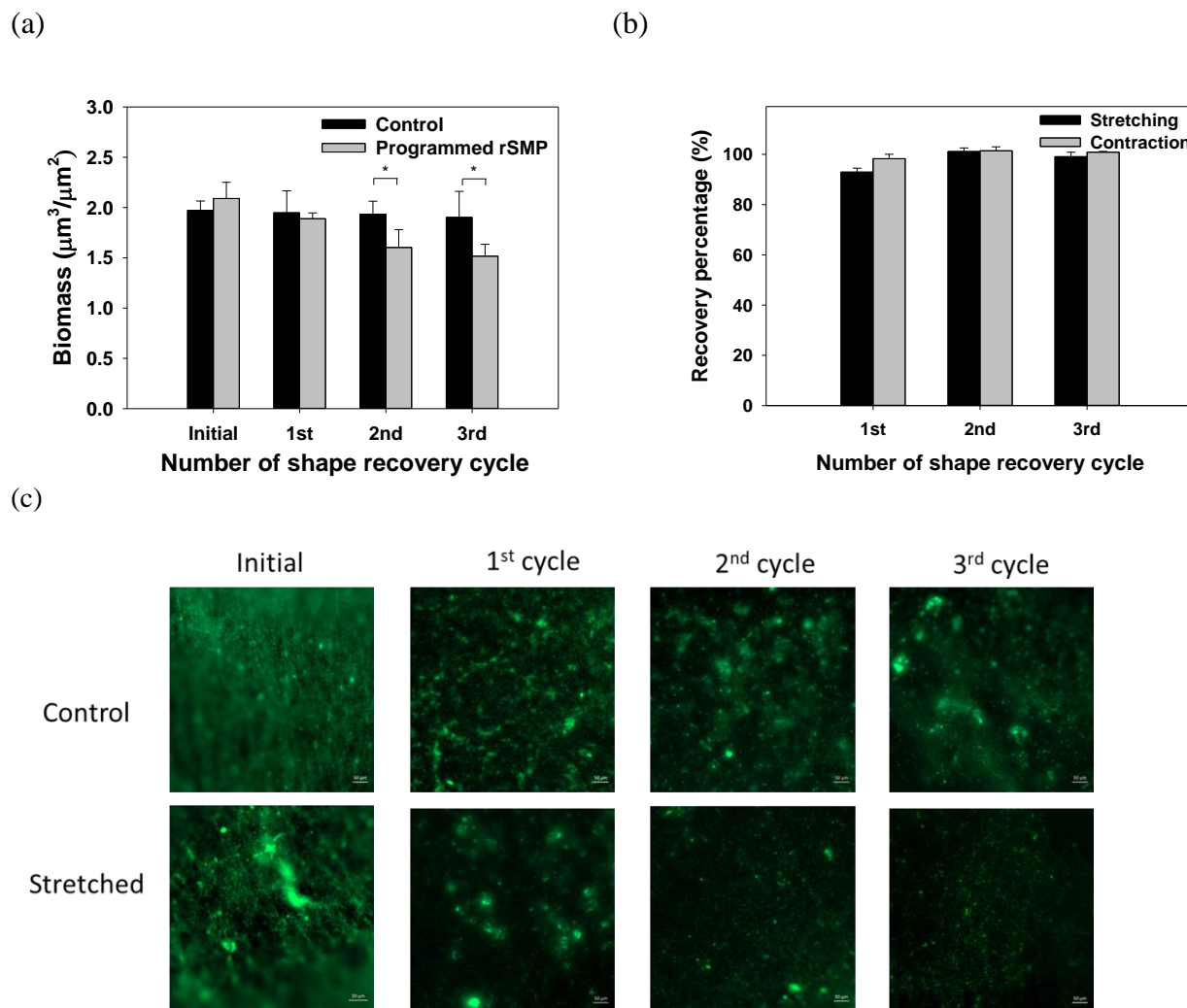
Figure 6.5. Shape recovery behavior and biofilm removal (0 degree and RT). (a) Biomass after each cycle. (b) The shape recovery percentage of the synthesized polymers. (c) Representative images of biofilms. *p < 0.05.

6.4.4 Reproducibility of biofilm removal through shape recovery

Repeatable shape recovery brings a possibility for long-term biofilm control. To test this hypothesis, we transferred the rSMP after the 1st shape recovery into a fresh LB media to grow the biofilm again for 48 h at room temperature. As shown in Figure 6.6a, the biomass of the remained biofilm cells after 1st shape recovery from the programmed rSMP slightly decreased (5.9±3.5%) and went up again after culturing in the fresh LB medium for 48 h. There was no significant difference in biomass between 'after 1st shape recovery' and 'regrown biofilm cells' (Figure 6.6a, p=0.087, t-test) and the fluorescent microscopic images (Figure 6.6b). However, after the regrown biofilm for 2 days, the biofilm removal via shape recovery was significantly increased after three consecutive cycles of shape recovery (a total of 4th shape recovery cycle) which showed a total of 32.8±7.2% biomass reduction (p=0.007, t-test) compare to the flat control. Fluorescence microscopy results support the CFU data (Figure 6.6b). Thus, biofilm removal was obtained overtime after the repeated shape recovery of rSMPs.

(a)

(b)
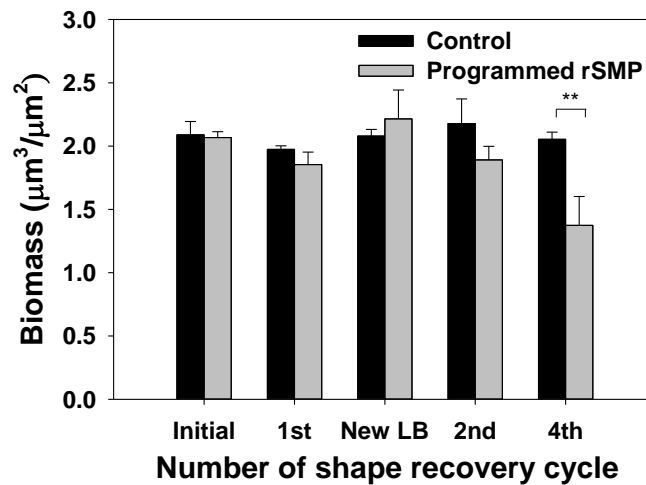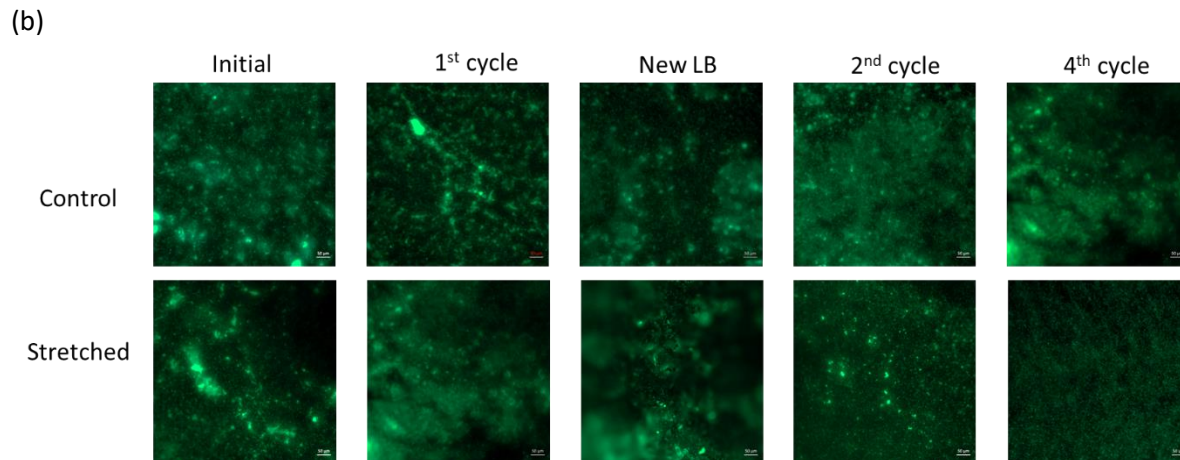
Figure 6.6. Shape recovery behavior and biofilm removal (RT and 40 degree). (a) Biomass after each cycle. After 1st shape recovery, the sample was transferred into new LB media and the biofilm was regrown for 2 days. Then, shape recovery was conducted three more cycles, and biomass was measured after the 1st and 3rd cycle (total 2nd and 4th cycle). (b) Representative images of biofilms. **p < 0.01.

6.4.5 Biofilm removal sensitized detached cells to tobramycin

In Chapter 5, we have demonstrated that the shape recovery can sensitize the biofilm cells to antibiotics and increase the intracellular level of ATP [35]. To understand if the rSMP has similar effects, we tested the susceptibility of cells detached by shape recovery and bead beater (control) to tobramycin. As shown in Figure 6.7, the detached biofilm cells by shape recovery were 0.7 ± 0.1 log (5.0 ± 1.2 times) more susceptible to the 50 µg/mL tobramycin than the control (p=0.004, t-test). Thus, reversible shape recovery by the newly synthesized rSMP also can sensitize the biofilm cells to the tobramycin which implies a potential use for combinational therapy, a physical detachment with antibiotic treatment.

148

50 μg/mL tobramycin
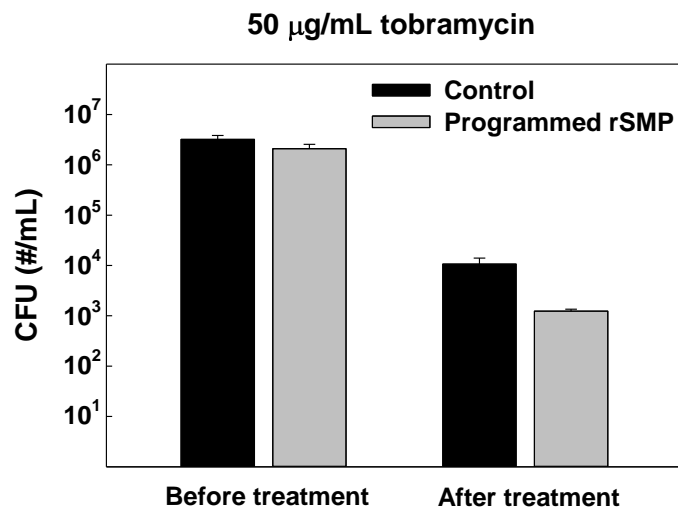
Figure 6.7. Sequential treatment of *P. aeruginosa* PAO1 biofilm cells. Tobramycin at 50 µg/mL was tested by adding to the biofilm cells dispersed after the 3rd shape recovery cycle. The biofilm cells of static flat control were detached by bead beating. The biofilm cells released by shape recovery were also processed with bead beating to avoid any confounding effects. **p < 0.01.

6.5 Discussion

Biofilm control strategies to date are largely limited to the direct killing of biofilm cells and the prevention of biofilm formation[43–55] [7,8,13–25,56–70]. With the activities of conventional antibiotics limiting, it is important to develop new methods to remove mature biofilms and/or sensitize biofilm cells to antibiotics.

In Chapter 4, we have developed on-demand biofilm control using a dynamic topographic stratum of SMP and obtained up to 99.9% removal of 48 h mature *P. aeruginosa* PAO1 biofilms[34]. In addition, we demonstrated that the dynamic deformation of the substrate can sensitize the detached biofilm cells to antibiotics possibly due to elevated levels of intracellular ATP, which showed a potential for combinational therapy in biomedical applications in Chapter 5 [35]. In this study, to overcome the limitation of one-way SMP that cannot be reactivated repeatedly over time, we synthesized a caprolactone-based SMP with the capability of reversible shape recovery. It has 3 cycles of 98.9±1.2% (average) shape recovery percentage of between room temperature and 40°C. The removal of 48 h *P. aeruginosa* PAO1 biofilm was 21.6±1.7% after 3 consecutive cycles and the reliability of the reproduction for biofilm removal via shape recovery (32.8±7.2%) was also demonstrated. Moreover, a synergy effect between an antibiotic treatment and biofilm removal was demonstrated showing 5.0±1.2 times more susceptible to 50 µg/mL tobramycin compared to the control biofilm cells.

Several stimuli have been shown to trigger shape change including heat [37,71–75], light [76–78], solvent [79–81], electricity [82–84], microwave [85–87], ultrasound [88–90], etc. Due to a need for additional equipment, feasibility, and safety, however, the heat stimulus has been highlighted the most in biomedical applications. In the present study, the newly synthesized rSMP is a chemically crosslinked semi-crystalline polymer with a heat-responsive property [37].

Functional groups, methacrylate groups, from two different molecular weights of PCLDIMAs were crosslinked together by a crosslinker, BA at 90°C. The reversible shape memory effect requires a wide range of melting temperature [91]. The two segments of the rSMP had two different melting temperatures (one with a high melting temperature and the other with a low melting temperature) before they were crosslinked, and this created a wide range of melting temperature after the copolymerization. Within the wide melting temperature range, two elements coexisted as a "shifting-geometry determining segment" (an element with a higher melting temperature) and an "actuator segment" (an element with a lower melting temperature). After programming the rSMP, the stretched sample shrunk at high temperature when the crystalline phase of the "actuator segment" is partially melted which leads to the increase of contraction force. The sample was contracted to the intermediate deformation until the contraction force and an internal tensile force are balanced. At a low temperature, on the other hand, the internal tensile force becomes dominant and this results in a further elongation of the rSMP. By using the same principle of reversible shape recovery effect, other materials of copolymers with different melting temperature range were synthesized [73,74,92–96] and be tested for future antifouling materials.

  The application of SMPs in the biomedical field has been limited to self-tightening sutures [97–99], self-expansion stents [100], drug delivery carriers [101–103], and artificial bandages [104] based on the property of one-way shape recovery effect. Though there are reversible SMPs, it is difficult to apply two stimuli to the inside of patients. Although the triggering temperatures need to be further optimized, the results from this study proved the feasibility to obtain repeated actuation and biofilm removal. By coating the internal surface of tubes and fabricating internal parts of the devices with a rSMP material, clusters of the biofilm cells can be

removed/detached via self-cleaning ability which does not need the replacement or disassemble of the biomedical devices.

It is unknown if the repeated shape recovery will cause any other changes such as the roughness and topography of the surface. This is part of our ongoing study. It will also be helpful to study how bacteria attach to surfaces that have gone through shape recovery. This will provide important information to evaluate the potential of this technology for long-term biofilm control.

6.6 Conclusion

In summary, this study demonstrated dynamic changes in topography via shape recovery to detach mature biofilm from the surfaces. The newly synthesized rSMP consists of 2,000 g/mol and 15,000 g/mol PCLDIMA with a ratio of 2:1, 25 wt.% BA as a crosslinker, and 1 wt.% BPO as a thermal initiator. The shape memory effect of the rSMP can be repeated up to 3 cycles with reliable reproducibility. The mature 48 h *P. aeruginosa* PAO1 biofilm cells were significantly removed by up to 94.3±1.0% after three cycles of consecutive shape recovery. The dynamic changes of substratum also can sensitize the detached biofilm cells to 50 µg/mL tobramycin by 5.0±1.2 times more than the biofilm cells from the static control. Reversible shape recovery has the potential for long-term biofilm control in medical and industrial applications.

6.7 References

[1]   H.C. Flemming, J. Wingender, The biofilm matrix, Nat. Rev. Microbiol. 8 (2010) 623–

        633. https://doi.org/10.1038/nrmicro2415.

[2]   L. Hall-Stoodley, J.W. Costerton, P. Stoodley, Bacterial biofilms: From the natural

        environment to infectious diseases, Nat. Rev. Microbiol. 2 (2004) 95–108.

        https://doi.org/10.1038/nrmicro821.

[3]   T. Bjarnsholt, O. Ciofu, S. Molin, M. Givskov, N. Høiby, Applying insights from biofilm

        biology to drug development-can a new approach be developed?, Nat. Rev. Drug Discov.

        12 (2013) 791–808. https://doi.org/10.1038/nrd4000.

[4]   I. Olsen, Biofilm-specific antibiotic tolerance and resistance, Eur. J. Clin. Microbiol.

        Infect. Dis. 34 (2015) 877–886. https://doi.org/10.1007/s10096-015-2323-z.

[5]   C.W. Hall, T.-F. Mah, Molecular mechanisms of biofilm-based antibiotic resistance and

        tolerance in pathogenic bacteria, FEMS Microbiol. Rev. 41 (2017) 276–301.

        https://doi.org/10.1093/femsre/fux010.

[6]   Centers for Disease Control and Prevention (CDC), Data Summary of HAIs in the US:

        Assessing Progress 2006-2016, (2017). https://www.cdc.gov/hai/data/archive/data-

        summary-assessing-progress.html.

[7]   W.H. Kim, S.B. Lee, K.T. Oh, S.K. Moon, K.M. Kim, K.N. Kim, The release behavior of

        CHX from polymer-coated titanium surfaces, Surf. Interface Anal. 40 (2008) 202–204.

        https://doi.org/10.1002/sia.2809.

[8]   A. Ewald, S.K. Glückermann, R. Thull, U. Gbureck, D. Lew, Antimicrobial

titanium/silver PVD coatings on titanium, Biomed. Eng. Online. 5 (2006) 22. https://doi.org/10.1186/1475-925X-5-22.

[9]   L. Zhao, P.K. Chu, Y. Zhang, Z. Wu, Antibacterial coatings on titanium implants, J. Biomed. Mater. Res. - Part B Appl. Biomater. 91 (2009) 470–480. https://doi.org/10.1002/jbm.b.31463.

[10]   A. Meza-Villezcas, A.L. Gallego-Hernández, F.H. Yildiz, O.E. Jaime-Acuña, O. Raymond-Herrera, A. Huerta-Saquero, Effect of antimicrobial nanocomposites on Vibrio cholerae lifestyles: Pellicle biofilm, planktonic and surface-attached biofilm, PLoS One. 14 (2019) 1–18. https://doi.org/10.1371/journal.pone.0217869.

[11]   E. Piacenza, A. Presentato, E. Zonaro, J.A. Lemire, M. Demeter, G. Vallini, R.J. Turner, S. Lampis, Antimicrobial activity of biogenically produced spherical Se-nanomaterials embedded in organic material against Pseudomonas aeruginosa and Staphylococcus aureus strains on hydroxyapatite-coated surfaces, Microb. Biotechnol. 10 (2017) 804–818. https://doi.org/10.1111/1751-7915.12700.

[12]   J. Redfern, L. Geerts, J.W. Seo, J. Verran, L. Tosheva, L.H. Wee, Toxicity and Antimicrobial Properties of ZnO@ZIF-8 Embedded Silicone against Planktonic and Biofilm Catheter-Associated Pathogens, ACS Appl. Nano Mater. 1 (2018) 1657–1665. https://doi.org/10.1021/acsanm.8b00140.

[13]   D. Campoccia, L. Montanaro, C.R. Arciola, A review of the biomaterials technologies for infection-resistant surfaces, Biomaterials. 34 (2013) 8533–8554. https://doi.org/10.1016/j.biomaterials.2013.07.089.

[14]   F. Mabboux, L. Ponsonnet, J.J. Morrier, N. Jaffrezic, O. Barsotti, Surface free energy and

bacterial retention to saliva-coated dental implant materials - An in vitro study, Colloids Surfaces B Biointerfaces. 39 (2004) 199–205. https://doi.org/10.1016/j.colsurfb.2004.08.002.

[15]   E. Fadeeva, V.K. Truong, M. Stiesch, B.N. Chichkov, R.J. Crawford, J. Wang, E.P. Ivanova, Bacterial retention on superhydrophobic titanium surfaces fabricated by femtosecond laser ablation, Langmuir. 27 (2011) 3012–3019. https://doi.org/10.1021/la104607g.

[16]   X. Zhang, L. Wang, E. Levänen, Superhydrophobic surfaces for the reduction of bacterial adhesion, RSC Adv. 3 (2013) 12003. https://doi.org/10.1039/c3ra40497h.

[17]   J. Ma, Y. Sun, K. Gleichauf, J. Lou, Q. Li, Nanostructure on taro leaves resists fouling by colloids and bacteria under submerged conditions, Langmuir. 27 (2011) 10035–10040. https://doi.org/10.1021/la2010024.

[18]   F. Song, H. Wang, K. Sauer, D. Ren, Cyclic-di-GMP and oprF are involved in the response of Pseudomonas aeruginosa to substrate material stiffness during attachment on polydimethylsiloxane (PDMS), Front. Microbiol. 9 (2018) 1–13. https://doi.org/10.3389/fmicb.2018.00110.

[19]   F. Song, M.E. Brasch, H. Wang, J.H. Henderson, K. Sauer, D. Ren, How Bacteria Respond to Material Stiffness during Attachment: A Role of Escherichia coli Flagellar Motility, ACS Appl. Mater. Interfaces. 9 (2017) 22176–22184. https://doi.org/10.1021/acsami.7b04757.

[20]   Y. Zhao, F. Song, H. Wang, J. Zhou, D. Ren, Phagocytosis of Escherichia coli biofilm cells with different aspect ratios: a role of substratum material stiffness, Appl. Microbiol.

Biotechnol. 101 (2017) 6473–6481. https://doi.org/10.1007/s00253-017-8394-2.

[21]   F. Song, D. Ren, Stiffness of cross-linked poly(dimethylsiloxane) affects bacterial adhesion and antibiotic susceptibility of attached cells, Langmuir. 30 (2014) 10354–10362. https://doi.org/10.1021/la502029f.

[22]   H. Gu, A. Chen, X. Song, M.E. Brasch, J.H. Henderson, D. Ren, How Escherichia coli lands and forms cell clusters on a surface: A new role of surface topography, Sci. Rep. 6 (2016) 1–14. https://doi.org/10.1038/srep29516.

[23]   H. Gu, D. Ren, Materials and surface engineering to control bacterial adhesion and biofilm formation: A review of recent advances, Front. Chem. Sci. Eng. 8 (2014) 20–33. https://doi.org/10.1007/s11705-014-1412-3.

[24]   H. Gu, K.W. Kolewe, D. Ren, Conjugation in Escherichia coli Biofilms on Poly(dimethylsiloxane) Surfaces with Microtopographic Patterns, Langmuir. 33 (2017) 3142–3150. https://doi.org/10.1021/acs.langmuir.6b04679.

[25]   M.N. Dickson, E.I. Liang, L.A. Rodriguez, N. Vollereaux, A.F. Yee, Nanopatterned polymer surfaces with bactericidal properties, Biointerphases. 10 (2015) 021010. https://doi.org/10.1116/1.4922157.

[26]   K.K. Chung, J.F. Schumacher, E.M. Sampson, R.A. Burne, P.J. Antonelli, A.B. Brennan, Impact of engineered surface microtopography on biofilm formation of Staphylococcus aureus , Biointerphases. 2 (2007) 89–94. https://doi.org/10.1116/1.2751405.

[27]   H. Koo, R.N. Allan, R.P. Howlin, P. Stoodley, L. Hall-Stoodley, Targeting microbial biofilms: Current and prospective therapeutic strategies, Nat. Rev. Microbiol. 15 (2017)

740–755. https://doi.org/10.1038/nrmicro.2017.99.

[28] M. Stigter, J. Bezemer, K. De Groot, P. Layrolle, Incorporation of different antibiotics into carbonated hydroxyapatite coatings on titanium implants, release and antibiotic efficacy, J. Control. Release. 99 (2004) 127–137. https://doi.org/10.1016/j.jconrel.2004.06.011.

[29] A.K. Epstein, D. Hong, P. Kim, J. Aizenberg, Biofilm attachment reduction on bioinspired, dynamic, micro-wrinkling surfaces, New J. Phys. 15 (2013). https://doi.org/10.1088/1367-2630/15/9/095018.

[30] P. Shivapooja, Q. Wang, L.M. Szott, B. Orihuela, D. Rittschof, X. Zhao, G.P. López, Dynamic surface deformation of silicone elastomers for management of marine biofouling: laboratory and field studies using pneumatic actuation, Biofouling. 31 (2015) 265–274. https://doi.org/10.1080/08927014.2015.1035651.

[31] P. Shivapooja, Q. Wang, B. Orihuela, D. Rittschof, G.P. Lõpez, X. Zhao, Bioinspired surfaces with dynamic topography for active control of biofouling, Adv. Mater. 25 (2013) 1430–1434. https://doi.org/10.1002/adma.201203374.

[32] H. Gu, S.W. Lee, J. Carnicelli, T. Zhang, D. Ren, Magnetically driven active topography for long-term biofilm control, Nat. Commun. 11 (2020) 2211. https://doi.org/10.1038/s41467-020-16055-5.

[33] V. Leveri, Q. Wang, P. Shivapooja, X. Zhao, G.P. Lõpez, Soft Robotic Concepts in Catheter Design: an On-demand Fouling-release Urinary Catheter, Adv Heal. Mater. 3 (2014) 1588–1596. https://doi.org/10.1002/ana.22528.Toll-like.

[34] H. Gu, S.W. Lee, S.L. Buffington, J.H. Henderson, D. Ren, On-Demand Removal of Bacterial Biofilms via Shape Memory Activation, ACS Appl. Mater. Interfaces. 8 (2016) 21140–21144. https://doi.org/10.1021/acsami.6b06900.

[35] S.W. Lee, H. Gu, J.B. Kilberg, D. Ren, Sensitizing bacterial cells to antibiotics by shape recovery triggered biofilm dispersion, Acta Biomater. 81 (2018) 93–102. https://doi.org/10.1016/j.actbio.2018.09.042.

[36] A. Lendlein, P. Neuenschwander, U.W. Suter, Hydroxy-telechelic copolyesters with well defined sequence structure through ring-opening polymerization, Macromol. Chem. Phys. 201 (2000) 1067–1076. https://doi.org/10.1002/1521-3935(20000701)201:11<1067::AID-MACP1067>3.0.CO;2-Y.

[37] M. Saatchi, M. Behl, U. Nöchel, A. Lendlein, Copolymer networks from oligo (ε -caprolactone) and n -butyl acrylate enable a reversible bidirectional shape-memory effect at human body temperature, Macromol. Rapid Commun. 36 (2015) 880–884. https://doi.org/10.1002/marc.201400729.

[38] B.S. Tseng, W. Zhang, J.J. Harrison, T.P. Quach, J.L. Song, J. Penterman, P.K. Singh, D.L. Chopp, A.I. Packman, M.R. Parsek, The extracellular matrix protects Pseudomonas aeruginosa biofilms by limiting the penetration of tobramycin, Environ. Microbiol. 86 (2013) n/a-n/a. https://doi.org/10.1111/1462-2920.12155.

[39] G. Bertani, Studies on lysogenesis. I. The mode of phage liberation by lysogenic Escherichia coli., J. Bacteriol. 62 (1951) 293–300. https://doi.org/citeulike-article-id:149214.

[40] A. Heydorn, A. Heydorn, A.T. Nielsen, A.T. Nielsen, M. Hentzer, M. Hentzer,

Quantication of biofilm structures by the novel computer program, Image Process. 146 (2000) 2395–2407. https://doi.org/10.1099/00221287-146-10-2395.

[41]   H. Gu, S.W. Lee, J. Carnicelli, Z. Jiang, D. Ren, Antibiotic Susceptibility of Escherichia coli Cells during Early-Stage Biofilm Formation, J. Bacteriol. 201 (2019). https://doi.org/10.1128/JB.00034-19.

[42]   S. Sieuwerts, F.A.M. De Bok, E. Mols, W.M. De Vos, J.E.T. Van Hylckama Vlieg, A simple and fast method for determining colony forming units, Lett. Appl. Microbiol. (2008). https://doi.org/10.1111/j.1472-765X.2008.02417.x.

[43]   N.C. Francis, W. Yao, W.S. Grundfest, Z.D. Taylor, Laser-Generated Shockwaves as a Treatment to Reduce Bacterial Load and Disrupt Biofilm, IEEE Trans. Biomed. Eng. 64 (2017) 882–889. https://doi.org/10.1109/TBME.2016.2581778.

[44]   N. Abramzon, J.C. Joaquin, J. Bray, G. Brelles-Mariño, Biofilm destruction by RF high-pressure cold plasma jet, IEEE Trans. Plasma Sci. 34 (2006) 1304–1309. https://doi.org/10.1109/TPS.2006.877515.

[45]   O.E. Petrova, K. Sauer, Escaping the biofilm in more than one way: Desorption, detachment or dispersion, Curr. Opin. Microbiol. 30 (2016) 67–78. https://doi.org/10.1016/j.mib.2016.01.004.

[46]   H. Mikkelsen, K. Hui, N. Barraud, A. Filloux, The pathogenicity island encoded PvrSR/RcsCB regulatory network controls biofilm formation and dispersal in Pseudomonas aeruginosa PA14, Mol. Microbiol. 89 (2013) 450–463. https://doi.org/10.1111/mmi.12287.

[47] L.O. Mair, A. Nacev, R. Hilaman, P.Y. Stepanov, S. Chowdhury, S. Jafari, J. Hausfeld, A.J. Karlsson, M.E. Shirtliff, B. Shapiro, I.N. Weinberg, Biofilm disruption with rotating microrods enhances antimicrobial efficacy, J. Magn. Magn. Mater. 427 (2017) 81–84. https://doi.org/10.1016/j.jmmm.2016.10.100.

[48] S.A. Crusz, R. Popat, M.T. Rybtke, M. Cámara, M. Givskov, T. Tolker-Nielsen, S.P. Diggle, P. Williams, Bursting the bubble on bacterial biofilms: A flow cell methodology, Biofouling. 28 (2012) 835–842. https://doi.org/10.1080/08927014.2012.716044.

[49] H. Jang, R. Rusconi, R. Stocker, Biofilm disruption by an air bubble reveals heterogeneous age-dependent detachment patterns dictated by initial extracellular matrix distribution, Npj Biofilms Microbiomes. 3 (2017) 0–1. https://doi.org/10.1038/s41522-017-0014-5.

[50] I.B. Gomes, M. Lemos, L. Mathieu, M. Simões, L.C. Simões, The action of chemical and mechanical stresses on single and dual species biofilm removal of drinking water bacteria, Sci. Total Environ. 631–632 (2018) 987–993. https://doi.org/10.1016/j.scitotenv.2018.03.042.

[51] D.P. Gnanadhas, M. Elango, S. Janardhanraj, C.S. Srinandan, A. Datey, R.A. Strugnell, J. Gopalan, D. Chakravortty, Successful treatment of biofilm infections using shock waves combined with antibiotic therapy, Sci. Rep. 5 (2015) 1–13. https://doi.org/10.1038/srep17440.

[52] N. Dror, M. Mandel, Z. Hazan, G. Lavie, Advances in Microbial Biofilm Prevention on Indwelling Medical Devices with Emphasis on Usage of Acoustic Energy, Sensors. 9 (2009) 2538–2554. https://doi.org/10.3390/s90402538.

[53] Y. Li, S. Heine, M. Entian, K. Sauer, N. Frankenberg-Dinkel, NO-induced biofilm dispersion in Pseudomonas aeruginosa is mediated by an MHYT domain-coupled phosphodiesterase, J. Bacteriol. 195 (2013) 3531–3542. https://doi.org/10.1128/JB.01156-12.

[54] O.E. Petrova, K.E. Cherny, K. Sauer, The diguanylate cyclase GcbA facilitates pseudomonas aeruginosa biofilm dispersion by activating BdlA, J. Bacteriol. 197 (2015) 174–187. https://doi.org/10.1128/JB.02244-14.

[55] A. Basu Roy, K. Sauer, Diguanylate cyclase NicD-based signalling mechanism of nutrient-induced dispersion by Pseudomonas aeruginosa, Mol. Microbiol. 94 (2014) 771–793. https://doi.org/10.1111/mmi.12802.

[56] D. Perera-Costa, J.M. Bruque, M.L. González-Martín, A.C. Gómez-García, V. Vadillo-Rodríguez, Studying the influence of surface topography on bacterial adhesion using spatially organized microtopographic surface patterns, Langmuir. 30 (2014) 4633–4641. https://doi.org/10.1021/la5001057.

[57] D. Siegismund, A. Undisz, S. Germerodt, S. Schuster, M. Rettenmayr, Quantification of the interaction between biomaterial surfaces and bacteria by 3-D modeling, Acta Biomater. 10 (2014) 267–275. https://doi.org/10.1016/j.actbio.2013.09.016.

[58] H. Yan Lin, Y. Liu, D. Wismeijer, W. Crielaard, D. Mei Deng, Effects of Oral Implant Surface Roughness on Bacterial Biofilm Formation and Treatment Efficacy, Int. J. Oral Maxillofac. Implants. 28 (2013) 1226–1231. https://doi.org/10.11607/jomi.3099.

[59] A.I. Hochbaum, J. Aizenberg, Bacteria pattern spontaneously on periodic nanostructure arrays, Nano Lett. 10 (2010) 3717–3721. https://doi.org/10.1021/nl102290k.

[60]   A. Ionescu, E. Wutscher, E. Brambilla, S. Schneider-Feyrer, F.J. Giessibl, S. Hahnel,
Influence of surface properties of resin-based composites on in vitro Streptococcus mutans
biofilm development, Eur. J. Oral Sci. 120 (2012) 458–465.
https://doi.org/10.1111/j.1600-0722.2012.00983.x.

[61]   R. Xing, S.P. Lyngstadaas, J.E. Ellingsen, S. Taxt-Lamolle, H.J. Haugen, The influence of
surface nanoroughness, texture and chemistry of TiZr implant abutment on oral biofilm
accumulation, Clin. Oral Implants Res. 26 (2015) 649–656.
https://doi.org/10.1111/clr.12354.

[62]   P. Ball, Shark skin and other solutions, Nat. Eng. 400 (1999) 507–508.
https://doi.org/10.1038/22883.

[63]   K. Anselme, P. Davidson, A.M. Popa, M. Giazzon, M. Liley, L. Ploux, The interaction of
cells and bacteria with surfaces structured at the nanometre scale, Acta Biomater. 6 (2010)
3824–3846. https://doi.org/10.1016/j.actbio.2010.04.001.

[64]   J.S. Price, A.F. Tencer, D.M. Arm, G.A. Bohach, Controlled release of antibiotics from
coated orthopedic implants, J. Biomed. Mater. Res. 30 (1996) 281–286.
https://doi.org/10.1002/(SICI)1097-4636(199603)30:3<281::AID-JBM2>3.0.CO;2-M.

[65]   J. Hasan, R.J. Crawford, E.P. Ivanova, Antibacterial surfaces: The quest for a new
generation of biomaterials, Trends Biotechnol. 31 (2013) 295–304.
https://doi.org/10.1016/j.tibtech.2013.01.017.

[66]   K.C. Popat, M. Eltgroth, T.J. LaTempa, C.A. Grimes, T.A. Desai, Decreased
Staphylococcus epidermis adhesion and increased osteoblast functionality on antibiotic-
loaded titania nanotubes, Biomaterials. 28 (2007) 4880–4888.

https://doi.org/10.1016/j.biomaterials.2007.07.037.

[67] A.D. Russell, W.B. Hugo, Antimicrobial Activity and Action of Silver, Prog. Med. Chem. 31 (1994) 351–370. https://doi.org/10.1016/S0079-6468(08)70024-9.

[68] J.R. Chambers, K.E. Cherny, K. Sauer, Susceptibility of Pseudomonas aeruginosa dispersed cells to antimicrobial agents is dependent on the dispersion cue and class of the antimicrobial agent used, Antimicrob. Agents Chemother. 61 (2017) 1–18. https://doi.org/10.1128/AAC.00846-17.

[69] E.B.H. Hume, J. Baveja, B. Muir, T.L. Schubert, N. Kumar, S. Kjelleberg, H.J. Griesser, H. Thissen, R. Read, L.A. Poole-Warren, K. Schindhelm, M.D.P. Willcox, The control of Staphylococcus epidermidis biofilm formation and in vivo infection rates by covalently bound furanones, Biomaterials. 25 (2004) 5023–5030. https://doi.org/10.1016/j.biomaterials.2004.01.048.

[70] L. Zhao, P.K. Chu, Y. Zhang, Z. Wu, Antibacterial coatings on titanium implants, J. Biomed. Mater. Res. - Part B Appl. Biomater. 91 (2009) 470–480. https://doi.org/10.1002/jbm.b.31463.

[71] T.H. Kang, J.M. Lee, W.R. Yu, J.H. Youk, H.W. Ryu, Two-way actuation behavior of shape memory polymer/elastomer core/shell composites, Smart Mater. Struct. 21 (2012). https://doi.org/10.1088/0964-1726/21/3/035028.

[72] M. Taya, Y. Liang, O.C. Namli, H. Tamagawa, T. Howie, Design of two-way reversible bending actuator based on a shape memory alloy/shape memory polymer composite, Smart Mater. Struct. 22 (2013). https://doi.org/10.1088/0964-1726/22/10/105003.

[73] M. Behl, K. Kratz, J. Zotzmann, U. Nöchel, A. Lendlein, Reversible bidirectional shape-memory polymers, Adv. Mater. 25 (2013) 4466–4469. https://doi.org/10.1002/adma.201300880.

[74] J. Zotzmann, M. Behl, D. Hofmann, A. Lendlein, Reversible triple-shape effect of polymer networks containing polypentadecalactone- and poly(ε-caprolactone)-segments, Adv. Mater. 22 (2010) 3424–3429. https://doi.org/10.1002/adma.200904202.

[75] S. Imai, K. Sakurai, An actuator of two-way behavior by using two kinds of shape memory polymers with different Tgs, Precis. Eng. 37 (2013) 572–579. https://doi.org/10.1016/j.precisioneng.2013.01.002.

[76] K.M. Lee, H. Koerner, R.A. Vaia, T.J. Bunning, T.J. White, Light-activated shape memory of glassy, azobenzene liquid crystalline polymer networks, Soft Matter. 7 (2011) 4318. https://doi.org/10.1039/c1sm00004g.

[77] L. Wu, C. Jin, X. Sun, Synthesis, properties, and light-induced shape memory effect of multiblock polyesterurethanes containing biodegradable segments and pendant cinnamamide groups, Biomacromolecules. 12 (2011) 235–241. https://doi.org/10.1021/bm1012162.

[78] A. Lendlein, H. Jiang, O. Jünger, R. Langer, Light-induced shape-memory polymers, Nature. 434 (2005) 879–882. https://doi.org/10.1038/nature03496.

[79] X. Gu, P.T. Mather, Water-triggered shape memory of multiblock thermoplastic polyurethanes (TPUs), RSC Adv. 3 (2013) 15783–15791. https://doi.org/10.1039/c3ra41337c.

[80] T. Wu, M. Frydrych, K. O'Kelly, B. Chen, Poly(glycerol sebacate urethane)-cellulose nanocomposites with water-active shape-memory effects, Biomacromolecules. 15 (2014) 2663–2671. https://doi.org/10.1021/bm500507z.

[81] D. Quitmann, N. Gushterov, G. Sadowski, F. Katzenberg, J.C. Tiller, Solvent-sensitive reversible stress-response of shape memory natural rubber, ACS Appl. Mater. Interfaces. 5 (2013) 3504–3507. https://doi.org/10.1021/am400660f.

[82] J.W. Cho, J.W. Kim, Y.C. Jung, N.S. Goo, Electroactive shape-memory polyurethane composites incorporating carbon nanotubes, Macromol. Rapid Commun. 26 (2005) 412–416. https://doi.org/10.1002/marc.200400492.

[83] Y. Xiao, S. Zhou, L. Wang, T. Gong, Electro-active shape memory properties of poly(ε-caprolactone)/ functionalized multiwalled carbon nanotube nanocomposite, ACS Appl. Mater. Interfaces. 2 (2010) 3506–3514. https://doi.org/10.1021/am100692n.

[84] J. Zhou, H. Li, W. Liu, R. Dugnani, R. Tian, W. Xue, Y. Chen, Y. Guo, H. Duan, H. Liu, A facile method to fabricate polyurethane based graphene foams/epoxy/carbon nanotubes composite for electro-active shape memory application, Compos. Part A Appl. Sci. Manuf. 91 (2016) 292–300. https://doi.org/10.1016/j.compositesa.2016.10.021.

[85] H. Kalita, N. Karak, Hyperbranched polyurethane/Fe3O4 nanoparticles decorated multiwalled carbon nanotube thermosetting nanocomposites as microwave actuated shape memory materials, J. Mater. Res. 28 (2013) 2132–2141. https://doi.org/10.1557/jmr.2013.213.

[86] H. Du, Y. Yu, G. Jiang, J. Zhang, J. Bao, Microwave-induced shape-memory effect of chemically crosslinked moist poly(vinyl alcohol) networks, Macromol. Chem. Phys. 212

(2011) 1460–1468. https://doi.org/10.1002/macp.201100149.

[87]   H. Du, X. Liu, Y. Yu, Y. Xu, Y. Wang, Z. Liang, Microwave-Induced Poly(ionic liquid)/Poly(vinyl alcohol) Shape Memory Composites, Macromol. Chem. Phys. 217 (2016) 2626–2634. https://doi.org/10.1002/macp.201600379.

[88]   G. Li, G. Fei, B. Liu, H. Xia, Y. Zhao, Shape recovery characteristics for shape memory polymers subjected to high intensity focused ultrasound, RSC Adv. 4 (2014) 32701– 32709. https://doi.org/10.1039/c4ra04586f.

[89]   M. Bao, Q. Zhou, W. Dong, X. Lou, Y. Zhang, Ultrasound-modulated shape memory and payload release effects in a biodegradable cylindrical rod made of chitosan-functionalized PLGA microspheres, Biomacromolecules. 14 (2013) 1971–1979. https://doi.org/10.1021/bm4003464.

[90]   J. Han, G. Fei, G. Li, H. Xia, High intensity focused ultrasound triggered shape memory and drug release from biodegradable polyurethane, Macromol. Chem. Phys. 214 (2013) 1195–1203. https://doi.org/10.1002/macp.201200576.

[91]   K. Wang, Y.G. Jia, C. Zhao, X.X. Zhu, Multiple and two-way reversible shape memory polymers: Design strategies and applications, Prog. Mater. Sci. 105 (2019) 100572. https://doi.org/10.1016/j.pmatsci.2019.100572.

[92]   T. Gong, K. Zhao, W. Wang, H. Chen, L. Wang, S. Zhou, Thermally activated reversible shape switch of polymer particles, J. Mater. Chem. B. 2 (2014) 6855–6866. https://doi.org/10.1039/c4tb01155d.

[93]   C. Qian, Y. Dong, Y. Zhu, Y. Fu, Two-way shape memory behavior of semi-crystalline

elastomer under stress-free condition, Smart Mater. Struct. 25 (2016). https://doi.org/10.1088/0964-1726/25/8/085023.

[94]   O. Dolynchuk, I. Kolesov, D. Jehnichen, U. Reuter, H.J. Radusch, J.U. Sommer, Reversible Shape-Memory Effect in Cross-Linked Linear Poly(ϵ-caprolactone) under Stress and Stress-Free Conditions, Macromolecules. 50 (2017) 3841–3854. https://doi.org/10.1021/acs.macromol.7b00481.

[95]   J. Zhou, S.A. Turner, S.M. Brosnan, Q. Li, J.M.Y. Carrillo, D. Nykypanchuk, O. Gang, V.S. Ashby, A. V. Dobrynin, S.S. Sheiko, Shapeshifting: Reversible shape memory in semicrystalline elastomers, Macromolecules. 47 (2014) 1768–1776. https://doi.org/10.1021/ma4023185.

[96]   Q. Li, J. Zhou, M. Vatankhah-Varnoosfaderani, D. Nykypanchuk, O. Gang, S.S. Sheiko, Advancing Reversible Shape Memory by Tuning the Polymer Network Architecture, Macromolecules. 49 (2016) 1383–1391. https://doi.org/10.1021/acs.macromol.5b02740.

[97]   A. Lendlein, R. Langer, Biodegradable, elastic shape-memory polymers for potential biomedical applications, Science (80-.). 296 (2002) 1673–1676. https://doi.org/10.1126/science.1066102.

[98]   X. Jing, H.-Y. Mi, H.-X. Huang, L.-S. Turng, Shape memory thermoplastic polyurethane (TPU)/poly(ϵ-caprolactone) (PCL) blends as self-knotting sutures, J. Mech. Behav. Biomed. Mater. 64 (2016) 94–103. https://doi.org/10.1016/j.jmbbm.2016.07.023.

[99]   A. Biswas, A.P. Singh, D. Rana, V.K. Aswal, P. Maiti, Biodegradable toughened nanohybrid shape memory polymer for smart biomedical applications, Nanoscale. 10 (2018) 9917–9934. https://doi.org/10.1039/C8NR01438H.

[100] M.C. Chen, H.W. Tsai, Y. Chang, W.Y. Lai, F.L. Mi, C.T. Liu, H.S. Wong, H.W. Sung, Rapidly self-expandable polymeric stents with a shape-memory property, Biomacromolecules. 8 (2007) 2774–2780. https://doi.org/10.1021/bm7004615.

[101] M.C. Serrano, L. Carbajal, G.A. Ameer, Novel Biodegradable Shape-Memory Elastomers with Drug-Releasing Capabilities, Adv. Mater. 23 (2011) 2211–2215. https://doi.org/10.1002/adma.201004566.

[102] M. Kashif, B. Yun, K.-S. Lee, Y.-W. Chang, Biodegradable shape-memory poly(ε-caprolactone)/polyhedral oligomeric silsequioxane nanocomposites: sustained drug release and hydrolytic degradation, Mater. Lett. 166 (2016) 125–128. https://doi.org/10.1016/j.matlet.2015.12.051.

[103] H. Chen, Y. Li, Y. Liu, T. Gong, L. Wang, S. Zhou, Highly pH-sensitive polyurethane exhibiting shape memory and drug release, Polym. Chem. 5 (2014) 5168–5174. https://doi.org/10.1039/C4PY00474D.

[104] M. Hasnat Kabir, T. Hazama, Y. Watanabe, J. Gong, K. Murase, T. Sunada, H. Furukawa, Smart hydrogel with shape memory for biomedical applications, J. Taiwan Inst. Chem. Eng. 45 (2014) 3134–3138. https://doi.org/10.1016/j.jtice.2014.09.035.

Chapter 7

Conclusions and Future work

7.1 Conclusions

Medical device-associated infections have been studied intensively for a long time to lower the infection rates and improve the safety of medical devices. Unfortunately, the presence of antibiotic tolerant biofilms makes it challenging. Various kinds of strategies (surface chemistry, biology, surface property, etc.) have attempted to eradicate biofilms from medical devices. Among these strategies, we have focused on the effects of surface property especially topography. Studies were conducted to investigate the effect of micron to nanoscale topographies that are either synthetic or inspired by nature such as sharkskin, lotus leaf, gecko skin, cicada wings, and others. To engineer biomaterials with antifouling topographies, systems of static, active, and dynamic surface topographies were developed. In this study, I have studied the effects of static and dynamic surface topography on bacterial attachment and biofilm formation using PDMS and shape memory polymer (SMP) biomaterials.

Studying the effects of PDMS static surface topography on bacterial adhesion and biofilm formation was motivated by BIA-ALCL associated with textured breast implants. We developed a high-throughput method to study bacterial attachment PDMS surfaces with systematically varied topographic features. By examining bacterial adhesion on these surfaces, we found that *E. coli*, a Gram-negative strain, prefers to attach to certain features (S10 D5, S10 D2, and S5 D2) than the flat control under static condition. In addition, we observed that *E. coli* prefers to attach to the interfacial junction area rather than the open flat area. Because the area of interfacial junctions can help microorganisms to escape from the host immune system, these surface structures may increase the risk of BIA-ALCL.

To control mature biofilms, we developed one-way SMP to remove/detach mature biofilm from the biomaterials. *tert*-butyl acrylate-based (tBA) SMP can change its surface topography by

a stimulus of 40°C heating for 10 min. This strategy was found effective for the removal of established 48h *P. aeruginosa* PAO1 biofilms by 99.9%. To understand the mechanism of biofilm removal via shape recovery, the physiological changes of detached biofilm cells were studied. The biofilm cells released by shape recovery were up to 9-fold more susceptible to antibiotics than the static flat control in sequential treatments; and more than 3 logs of biofilm reduction was achieved by concurrent treatment (shape recovery in the presence of antibiotics). Consistent with the increase in susceptibility to antibiotics, 11.8 times more ATP production and 4.1 times higher *rrnB* expression levels were observed in biofilm cells dispersed by shape recovery compared to the static flat control. These findings were corroborated by RNA-seq and qPCR results and indicate that shape recovery triggered dispersion rendered bacterial cells to leave the physiological stage of biofilm growth and entered a more active and drug-susceptible stage.

Due to the limitation of one-time use for one-way SMP, the property of reversible shape recovery is needed for long-term biofilm control. The newly synthesized reversible shape memory polymer (rSMP) consists of 2,000 g/mol and 5,000 g/mol poly(ε-caprolactone) diisocyanatoethyl dimethacrylate (PCLDIMA) with a ratio of 2:1, 25 wt.% butyl acrylate (BA) as a crosslinker and 1 wt.% benzoyl peroxide (BPO) as a thermal initiator. The shape memory effect of this rSMP can be repeated up to 3 cycles with good reproducibility. The mature 48 h *P. aeruginosa* PAO1 biofilm cells were removed by up to 94.3±1.1% after three cycles of consecutive shape recovery. The dynamic changes of substratum also sensitized the detached biofilm cells to 50 µg/mL tobramycin by 5.0±1.2 times compared to the biofilm cells from the static control. Further studies are needed to be optimized the shape recovery condition for medical applications, but the results from this study proved this new concept.

7.2 Future work

7.2.1 Effects of surface topography on bacterial virulence

In Chapter 3, we demonstrated that more cells were attached on the textured surfaces especially those with the patterns of S5 D2, S10 D5 & S10 D2 than the flat control. In addition, *E. coli* prefers to attach on the side/corner area of recessive features. We speculate that the change in surface attachment can also affect the production of virulence factors of bacteria. Host immune responses such as macrophages are generally induced by the virulence factors that pathogens produce [1,2]. If the type and amount of virulence factors are altered on specific patterns such as S5 D2, S10 D5, and S10 D2, we would identify important BIA-ALCL risk factors and the possible strategy to mitigate. The RNA-seq analysis or qPCR can demonstrate if and which virulence factor-related genes are upregulated/downregulated in response to surface topography.

7.2.2 Effects of fluid dynamics on textured breast implant devices

To categorize the risk of BIA-ALCL level, *in vivo* condition needs to be considered. Breast implants in the human body are static most of the time but also commonly experience motion. This study focused on static conditions to have a high throughput study of many features, but it does not fully represent the real conditions in patients. To understand the details of *in vivo* conditions, it will be important to conduct a simulation of fluid dynamics on textured breast implants to mimic motion. This analysis will provide further information to categorize the risk of BIA-ALCL.

7.3 References

[1]   S. Sone, H. Tsutsumi, R. Takeuchi, K. Matsuda, S. Lmai, P.L. Ogra, S. Chiba, Enhanced cytokine production by milk macrophages following infection with respiratory syncytial virus, J. Leukoc. Biol. 61 (1997) 630–636. https://doi.org/10.1002/jlb.61.5.630.

[2]   E. Obeid, R. Nanda, Y. Fu, O.I. Olopade, The role of tumor-associated macrophages in breast cancer progression, Int. J. Oncol. 43 (2013) 5–12. https://doi.org/10.3892/ijo.2013.1938.

[3]   A. Farkas, N. Degiuli, I. Martić, Towards the prediction of the effect of biofilm on the ship resistance using CFD, Ocean Eng. 167 (2018) 169–186. https://doi.org/10.1016/j.oceaneng.2018.08.055.

[4]   A.R. Rajabzadeh, R.L. Legge, K.P. Weber, Multiphysics modelling of flow dynamics, biofilm development and wastewater treatment in a subsurface vertical flow constructed wetland mesocosm, Ecol. Eng. 74 (2015) 107–116. https://doi.org/10.1016/j.ecoleng.2014.09.122.

[5]   B. Boulbene, J. Morchain, M.M. Bonin, S. Janel, F. Lafont, P. Schmitz, A combined computational fluid dynamics (CFD) and experimental approach to quantify the adhesion force of bacterial cells attached to a plane surface, AIChE J. 58 (2012) 3614–3624. https://doi.org/10.1002/aic.13747.

Appendices

Appendix A. Fabrication process of recessive PDMS features

1. Design your features using L-edit CAD software
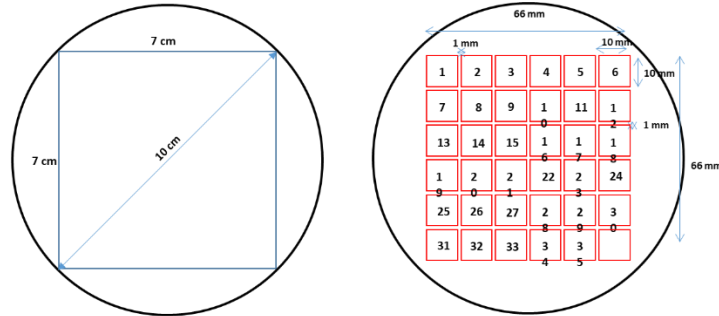
Area	Side (um)	Distance (um)	Area	Side (um)	Distance (um)	Area	Side (um)	Distance (um)	Area	Side (um)	Distance (um)	Area	Side (um)	Distance (um)
1	2	2	8	5	9.8	15	10	108	22	110	5.5	29	190	55
2	2	5	9	4.9	50.2	16	60	2	23	102	15	30	210	94
3	2	10.61	10	5	95	17	55	5	24	100	48	31	300	2
4	1.995	54.502	11	10.2	2	18	50	12	25	100	100	32	310	5.5
5	1.993	90	12	10	5	19	50	50	26	200	2	33	300	10
6	4.9	2	13	10	10	20	50	90	27	200	5	34	300	45
7	5	5	14	9.7	52.8	21	90	2	28	200	9	35	285	196

2. Use mask drawing machine to create patterns on a quartz mask

Expose laser to Cr-quartz
mask based on CAD drawing
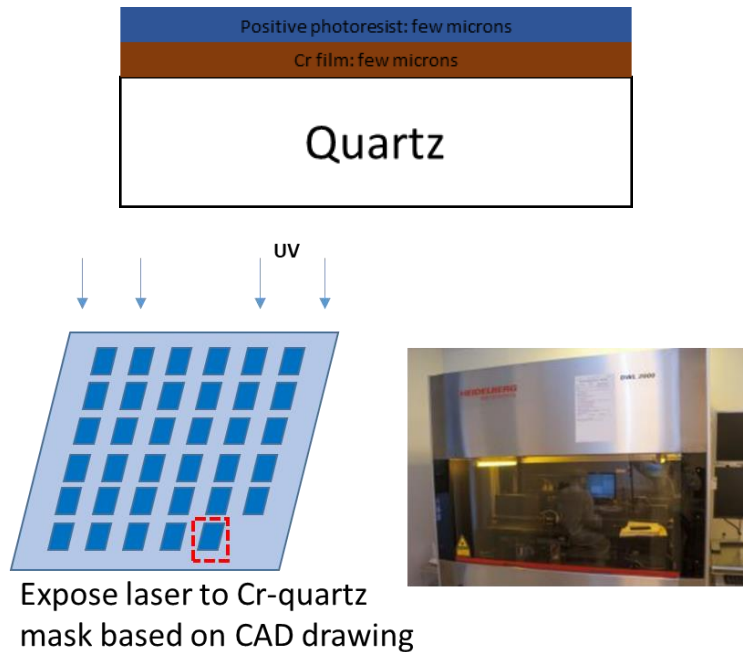
3. Develop photoresist (PR) using 726 MIF TMAH based developing solution

Developer (726 MIF): TMAH based solution

Developing process
(develop PR)

10 mm

10 mm
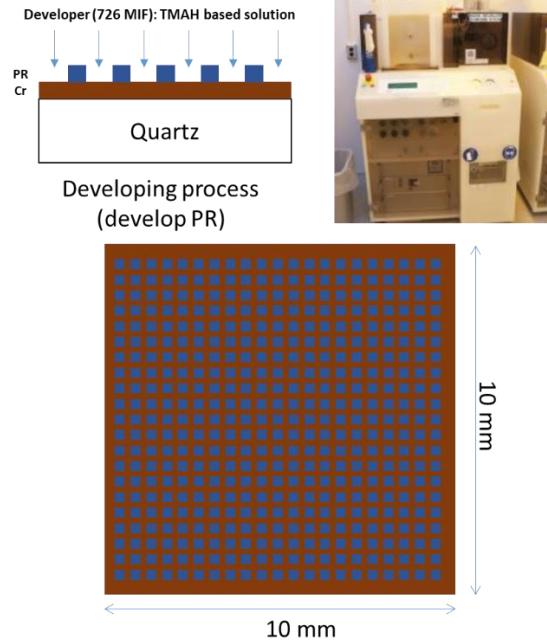
4. Etch Cr layer using a ceric ammonium nitrate-based etchant (Cyantek CR-14)

Etchant (Cyantek CR-14): Ceric ammonium nitrate based solution

Developing process
(Etch Cr)

10 mm

10 mm
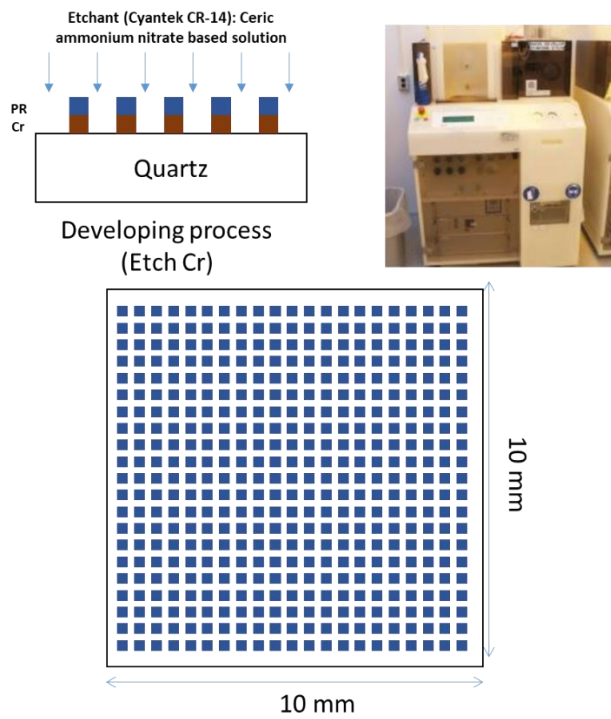
5. Strip rest of PR from the quartz mask

Stripping agent: NMP and TMAH based solution at 80 degree

Cr

Quartz

Stripping process
(strip PR only)

10 mm

10 mm
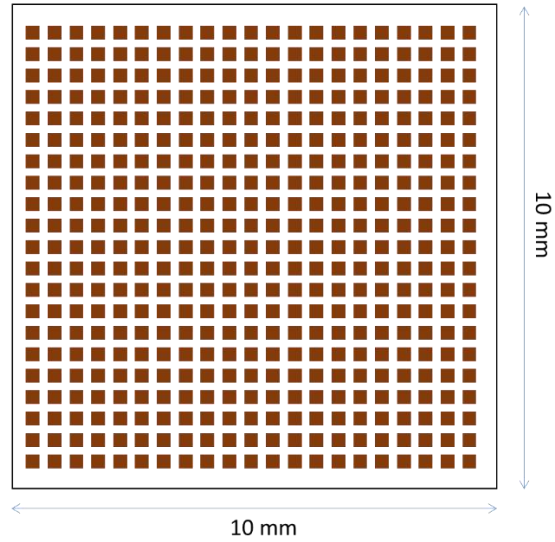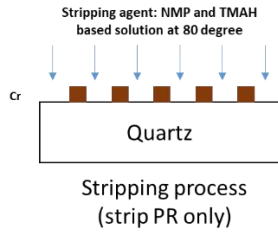
6. Spin coat a silicon wafer with P20 (adhesion layer) and PR (S1813)

Positive photoresist (S1813 or S1818): 1.8 um - 2.5 um
P20 (adhesive agent): 30-50 nm
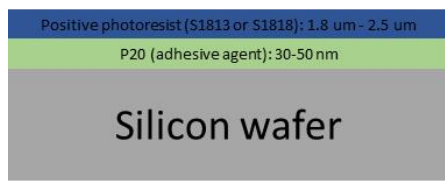
Silicon wafer

Spin coating process
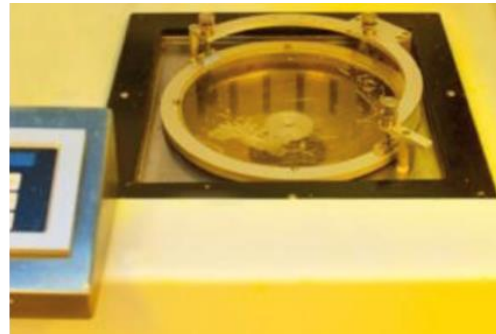
7. Use a 1:1 photolithography (Contact aligner) to create patterns on the silicon wafer

UV

Cr mask

PR
P20

Si
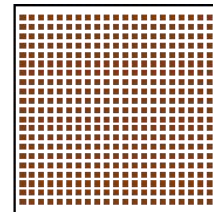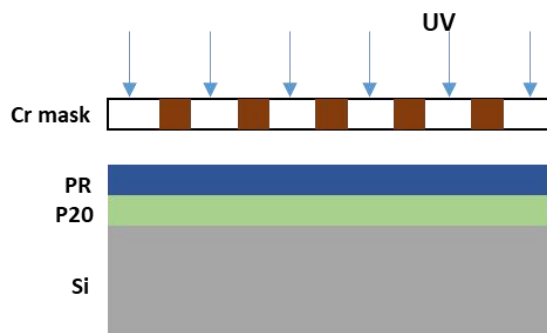
1:1 photolithography process
(contact mode)

8. Develop P20 and PR layers in a hot TMAH-based bath
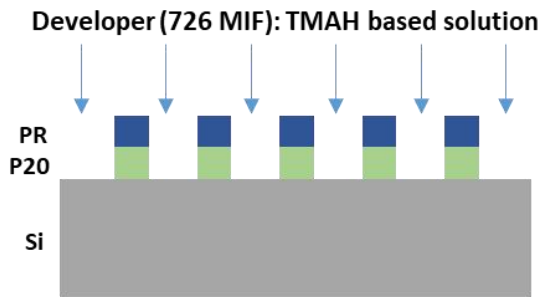
9. Etch the silicon wafer using deep reactive ion etcher (DRIE)
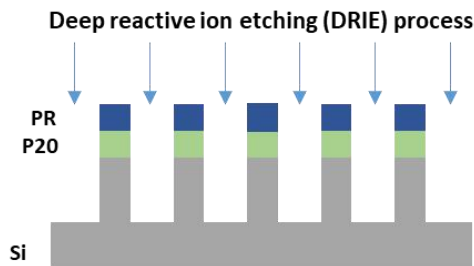
10. Strip rest of PR and P20 layers using stripper
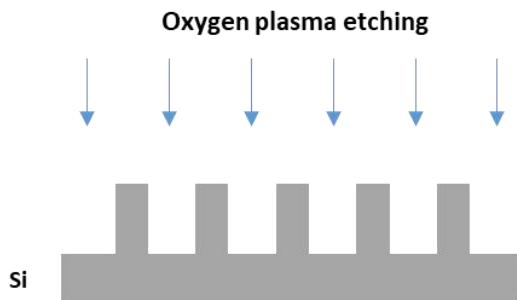
11. Deposit fluorooctyltrichlorosilane (FOTS) on the silicon wafer to make the surface hydrophobic

Fluorooctyltrichlorosilane (FOTS)

Si

Molecular vapor deposition (MVD) process
(hydrophobic surface)
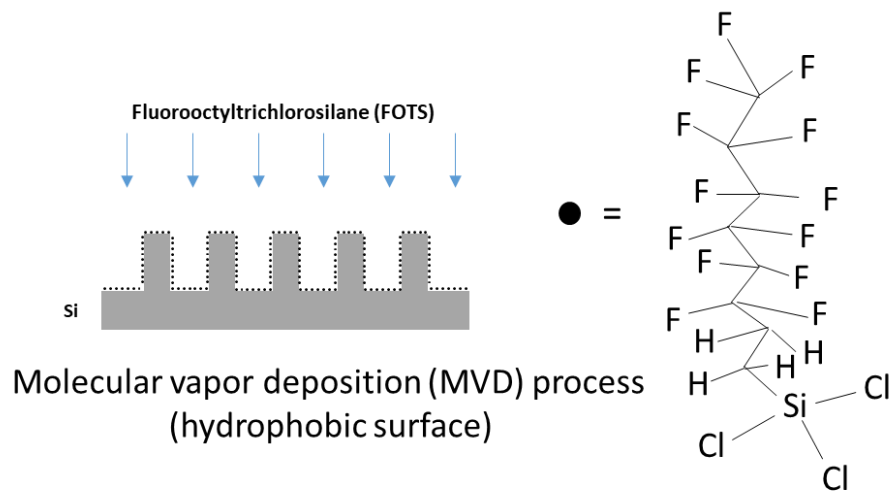
Appendix B. A synthesis of reversible shape memory polymer (rSMP)

1. Oligo(ε-caprolactone) diol (OCL)

    (1) Add ε-caprolactone: ethylene glycol 100: 1 weight ratio and 5 wt.% dibutyltin oxide (catalyst) into a round bottom flask

    (2) Set temperature at 130°C and react for 5 hr

    (3) Use a balloon to keep N_2 environment inside of a flask

    (4) Turn off the hot plate after 5 hr and wait until it cools down

    (5) Dissolve the catalyst in 1,2-dichloroethane and purify the OCL over silica gel

    (6) Use hexane fraction to purify OCL if needed

2. Poly(ε-caprolactone) diisocyanatoethyl dimethacrylate (PCLDIMA)

    (1) Add 7.077 g OCL (Mw: 2000 g/mol) + 1 mL 2-isocyanatoethyl methacrylate + 30 ppm dibutyltin dilaurate in 50 mL dichloromethane (calculate weight of 2-isocyanatoethyl methacrylate based on 2:1 molar ratio between OCL and 2-isocyanatoethyl methacrylate)

    (2) Use a balloon to keep N_2 environment inside of the flask

    (3) React for 5 days at room temperature

    (4) After 5 days of reaction, precipitated in a mixture of hexane/methanol/diethyl ether mixture (18:1:1) at 30°C, filtered and subsequently dried overnight in a vacuum chamber.

3. Reversible shape memory polymer (rSMP)

    (1) Add 2:1 wt. ratio of 2,000 g/mol PCLDIMA and 15,000 g/mol PCLDIMA

    (2) Heat it at 90°C oven for 30 min

    (3) Add 25 wt.% of 35.6 mg/mL benzoyl peroxide dissolved butyl acrylate

    (3) Quickly mix before it polymerizes and transfers into the mold

    (4) Curing it at 90°C for an hour

CURRICULUM VITAE

Sang Won LEE

Dept. of Biomedical and Chemical Engineering

Syracuse University

Tel: +1-315-401-6417

E-mail: slee155@syr.edu

EDUCATION & TRAINING	

Aug. 2015 ~ present	**Ph. D.**: Chemical Engineering
	Syracuse University, NY, USA
	Advisor: Prof. Dacheng Ren
	Thesis: Effects of Surface Topography on Biofilm Formation
Mar. 2012 ~ Feb. 2014	**M. S.**: Chemical and Biological Engineering
	Seoul National University, Seoul, South Korea
	Advisor: Prof. Jae Jeong KIM
	Thesis: Study on the effects of corrosion inhibitor according to the functional groups for Cu chemical mechanical polishing in neutral environment
Mar. 2006 ~ Feb. 2012	**B. S.**: Chemical Engineering
	SungKyunKwan University, Suwon, South Korea
	Thesis: Polymer-clay nanocomposite
Feb. 2012	Completion of the 2012 training program on Semiconductor Processes at Inter-university Semiconductor Research Center in SNU

Research Experience	

Sep. 2019 ~ present	NSF scholar (guest researcher) at FDA, Silver Spring, MD, USA
	Working on the infections in biomedical devices
Aug. 2015 ~ present	Research assistant at Biofilm Laboratory
	Syracuse University, Syracuse, NY, USA
	- Characterized and assessed the effect of dynamic surface topography on biofilm removal for biomedical devices (e.g. catheters)

	- Demonstrated the sensitization of biofilm cells by dynamic surface topography through antibiotic susceptibility test and genomic analysis (e.g. RNA-seq)
July 2019 ~ Aug. 2019	ORISE Fellow at FDA, Silver Spring, MD, USA Working on the infections in biomedical devices
Apr. 2019 ~ June. 2019	NSF scholar in residence at FDA, Silver Spring, MD, USA Working on the infections in biomedical devices
June. 2018 ~ Aug. 2018	Undergraduate research mentor in ECS Leadership Scholar REU program Syracuse University, Syracuse, NY, USA (Mentee; Katherine Gardner, Adviser; Prof. Dacheng Ren) - Assessed the effect of nano-scale pillar topography on biofilm removal (**Awarded 2nd prize in poster presentation**)
June. 2017 ~ Aug. 2017	Undergraduate research mentor in 2017 Interactive Biomaterials REU Program Syracuse University, Syracuse, NY, USA (Mentee; Alexander Deen Fusi, Adviser; Prof. Dacheng Ren) - Assessed the effect of nano-scale pillar topography on biofilm removal and anti-microorganism
Mar. 2012 ~ Feb. 2014	Research assistant at Electronics Processing Research Laboratory Seoul National University, Seoul, South Korea - Characterized the composition of cleaning solution for Cu CMP process - Verified and assessed the cleaning solution for invar cleaning process - Developed the CMP solution for Cu and Al CMP process

Teaching Experience

Fall 2018	Lab instructor in BEN301 Biological Principles for Engineers Syracuse University, Syracuse, NY, USA (Adviser; Prof. Dacheng Ren) - Leaded 8 lab courses (two times each for 4 different lab classes). Graded lab reports and exams. Communicated between students and professors. 37 junior students
Spring 2018	Teaching assistant in BEN212 Experimental Methods in Chemical Engineering Syracuse University, Syracuse, NY, USA (Adviser; Prof. Ian Hosein) - Held weekly office hour, graded homework and exams. Attended classes with students and helped solving problems and activities. 65 sophomore students

Spring 2018	Teaching assistant in CEN551 Biochemical Engineering
	Syracuse University, Syracuse, NY, USA
	(Adviser; Prof. Dacheng Ren)
	- Graded homework and exams. Conducted one lecture class. Communicated between students and professors. 25 graduate students

Fall 2017	Lab instructor in BEN301 Biological Principles for Engineers
	Syracuse University, Syracuse, NY, USA
	(Adviser; Prof. Dacheng Ren)
	- Leaded 8 lab courses (two times each for 4 different lab classes). Graded lab reports and exams. Communicated between students and professors. 33 junior students

Spring 2013	Teaching assistant in Physical Chemistry II
	Seoul National University, Seoul, South Korea
	(Adviser; Prof. Jae Jeong Kim)
	- Held weekly office hour, graded homework and exams. Attended classes with students and helped solving problems and activities. 52 sophomore students

Fall 2012	Teaching assistant in Physical Chemistry I
	Seoul National University, Seoul, South Korea
	(Adviser: Prof. Jae Jeong Kim)
	- Held weekly office hour, graded homework and exams. Attended classes with students and helped solving problems and activities. 50 sophomore students

Work Experience

Sep. 2019 ~ present	NSF scholar (guest researcher) at FDA, Silver Spring, MD, USA
	Working on the infections in biomedical devices
July 2019 ~ Aug. 2019	ORISE Fellow at FDA, Silver Spring, MD, USA
	Working on the infections in biomedical devices
Apr. 2019 ~ June. 2019	NSF scholar in residence at FDA, Silver Spring, MD, USA
	Working on the infections in biomedical devices
Jan. 2015 ~ Aug. 2015	Researcher at "Research Center for Energy Conversion and Storage"
	(Engineering Research Center designated by the Ministry of Science, ICT and

	Future Planning and the National Research Foundation of Korea), Seoul, South Korea
	- Investigate the effect of TAD-based cleaning solution on chemical mechanical planarization and cleaning solution of MEMS process
Mar. 2014 ~ Dec. 2014	Researcher at "Institute of Chemical Process (ICP)"
	(Engineering Research Center designated by the Ministry of Science, ICT and Future Planning and the National Research Foundation of Korea), Seoul, South Korea
	- Investigate the effect of TAD-based cleaning solution on chemical mechanical planarization and cleaning solution of MEMS process
Jul. 2011 ~ Aug. 2011	International research internship at BISCO Corp. Lab., Chicago, IL, USA
	- Verified the product 'ALL-BOND' with changing the composition of chemicals.
	- ALL-BOND: An adhesive product on dentistry field

Training Experience

Jan. 2016	Completion of the 2016 training program at Cornell NanoScale Science & Technology Facility (CNF) in Cornell University
	- Finished trainings for MEMS process such as photolithography, deposition, oxidation, and etching process
Feb. 2012	Completion of the 2012 training program on Semiconductor Processes at Inter-university Semiconductor Research Center in SNU
	- Finished trainings for MEMS process such as photolithography, deposition, oxidation, and etching process

PUBLICATIONS

1. Huan Gu, **Sang Won Lee,** Joseph Carnicelli, Zheng Tang, and Dacheng Ren, "Long-term biofilm control by tunable active topographies.", *Nat. Commun.* **11**, 2211 (2020).

2. Huan Gu, **Sang Won Lee,** Joseph Carnicelli, Zhaowei Jiang, and Dacheng Ren, "Antibiotic susceptibility of Escherichia coli cells during early-stage biofilm formation.", *J. Bacteriol.,* **201**, 18 (2019).

3. **Sang Won Lee,** Huan Gu, James Bryan Kilberg, and Dacheng Ren, "Sensitizing bacterial cells to antibiotics by shape recovery triggered biofilm dispersion", *Acta Biomater.*, **81**, 93 (2018).

4. Huan Gu, **Sang Won Lee**, Shelby Lois Buffington, James H. Henderson, and Dacheng Ren, "On-demand removal of bacterial biofilms via shape memory activation", *ACS Appl. Mater. Interfaces*, **8**,

21140 (2016).

5. **<u>Sang Won Lee</u>**, Seung Uk Kim, Ki Ho Bae, Kang Uk Lee, Oh Joong Kwon, and Jae Jeong Kim, "The effect of TAD based cleaning solution on post Cu CMP process", *Microelectronic Engineering*, **162**, 17 (2016).

6. **<u>Sang Won Lee</u>** and Jae Jeong Kim, "Study on the effects of corrosion inhibitor according to the functional groups for Cu chemical mechanical polishing in neutral environment", *Korean Chem. Eng. Res.*, **53**, 517 (2015).

PATENT

Jae Jeong Kim, **<u>Sang Won Lee</u>**, and Jin Uk Byun, "Cleaning composite of semiconductor wafer and display panel and manufacturing method thereof", Korean patent, registration number: 10-1799282, Nov. 14, 2017, application number: 10-2015-0155092, Nov. 5, 2015

Jae Jeong Kim, Seung Uk Kim, and **<u>Sang Won Lee</u>**, "Post-CMP washing liquid composition for substrate with copper wire", Korean patent, application number: 10-2012-0154515, Dec. 27, 2012 (withdrawn)

PRESENTATION

* Presenter

1. **<u>Sang Won Lee*</u>**, Ivan Gitsov Ivanov, and Dacheng Ren, "Biofilm control using caprolactone-based reversible shape memory polymer", *2020 Stevenson Biomaterials Lecture Series,* Syracuse, NY; March 6, 2020.

2. Huan Gu*, **<u>Sang Won Lee</u>**, Joseph Carnicelli, Teng Zhang, and Dacheng Ren, "Long-term biofilm control by tunable active topographies", *2020 Stevenson Biomaterials Lecture Series,* Syracuse, NY; March 6, 2020.

3. **<u>Sang Won Lee*</u>**, Michael Wong, Anant Agrawal, Allan Guan, Shervin Abdollahi, Yi Wang, Ralph J Basile, Kaumudi Kulkarni, Miranda Gavette, Jahan Azizi, Jerri Tripp, Elena Campbell, Marc Bloom, Norton Elson, Mohamed Labib, Dacheng Ren, and K. Scott Phillips, "Quality control of endoscope reprocessing: three hospital clinical study using rapid, point-of-reprocessing methods to detect protein and biofilm", *2020 Biofilm Science and Technology Meetings*, Arlington, VA; February 5, 2020.

4. **<u>Sang Won Lee*</u>**, Ivan Gitsov Ivanov, and Dacheng Ren, "Biofilm removal using reversible shape memory polymer", *2019 AIChE Annual Meeting, Orlando*, FL; November 11, 2019. (**Awarded a prize in the poster competition**)

5. Huan Gu*, **<u>Sang Won Lee,</u>** and Dacheng Ren, "Preventing bacterial biofilm formation using active surface topography", *2019 AIChE Annual Meeting, Orlando*, FL; November 12, 2019.

6. **<u>Sang Won Lee*</u>**, Hainsworth Shin, Irada Isayeva, Dacheng Ren, and K. Scott Phillips, "The effects of topography on bacterial attachments for breast implant devices", *FDA Annual Summer Student Poster Day Presentations 2019*, Silver Spring, MD; August 7, 2019.

7. Le Hoang Phu Pham*, Hao Wang, **<u>Sang Won Lee</u>**, Yi Wang, Xiaolong Luo, and K. Scott Phillips, "A high-throughput platform to study the relationship between biofilm persistence and antimicrobial resistance", *FDA Annual Summer Student Poster Day Presentations 2019*, Silver Spring, MD; August 7, 2019.

8. Michael Wong, Anant Agrawal, Allan Guan, Shervin Abdollahi, **<u>Sang Won Lee*</u>**, Dacheng Ren, and K. Scott Phillips, "Residual protein and bacteria on endoscopes before and after reprocessing", *FDA Annual Summer Student Poster Day Presentations 2019*, Silver Spring, MD; August 7, 2019.

9. Huan Gu*, **<u>Sang Won Lee,</u>** Joseph Carnicelli, Zhaowei Jiang, and Dacheng Ren, "Not always resistant: antibiotic susceptibility of bacterial cells during early-stage biofilm formation", *The 5th Stevens Conference on Bacteria-Material Interactions*, Hoboken, NJ; June 12, 2019.

10. **<u>Sang Won Lee*</u>**, Huan Gu, James Bryan Kilberg, and Dacheng Ren, "Physiological changes in bacterial cells induced by shape recovery triggered biofilm dispersion", *The 5th Stevens Conference on Bacteria-Material Interactions*, Hoboken, NJ; June 12, 2019.

11. **<u>Sang Won Lee*</u>**, Huan Gu, James Bryan Kilberg, and Dacheng Ren, "Physiological changes in *Pseudomonas aeruginosa* cells induced by shape recovery triggered biofilm dispersion", *The ECS Research Day*, Syracuse, NY; March 29, 2019.

12. **<u>Sang Won Lee*</u>**, Huan Gu, James Bryan Kilberg, and Dacheng Ren, "Physiological changes in bacterial cells induced by shape recovery triggered biofilm dispersion", *2019 Stevenson Biomaterials Lecture Series*, Syracuse, NY; March 1, 2019.

13. **<u>Sang Won Lee*</u>**, Huan Gu, James Bryan Kilberg, and Dacheng Ren, "Sensitizing Bacterial Cells to Antibiotics through Dynamic Topography–Triggered Biofilm Detachment", *2018 AIChE Annual Meeting,* Pittsburgh, PA; October 29, 2018.

14. Huan Gu*, **<u>Sang Won Lee</u>**, and Dacheng Ren, "A New Antifouling Strategy with Active Surface Topography", *2018 AIChE Annual Meeting,* Pittsburgh, PA; October 29, 2018.

15. **<u>Sang Won Lee*</u>**, Huan Gu, James Bryan Kilberg, and Dacheng Ren, "Sensitizing Pseudomonas aeruginosa to antibiotics by shape recovery triggered biofilm dispersion", *2018 ASM Biofilm Conference,* Washington D.C.; October 11, 2018.

16. Katherine Gardner*, **<u>Sang Won Lee</u>**, and Dacheng Ren, "Biofilm removal using shape memory polymers", *2018 ECS Leadership Scholar REU program,* Syracuse, NY; August 10, 2018. (**Awarded 2nd prize in poster presentation**)

17. Bryant J. Chung*, Huan Gu, **<u>Sang Won Lee</u>**, and Dacheng Ren, "A New System to Control Biofouling Using an Active Topography", *2018 ECS Leadership Scholar REU program,* Syracuse, NY; August 10,

2018.

18. Huan Gu, **Sang Won Lee**, and Dacheng Ren*, "A New Strategy for Biofilm Control Using Bioinspired Dynamic Surface Topography", *Biofilms 8 conference,* Aarhus, Denmark; May 29, 2018.

19. **Sang Won Lee***, Huan Gu, and Dacheng Ren, "Sensitizing bacterial cells to antibiotics through dynamic topography-triggered biofilm detachment", *2018 Stevenson Biomaterials Lecture Series*, Syracuse, NY; April 23, 2018.

20. **Sang Won Lee***, Huan Gu, and Dacheng Ren, "Sensitizing bacterial cells to antibiotics through dynamic topography-triggered biofilm detachment", *The ECS Research Day*, Syracuse, NY; March 30, 2018.

21. Alexander Deen Fusi*, **Sang Won Lee**, Huan Gu, and Dacheng Ren, "Effects of dynamic nano-scale surface topography on *Escherichia coli* biofilm formation", *2017 Interactive Biomaterials REU Program,* Syracuse, NY; August 10, 2017.

22. **Sang Won Lee***, Huan Gu, and Dacheng Ren, "Sensitizing bacterial cells to antibiotics through dynamic topography-triggered biofilm detachment", *The 4th Stevens Conference on Bacteria-Material Interactions*, Hoboken, NJ; June 15, 2017.

23. **Sang Won Lee***, Huan Gu, and Dacheng Ren, "Sensitizing bacterial cells to antibiotics through dynamic topography-triggered biofilm detachment", *The ECS Research Day*, Syracuse, NY; April 25, 2017.

24. Huan Gu*, **Sang Won Lee**, Shelby Lois Buffington, James H. Henderson, and Dacheng Ren, "On-demand release of bacterial biofilms via shape memory activation", *2016 AIChE Annual Meeting, Biomaterials: Faculty Candidates II*, San Francisco, CA; November 14, 2016.

25. **Sang Won Lee***, Myung Jun Kim, Kiho Bae, and Jae Jeong Kim, "Effects of functional groups in corrosion inhibitors on the performance of chemical mechanical polishing", *2013 Spring Annual Meeting of Korean Institute of Chemical Engineers*, Kwangju, Korea; April 25, 2013.

PROJECT PARTICIPATION

1. "Rational Design of Dynamic Antifouling Material Topographies for Safer Medical Devices"
   Funded by National Science Foundation (NSF), Aug. 2018 ~ July 2020 (**$100k**)

2. "Integrating synthetic biology approaches with patterned biofilm formation to investigate bacterial persistence in heterogeneous structures"
   Funded by National Science Foundation (NSF), July 2017 ~ June 2020 (**$300k**)

3. "IGERT: Soft Interfaces - Bridging the Divide in Graduate education (iBriD)"
   Funded by National Science Foundation (NSF), Sep. 2011 ~ Aug. 2018 (**$3.0M**)

4. "CAREER: Patterned Biofilm Formation by Surface Design: Linking Structure to Physiology and Genetics"
   Funded by National Science Foundation (NSF), May 2011 ~ Apr. 2017 (**$400k**)

5. "EFRI-MIKS: Deciphering and Controlling the Signaling Processes in Bacterial Multicellular Systems and Bacteria-Host Interactions"

   Funded by National Science Foundation (NSF), Oct. 2011 ~ Sep. 2016 (**$2.0M**)

6. "Development of the slurry for metal CMP based on ceria and cleaning solution"

   Funded by KCTech Co., LTD, Oct. 2010 ~ Sep. 2012 (**$100k**)

7. "Development of key cleaning technology for 10 nm-semiconductor and 8th generation display using damage free technology"

   Funded by Ministry of Trade, Industry and Energy, Korea, Sep. 2012 ~ Aug. 2015 (**$1.0M**)

AWARDS AND HONORS

Apr. 2020	2020 Graduate Student Award for Distinguished Biomaterials Research
Nov. 2019	Poster presentation competition award from *2019 AIChE Annual Meeting* ($369)
June 2019	Travel grant award from *The 5th Stevens Conference on Bacteria-Material Interactions* ($425)
Sep. 2015 ~ Aug. 2019	Graduate student fellowship from Syracuse University
Oct 2018	Travel grant award from Graduate School of Syracuse University ($150)
June 2017	Travel grant award from Graduate School of Syracuse University ($300)
Mar. 2013 ~ Aug. 2013	Merit-based scholarship from Seoul National University
Sep. 2010 ~ Feb. 2012	Superior Academic Performance external scholarship from Chugang Scholarship Association
Mar. 2008 ~ Feb. 2010	Military service as a Military Intelligence (MI) soldier for 2 years and a squad leader for 5 months. Took second place in the 'squad leader training education'
Sep. 2007 ~ Feb. 2008	Superior Academic Performance scholarship from SungKyunKwan University
Sep. 2006 ~ Feb. 2007	Superior Academic Performance scholarship from SungKyunKwan University